TERAHERTZ METAMATERIALS AND PLASMONICS USING TWO-DIMENSIONAL MATERIALS AND HIGHLY CONDUCTIVE TRANSPARENT OXIDES

by

Sara Arezoomandan

A dissertation submitted to the faculty of
The University of Utah
in partial fulfillment of the requirements for the degree of

Doctor of Philosophy

Department of Electrical and Computer Engineering

The University of Utah

May 2018

Copyright © Sara Arezoomandan 2018

All Rights Reserved

The University of Utah Graduate School

STATEMENT OF DISSERTATION APPROVAL

The dissertation of **Sara Arezoomandan**

has been approved by the following supervisory committee members:

Berardi Sensale Rodriguez	, Chair	**11/29/2017** Date Approved
Ajay Nahata	, Member	**12/13/2017** Date Approved
David Schurig	, Member	**11/29/2017** Date Approved
Steven Blair	, Member	**11/29/2017** Date Approved
Ashutosh Tiwari	, Member	**11/29/2017** Date Approved

and by **Florian Solzbacher** , Chair/Dean of

the Department/College/School of **Electrical and Computer Engineering**

and by David B. Kieda, Dean of The Graduate School.

ABSTRACT

Driven by a myriad of potential applications such as communications, medical imaging, security, spectroscopy, and so on, terahertz (THz) technology has emerged as a rapidly growing technological field during the last three decades. However, since conventional materials typically used in microwave and optical frequencies are lossy or do not effectively respond at these frequencies, it is essential to find or develop novel materials that are suitable for device applications in the THz range. Therefore, there is wide interest in the community in employing novel naturally-occurring materials, such as 2D materials, as well as in designing artificial metamaterial structures for THz applications. Here, we combined both of these approaches so to develop reconfigurable THz devices capable of providing amplitude modulation, phase modulation, and resonance frequency tuning.

First, graphene is employed as the reconfigurable element in metamaterial phase modulators. For this purpose, we propose the use of unit cells with deep-subwavelength dimensions, which can have multiple advantaged for beam shaping applications. The analyzed metamaterials have one of the smallest unit cell to wavelength ratios reported or proposed todate at THz frequencies. By systematic analysis of the geometrical tradeoffs in these devices it is found that there is an optimal unit cell dimension, corresponding roughly to ~$\lambda/20$, which can deliver the best performance. In addition to this, we explored other applications of graphene in metamaterial devices, including amplitude modulation and resonance-shifting. These studies motivated us to analyze what is the most suitable role of graphene from a THz device perspective: is graphene a good plasmonic material? Or it is better suited as a reconfigurable material providing tunability to otherwise passive metallic structures? Our studies show that the Drude scattering time in graphene

is an important parameter in this regard. In order to attain strong plasmonic resonances graphene samples with $\tau >> 1$ps are required, which is challenging in large area CVD samples. But graphene is just one example of a wider class of 2D materials. In this work we also studied for the first time the application of 2D materials beyond graphene as reconfigurable elements in THz devices. For this purpose, Molybdenum Disulfide (MoS_2) was employed as the reconfigurable element in cross-slot metamaterial amplitude modulators. Our results evidence that smaller insertion loss is possible when employing 2D materials with a bandgap, such as MoS_2, rather than a zero-gap material such as graphene. Furthermore, because of a stronger optical absorption active control of the metamaterial properties is possible by altering the intensity of an optical pump.

We later investigate and discuss transparent conductive oxides (TCOs), which constitute an interesting choice for developing visible-transparent THz-functional metamaterial devices for THz applications. These materials show a metallic THz response and thus can substitute the metal patterns in metamaterial devices. In our particular studies we analyzed samples consisting of: (i) two-dimensional electron gases at the interface between polar/nonpolar complex oxides having record-high electron density, and (ii) thin-films of La-doped $BaSnO_3$ having record-high conductivity in a TCO. These materials exhibit a flat THz conductivity across a broad terahertz frequency window. As a result of their metal-like broadband THz response, we demonstrate a visible-transparent THz-functional electromagnetic structure consisting of a wire-grid polarizer.

TABLE OF CONTENTS

ACKNOWLEDGMENTS

This journey would not have been possible without the support of my family, professors, and friends. To my family, thank you for encouraging me in all of my pursuits and inspiring me to follow my dreams, although staying away from you was the hardest part of this journey. I am especially grateful to my beloved husband, who supported me to do what I love to and was my companion in this journey. To my mom and dad, I always knew that you believed in me and wanted the best for me. To my sisters and brother that I missed in all these years.

I would like to express the deepest appreciation to my advisor and my committee chair Professor Berardi Sensale-Rodriguez; he continually and convincingly inspires me in regard to research and critical thinking. Without his guidance and persistent help this dissertation would not have been possible. He also was a great and supportive friend to me and helped me in all these years.

I would like to thank my committee members David Schurig, Ajay Nahata, Steve Blair and Ashutosh Tiwari, for their support and useful discussion. Also I would like to thank Bharat Jalan and his students who closely worked with us and provided samples and useful discussions. Also I would like to thank my colleagues Kai Yang, Hugo Condori, Prashanth Golpan, and Ashish Chanana; without their spirit of teamwork this dissertation would not be possible.

I would also like to thank to MRSEC for their financial support granted through my graduate study at University of Utah.

CHAPTER 1

INTRODUCTION

1.1 The THz spectral range

The THz spectral range, also referred to as submillimeter and far-infrared range, consists of electromagnetic waves with frequencies ranging from 300 GHz to 3 THz. Wavelengths in this spectral range correspondingly span from 1000 μm to 100 μm with respective photon energies ranging from 1.24 meV to 12.4 meV. THz electromagnetic waves are emitted as a part of black-body radiation from any objects with a temperature larger than 10K [1]. Historically, the THz frequency range has been referred to as the "THz gap" [2], owing to the fact that for a long-time exploration of this spectral region was scarce, and the interaction of THz electromagnetic waves with different materials was a mystery. Furthermore, during many decades there was an absence of efficient THz generation and detection techniques. The main motivations and driving forces for exploring this spectral range were astronomy and chemistry. But after the introduction of efficient room-temperature THz sources and detectors over the last three decades of the 20th century, new applications have emerged, such as spectroscopy, medical imaging, security, communications, etc., in which THz wavelengths can offer some remarkable advantages. In addition to its practical applications, the THz spectral range also appears as an interesting subject in fundamental science to study light-matter interaction. After

developing functional sources and detectors for THz spectroscopy, physicists and materials scientist have also used THz spectroscopy as a noncontact, noninvasive method to reveal many important low-energy physical properties of condensed matter.

As mentioned, astronomy was one of the first motivations for researchers to develop THz systems. Interstellar dust sizes are in the range of 100 μm to 1 mm, thus associated with THz wavelengths [1]. In addition, the black-body radiation from interstellar particles with temperatures between 10-20K (with the cosmic background noise of 2.7K) occurs in the THz frequency range. Therefore, THz detection will improve our understanding of the cosmos. Studies of the spectral energy distribution in galaxies show that half of the total luminosity and 98% of the emitted photons since the big bang are located in the THz spectral range [3]. Consequently, for achieving a comprehensive understanding of any cosmological phenomena, we are in need of proper THz detection mechanisms. Furthermore, many abundant molecules, like oxygen, water, carbon monoxide and nitrogen, have absorption lines in the THz spectral region [1]. Probing these molecules in regions of the universe where star formation occurs is essential for observation of the star formation phenomena in early stages. In addition, with regard to our planet, THz probing can be used to observe thermal absorption of the tropospheric layer and study ozone destruction, global warming, and other atmospheric phenomena [4].

Spectroscopy has been another primary application field motivating the development of THz technology; this is a result of the strong emission and absorption features associated with vibrational, rotational, torsional, phonon, intermolecular and intramolecular modes present in this spectral range [5]. For example, DNA molecules show phonon absorption in this frequency range, which motivates THz studies on detection

of DNA molecule signatures [6], [7]. It is worth mentioning that far-IR spectroscopy is a technique that has been well established for a long time. However, THz spectroscopy is different from far-IR spectroscopy in which black-body radiation and photon detection are used as methods of generation and detection. In this aspect, it is important to note that the signal to noise ratio in conventional far-IR spectroscopy will decrease at longer wavelengths. In THz spectroscopy, bright sources and different detection techniques are used which improves the signal to noise ratio when compared to far-IR spectroscopy in longer wavelengths. Time domain spectroscopy (TDS) is a technique that is widely used for spectroscopy in the THz region of the spectrum. Recent developments in this technique have led to commercially available systems. In addition, availably of compact and portable TDS systems have popularized the use of this technique for chemical analysis. Due to the low photon energy and nonionizing nature of this probing method, it is a safe, noninvasive, nondestructive technique to characterize chemical compounds, which makes it THz spectroscopy attractive in the drug and food industry, as well as for security applications [8].

THz radiation can penetrate through normal clothing and usual packaging with tolerable attenuation, so it is a feasible choice for security purposes. In this regard, currently, the majority of security systems in airports are based on millimeter wave technologies. By integrating THz spectroscopy and imaging techniques, this higher frequency range can be utilized for more complex and functionally integrated security purposes. In addition, THz spectroscopy can be used to identify explosive materials as well as illegal drugs [9], [10].

Aforementioned, THz radiation is noninvasive and nonionizing, which makes it a

potential candidate for medical imaging. Due to the small penetration depth of THz beams in tissues and owing to its sensitivity to the water content of tissue, only visible-accessible parts of the body are potential targets for THz imaging. In this regard, the ultimate goal of THz biomedical imaging is to replace invasive methods like biopsy with noninvasive techniques at least in some areas such as skin cancer detection [11], [12]. Dermatology is the first application that widely uses THz imaging since the skin is the most accessible organ for reflection measurements. THz imaging was demonstrated in wound healing monitoring measurements. Using THz imaging, scar tissue and healthy tissue can be differentiated, and since THz can probe without removing the wound dressing it has advantages over other alternative methods [13]. Also, THz can differentiate between benign and malignant lesions and measure the depth of the lesion in the skin. So THz imaging is a suitable technique for diagnosing of malignant cancers at its early stages [14], [15]. Another application of THz imaging in dermatology is to measure the water content and skin hydration, which can be employed so to monitor and reveal the impact of cosmetic products [16]. Teeth are the next accessible choice in our body for THz imaging. In dentistry, imaging options are fewer than those in dermatology, and radiography is widely used for diagnoses. But it is shown that THz imaging due to its nonionizing nature can detect caries in primary stages, which is not possible with X-ray imaging [17], [18]. If caries can be detected in its primary stages, by early therapy it can be reversed and filling procedures could be prevented. It is worth mentioning that by using this technique, primary caries can be differentiated from low mineralization regions. In addition to these applications in dermatology and dentistry, there are also some initial works showing THz imaging of human breast cancer tissue [19]–[21]. As the interest in THz imaging

techniques increases, more and more potential applications will emerge.

Wireless communications is perhaps one of the most important potential applications for THz technology. As based on Edholm's law, the bandwidth demand in communication networks triples every 18 months [22]; the prediction for 2020 is 100 Gbps. There are two approaches for addressing this growth in demand: the first approach is to use advanced modulation techniques or MIMO systems, and the second approach is to utilize higher frequency carriers. Since there is a fundamental upper limit for the achievable bandwidth using signal processing techniques [23], eventually, using higher frequency carriers will become inevitable. Right now, microwave (i.e., GHz) carriers are used for wireless communication links, but ultimately, the demand for bandwidth will force us to use millimeter-waves and THz frequencies for communications.

In order to enable the use of THz for communication systems, we need to develop different system components such as sources, detectors, modulators, switches, filters, amplifiers, etc. Most conventional materials and design approaches typically used in optics or at microwave frequencies are not applicable in the THz frequency range. Since most materials are lossy at these frequencies it is essential to find or develop new materials suitable for the THz range [24]. Therefore, researchers have been interested in finding novel naturally occurring materials, such as graphene, liquid metals, etc. as well as in designing artificial metamaterial structures for application in the THz range.

1.2 Visible-transparent conductive materials and devices

Transparent electronics have always been a part of the image that describes the future as usually seen in science-fiction movies. In 1997, for the first time, a transparent

circuit was demonstrated based on transparent conductive oxides (TCOs), which was called the “invisible circuit” [25], [26]. Subsequently, transparent electronics does not sound so unreachable. Since then there has been an enormous effort for realizing such devices and for discovering new materials enabling transparent electronic applications. TCOs are materials which are electrically conductive and visually transparent; during World War II, these materials were used as heaters in aircraft windshields to prevent icing [27]. These materials have vast applications as passive electrical and optical elements, for example, in solar cells, antistatic coating, and flat panel display. Since the introduction of the first circuits based on TCOs [28]–[30], several electronic devices were proposed and fabricated based on this family of materials.

The first transparent thin-film transistor (TTFT) was introduced and demonstrated in 2003 [28]–[30]. Although the quality of these transistors is not yet comparable with that of silicon MOSFETs, there is an intense effort to improve the quality of these devices by introducing new materials and device designs. The market for transparent electronics is growing fast and is expected to be worth more than 2 billion dollars in 2023 [31]. Usually, it takes one or two decades before a device technology can be commercialized, so we expect to have commercial transparent devices around 2020.

One of the many challenges that this technology is facing is the small operational frequency of these devices, which is a bound by kHz to few MHz with existing devices [32]. This drawback is caused by the small mobility available in these transparent thin films and can restrict certain applications such as telecommunications. The materials science community is constantly in search of new materials which can improve the mobility and therefore the operational frequency of transparent devices.

Conductive transparent materials are an essential group of materials for the demonstration of transparent devices as well as several other applications like liquid-crystal displays (LCDs), solar cells, and LEDs. These materials can be classified in two large groups: the first group is TCOs which possess high band-gap and either n-type or p-type conduction. Typical examples of these materials are Sn-doped indium oxide (ITO), doped zinc oxide (ZnO) and Cadmium oxide (CdO) [33]–[35]. Also, conductive polymers have been introduced, for example poly(3,4-ethylenedioxythiophene) doped with polystyrene sulfonic acid (PEDOT:PSS) [36], [37] which offers these properties. The major problem with this group of materials is their limited conductivity; the largest achieved conductivity value among these group of materials was found in ITO [38], with conductivity values $\sim 10^4\ S/cm$ at room temperature. This material is widely used in transparent electrodes for many applications. However, the conductivity found in ITO is still two orders of magnitude smaller than metal conductivities and the search for new transparent materials with higher conductivity never stops. The second group of materials is not necessarily transparent, but their dimensions are engineered so that they are conductive in one direction and effectively transparent in another; nanowires [39], [40] and 2D materials [41], [42] belong to this group of materials. These materials are conductive in-plane and relatively transparent out-of-plane as a result of their very small thickness. Graphene is one of the most prominent 2D materials, and is widely used as a transparent electrode since its inception.

In this dissertation, I will study materials from each of these two groups— TCOs and 2D materials— and use them to realize electromagnetic structures and reconfigurable devices for applications in the THz frequency range. As mentioned before, most of the

conventional materials that are used in millimeter wave or infrared frequencies are lossy in the THz range and do not respond to these frequencies in a controllable manner. For achieving efficient devices, we are constantly in search of new materials. Two methods are commonly used for realizing functional electromagnetic structures in the THz frequency range, namely, (a) taking advantage of the intrinsic properties of materials, e.g., plasmonic properties, or (b) by engineering "artificial" structures by merging several materials at subwavelength scales, e.g., metamaterial approaches. Here, we are going to use both of these approaches to demonstrate functional devices in the THz frequency range. In this regard, graphene, apart from being used as a transparent electrode in electronic applications, is currently one of the materials of greatest interest to develop THz devices. Furthermore, TCOs can be also beneficial for THz technology, since they can enable devices that are functional at THz frequencies and transparent in the near-IR and visible ranges. In the next two sections of this introductory chapter I will describe graphene and some of its THz applications as well as introduce my work on graphene and TCOs.

1.3 Graphene

Graphene is a two-dimensional (2D) material with a hexagonal lattice which is formed from carbon atoms. Single-layer graphene was synthesized experimentally for the first time in 2004 [43]. However, its existence was predicted by physicists a long time ago [44]. In early efforts, mechanical exfoliation (using a scotch tape) was employed to peel off graphene from graphite crystals. However, the mechanical exfoliation method is a random process and only provides small flakes of graphene in the order of several 10 μm or smaller. Later, several other methods such as thermal annealing of SiC [45], [46],

chemical vapor deposition (CVD) [47], [48], and reducing graphene oxide [49] were developed so to synthesize large area graphene.

Thermal annealing of SiC single crystals at 1500˚C will result in evaporation of Si, which leaves the substrate, and thus the remaining carbon atoms will form graphene [50]. This method is very easy to perform. However, the SiC crystals are expensive and due to formation of a buffer layer between graphene and the substrate the transfer process is very difficult. But graphene devices can be potentially fabricated directly on the SiC substrate. Reduction of graphene oxide is a popular method for bulk application, like manufacturing composites, conductive inks, or conductive pastes. The complete reduction of the oxide to graphene is very difficult and this will lead to samples suffering from defects. CVD graphene synthesis uses hydrocarbon molecules in the presence of a metal catalyst at a high temperature of 900-1080˚C. The number of layers in this growth procedure depends on the metal catalyst. In the presence of Ni and Pd the final structure will be multilayer and its thickness depends on gas flow and other growth parameters [51], [52]. However, by using Cu as metal catalyst one can achieve single layer graphene since the synthesis is a self-limiting process [53]. The graphene synthesized using CVD process is easy to transfer to any arbitrary substrate which makes it an interesting choice for flexible electronics and many other applications. Achieving a large area is also another advantage of this method and is relatively cheap. Dark-field transmission electron microscopy (DF-TEM) on CVD grown sample indicates that this growth process leads to polycrystalline samples with grain sizes in the order of 500 nm to several micrometers, and these grains are randomly rotated [54].

In addition, several transfer techniques were developed to transfer the synthesized

graphene films into arbitrary substrates. Wet transfer using a supporting layer, usually PMMA, is the most common method by which the graphene layer is spin coated with a PMMA supporting layer and then the film is released in a metal etchant solution after what is finally transferred to the desired substrate. There are also several alternative dry transfer methods such as roll-to-roll transfer in which very large samples (~30 inch) can be transferred [48], [55]. Also there are other transfer techniques proposed in the literature such as electrochemical and imprinting techniques [56]–[58].

Graphene proves to be an interesting material for developing reconfigurable and active devices due to its extraordinary electro-optic properties. Graphene is a material without a bandgap, which means that the valence band and conduction band meet in one point, called the Dirac point. As in semiconductors, the optical conductivity in graphene is determined by the superposition of two different optical absorption mechanisms, namely intraband and interband transitions, which can be expressed as [59]:

$$\sigma(\omega) = \sigma_{\text{intra}}(\omega) + \sigma_{\text{inter}}(\omega) \tag{1.1}$$

$$\sigma_{\text{intra}}(\omega) = \frac{ie^2 E_f}{\pi\hbar(\omega+\frac{i}{\tau})}. \tag{1.2}$$

$$\sigma_{\text{intra}}(\omega) = \frac{ie^2\omega}{\pi}\int_0^\infty \frac{f(\varepsilon-E_f)-f(-\varepsilon-E_f)}{(2\varepsilon)^2-(\hbar\omega+i\Gamma)^2}\,d\varepsilon \tag{1.3}$$

where e is the electron charge, E_f is the Fermi level, ħ is the reduced Planck constant, ω is the angular frequency, τ is the electron momentum relaxation time, f is the Fermi-Dirac distribution function, and Γ is the phenomenological scattering rate. In the low-frequency regime, i.e., the THz frequency range, the intraband transition mechanism is dominant, whereas in the high-frequency regime, i.e., the visible spectrum, the interband transition mechanism is dominant. In Fig. 1.1 the conductivity of graphene is shown versus

frequency for different Fermi levels. Figure 1.1 also shows that by changing the Fermi level, graphene's optical conductivity can be tuned. In the THz frequency range, the impact of the interband transitions is negligible, due to the low THz photon energy, which is on the order of a few meV, which makes intraband transitions the dominant absorption phenomenon. Therefore, graphene conductivity can be expressed using a Drude model at THz wavelengths, as:

$$\sigma_{THz} = \frac{1}{1+j\omega\tau} \tag{1.4}$$

in which σ_{DC} is the direct current (DC) electrical conductivity, and τ is electron momentum relaxation time. In conventional 2D semiconductors with parabolic band structure $\sigma_{DC} \propto E_f \propto \sqrt{n}$ but in graphene, due to its conical band structure $\sigma_{DC} \propto E_f \propto n$. Therefore, as in semiconductors the conductivity of graphene can be effectively tuned when $\omega < 1/\tau$. τ depends on graphene quality and ω typically is between 1-4THz.

In higher frequency regimes, interband transitions are the dominant term and at the limit of very high frequencies ($\omega \to \infty$), the optical conductivity of graphene will be $\frac{e^2}{4\hbar}$, which results in $\sim$2.3% absorption per layer of graphene. As indicated in Fig.1.1 the optical conductivity is a constant value and independent of Fermi level in this region. Therefore, graphene in single layer form has a negligible absorption in the visible frequency range and it is mainly transparent.

Graphene is also known for its large carrier mobility. As a result of the linear E-k dispersion in graphene, its charge carriers behave like massless Dirac fermions. In practice, these massless fermions lead to a very large mobility in graphene, e.g., mobility in the order of 10^6 cm^2/V.s has been reported in suspended graphene samples [60]. Overall graphene

can provide greater conductivity per unit length than any other known semiconductor. These properties prove graphene to be one of the most promising reconfigurable materials for THz frequencies.

As stated before, the conductivity of graphene can be tuned in the THz frequency range by means of changing the Fermi level. To control the Fermi level there are several proposed methods. One of the methods proposed is to gate graphene using a semiconductor substrate, e.g., silicon (e.g., [61]). Another way introduced in the literature is to self-gate graphene (e.g., [62]). In this method two layers of graphene are separated with a dielectric layer, and, by applying a voltage between these layers, accumulation of different type of charge carriers takes place in opposite layers. By means of injecting and depleting carriers in these layers the Fermi levels are therefore tweaked. Moreover, there are several other methods discussed in the literature such as gating graphene using ion-gels [63] or doping graphene chemically [48]. In the chemical doping method, the graphene layer is typically doped using nitric acid, which is a known dopant of other carbon products such as carbon nanotubes [64]. The attainable doping level depends on the acid concentration and the duration of soaking. Also, this doping can be either time-variant (i.e., reversible) or time-invariant (i.e., irreversible) depending on the experimental conditions.

As mentioned before graphene is one of popular active material in THz frequency. However, over large areas graphene in its single layer form can achieve limited performance, due to its practically achievable conductivity swing being limited as a result of fabrication issues [61], but by patterning graphene or by integrating it with metamaterial we can boost the performance of THz devices.

1.4 Metamaterials for THz applications

Metamaterials are artificially-made structures that are engineered to achieve desirable electromagnetic properties, and thus are capable of achieving properties beyond what is possible in naturally occurring materials [65]. Usually, metamaterials are made of unit cells arranged in lattices, and the lattice dimensions are small relative to the operational wavelength, which causes these structures to be recognized as a homogenized effective medium in the operational frequency range. The properties of metamaterials are affected by the properties of the component materials as well as by the geometrical features of the unit cells. Metamaterials are widely used to manipulate electromagnetic waves and other physical phenomena. Using this concept, various exotic unnatural phenomena like negative refractive index and ultrahigh refractive index have been demonstrated. Historically, the theory and first implementation of metamaterials took place at microwave frequencies, but later this was applied to higher frequency ranges such as the THz and the visible.

In the THz range, since most natural materials are not able to effectively interact with these electromagnetic waves, metamaterials provide a promising method to enhance the light matter interaction. Using metamaterials, unit cell designs can be engineered to achieve a set of desired properties. In addition, in the THz frequency range, fabrication of subwavelength structures can be achieved using standard lithographic techniques. As a result, the metamaterial approach has become very popular at this frequency range. There are many studies proposing different metamaterial structures for THz applications, such as modulators and filters [66], [67]. These designs can be divided into two major groups of passive and active metamaterials. Usually passive metamaterial designs are based on metallic films patterned in different geometries, arranged in an array (e.g., [68]). Active

control of THz signals is one of the biggest challenges in THz science and technology field. In order to address this challenge, a popular approach is to use an active metamaterial in which the effective THz permittivity of the metamaterial structure should be tuned. For demonstrating this active control, usually a metamaterial design is either made out of or integrated with an active medium like conventional semiconductors, two-dimensional electron gas (2DEG), phase transition materials, etc. In the past decade, several actuation approaches have been taken so to effectively control the THz permittivity of metamaterials, such as electrical, thermal, mechanical, optical, and plasmonic effects. Among all these methods, electrical tuning is the most attractive option due to its integrability. Typically, semiconductors are the suitable choice for electrically tuning permittivity, but, as mentioned, most of the conventional semiconductor materials lead to high insertion loss when used in the THz frequency range, and their responses are weak. Therefore, we are in search of new materials which can efficiently manipulate THz frequencies and meanwhile introduce low insertion loss. From this perspective, graphene, as a reconfigurable semimetal, proves to be good candidate for metamaterial applications at THz frequencies.

1.5 Graphene-based THz metamaterials

Based on the extraordinary electro-optical properties of graphene and the capability of tuning its optical conductivity in a wide range of frequencies, graphene attracted lots of attention from the THz research community. Several devices were designed and demonstrated based on graphene. The first of such devices based on graphene were realized actually in the infrared. However, in 2011, Ju et al. demonstrated the first reconfigurable plasmonic device based on graphene stripes which were gated using ion-gel [63]. Later in

2012, Yan et al. proposed a stack of graphene/insulator layers in disk shape array, where resonance tuning was achieved via chemical doping [69]. Early works on graphene in the THz frequency range were motivated by modulator applications. In 2012, the first graphene-based THz device, a large area modulator, was demonstrated by Sensale-Rodriguez et al. In this configuration gating was achieved by applying a voltage between a graphene layer and a semiconductor substrate [61]. More recently a new configuration of gating, self-gating, which was also proposed by Sensale-Rodriguez et al. in [61], was experimentally introduced by Gomez-Diaz et al., in which two layers of graphene are separated with a dielectric layer and by applying voltage between these layers the Fermi level can be tuned [70]. Later work by Lee et al. in 2012 introduced the first metamaterial integrated with a graphene film, which operates as a switch for THz waves [71]. Furthermore, graphene integrated with split ring resonators was experimentally demonstrated for THz modulation by Valmorra et al. [72] and Degl'Inocenti et al. [73].

Several studies also investigated the fundamental limits in the performance of devices based on graphene. In 2014, Tamagnone et al. showed by random simulation across the whole design space that there are fundamental limits between the insertion loss and modulation depth in designing graphene-based modulators [74]. Later work by Yan et al. indicates that the separation between the active graphene layer and the metallic metamaterial is a key parameter in controlling the tradeoff between insertion loss and the modulation depth in these devices, in other words, the strength of the light-matter interaction needs to be carefully tailored so as to obtain the best tradeoffs in device performance [75]. In addition, in a simulation study based on split ring resonators made only of graphene, Zouaghi et al. showed that the Drude scattering-time is an effective

parameter in defining the device performance [76].

Even though most of the first applications of graphene at THz frequencies were on developing amplitude modulators, several other devices were also proposed based on graphene integrated metamaterials. In 2014, Yang et al. demonstrated for the first time active THz filters based on graphene, in which the frequency of resonance was tuned by controlling the Fermi level on a graphene film [66]. With all the recent progress in developing THz elements for future compact low-cost terahertz systems, several needs are not properly addressed yet. A beam steerer is an essential part of MIMO communications, tunable flat lenses for terahertz cameras, etc., since all of these applications will demand components capable of achieving active beam-shaping to some degree. One of the issues we are trying to address in this work is on approaches towards active beam steering using reconfigurable terahertz metamaterials.

1.6 Structure of this dissertation

In the second chapter of this dissertation, a graphene-based metamaterial phase modulator is proposed. In this device, graphene is integrated within a deep-subwavelength frequency selective surface to form a reconfigurable metamaterial for THz phase modulation. This phase modulator is designed as a building block for future THz beam steerers. From this perspective, our goal was to improve the device efficiency in terms of attainable phase modulation per unit cell area when compared to that of existing metamaterial phase modulators. The proposed devices are deeply-scaled and have the smallest unit cell dimensions demonstrated in the literature. This can lead from a practical perspective to sharper phase gradients and larger directivity.

However, as unit cells are made smaller and smaller, while trying to keep the resonance frequency constant, the performance of these devices in terms of loss degrades. Therefore, in the third chapter of this dissertation, I discuss the geometrical tradeoffs when designing deeply scaled metamaterial phase modulators. In this study two families of deep subwavelength structures, namely spiral resonators and split ring resonators, are considered. Two figures of merit related to device performance are defined, and the effect of the metamaterial geometry on these figures of merit is investigated. Our results show that there is an optimal unit cell size ~$\lambda/20$, which leads to the best performance.

After having discussed graphene-based metamaterials as phase modulators, we try to answer a more general research question: what is the best role that graphene can play when realizing terahertz devices? In other words, is graphene more attractive as a reconfigurable plasmonic material by itself? Or, as a reconfigurable media providing tunability to, otherwise passive, metallic structures? Our simulations and experimental results evidence that graphene/metal hybrid approaches can offer much stronger responses that graphene-only plasmonic structures, and therefore are more suitable for practical terahertz applications. A discussion on this analysis is presented in Chapter 4.

In addition to graphene, we investigated other 2D materials as reconfigurable elements in THz devices. Graphene is a material with zero bandgap, which results in a nonzero minimum conductivity; therefore, all the device designs based on graphene suffer from a finite insertion loss in the off state. However, there are other novel 2D materials with bandgap, which can be used so to achieve reconfigurability and lower loss. One of these materials is Molybdenum disulfide (MoS_2). In Chapter 5, we discuss our investigations on THz metamaterials based on 2D materials beyond graphene.

Furthermore, in Chapter 6, another 2D conductive structure is discussed and studied. The structure under study is not a particular material, as was the case in Chapters 2 to 5, but the 2DEG that is formed at the interface between two complex oxides. These complex oxides are transparent to visible wavelengths as a result of their wide bandgap. The 2DEG under study, in the interface between NTO and STO, has a world-record 2D carrier concentration. By using THz spectroscopy we show that the conductivity and thus mobility at the nanoscale is much larger than the one extracted from DC transport measurements. The large extracted nanoscale conductivity positions these materials at the same conductivity levels typically attainable in high-mobility semiconductors. From this perspective, these materials can be very strong candidates for transparent electronics applications.

We followed this study on highly conductive oxide interfaces, by studying a transparent conducting oxide thin film with record high conductivity levels: $BaSnO_3$ (BSO). Chapter 7 discusses this material and presents our results on its characterization by means of THz spectroscopy. As a result of the high terahertz conductivity in this material, which takes place across a broad frequency window, a visible-transparent / terahertz functional electromagnetic structure is designed and demonstrated to reveal the application potentials of BSO for visible-transparent terahertz applications.

Finally, this dissertation ends in Chapter 8, which discusses conclusions and future work.

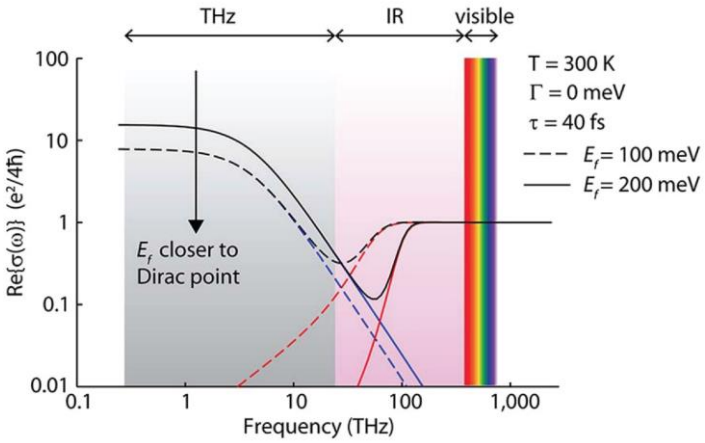

Figure 1.1: Graphene conductivity vs. frequency for different Fermi levels © 2013 IEEE [59]

1.7 References

[1] T. G. Phillips and J. Keene, “Submillimeter astronomy (heterodyne spectroscopy),” *Proc. IEEE*, vol. 80, no. 11, pp. 1662–1678, 1992.

[2] M. Tonouchi, “Cutting-edge terahertz technology,” *Nat. Photonics*, vol. 1, no. 2, pp. 97–105, 2007.

[3] D. T. Leisawitz *et al.*, “Scientific motivation and technology requirements for the SPIRIT and SPECS far-infrared/submillimeter space interferometers,” in *UV, Optical, and IR Space Telescopes and Instruments*, 2000, vol. 4013, pp. 36–47.

[4] J. W. Waters, “Submillimeter-wavelength heterodyne spectroscopy and remote sensing of the upper atmosphere,” *Proc. IEEE*, vol. 80, no. 11, pp. 1679–1701, 1992.

[5] Y.-S. Lee, “Terahertz spectroscopy of atoms and molecules,” in *Principles of Terahertz Science and Technology*, Springer, Boston, MA, 2009, pp. 1–44.

[6] T. R. Globus *et al.*, “THz-spectroscopy of biological molecules,” *J. Biol. Phys.*, vol. 29, no. 2, pp. 89–100, 2003.

[7] B. M. Fischer, M. Walther, and P. U. Jepsen, “Far-infrared vibrational modes of DNA components studied by terahertz time-domain spectroscopy,” *Phys. Med. Biol.*, vol. 47, no. 21, p. 3807, 2002.

[8] A. Rostami, H. Rasooli, and H. Baghban, *Terahertz Technology: Fundamentals and Applications*, 2011 edition. Heidelberg ; New York: Springer, 2011.

[9] H.-B. Liu, H. Zhong, N. Karpowicz, Y. Chen, and X.-C. Zhang, “Terahertz spectroscopy and imaging for defense and security applications,” *Proc. IEEE*, vol. 95, no. 8, pp. 1514–1527, 2007.

[10] J. F. Federici *et al.*, “THz imaging and sensing for security applications—explosives, weapons and drugs,” *Semicond. Sci. Technol.*, vol. 20, no. 7, p. S266, 2005.

[11] B. E. Cole, R. M. Woodward, D. Crawley, V. P. Wallace, D. D. Arnone, and M. Pepper, “Terahertz imaging and spectroscopy of human skin, in-vivo,” in *Proc. SPIE*, 2001, vol. 4276, p. 10.

[12] P. H. Siegel, “Terahertz technology in biology and medicine,” *IEEE Trans. Microw. Theory Tech.*, vol. 52, no. 10, pp. 2438–2447, 2004.

[13] R. Ross and E. P. Benditt, “Wound healing and collagen formation: V. Quantitative electron microscope radioautographic observations of proline-H3 utilization by fibroblasts,” *J. Cell Biol.*, vol. 27, no. 1, p. 83, 1965.

[14] R. M. Woodward, V. P. Wallace, D. D. Arnone, E. H. Linfield, and M. Pepper, “Terahertz pulsed imaging of skin cancer in the time and frequency domain,” *J. Biol. Phys.*, vol. 29, no. 2–3, pp. 257–259, 2003.

[15] R. M. Woodward *et al.*, “Terahertz pulse imaging in reflection geometry of human skin cancer and skin tissue,” *Phys. Med. Biol.*, vol. 47, no. 21, p. 3853, 2002.

[16] R. Bazin and C. Fanchon, “Equivalence of face and volar forearm for the testing of moisturizing and firming effect of cosmetics in hydration and biomechanical studies,” *Int. J. Cosmet. Sci.*, vol. 28, no. 6, pp. 453–461, 2006.

[17] D. Crawley, C. Longbottom, V. P. Wallace, B. Cole, D. Arnone, and M. Pepper, “Three-dimensional terahertz pulse imaging of dental tissue,” *J. Biomed. Opt.*, vol. 8, no. 2, pp. 303–307, 2003.

[18] D. A. Crawley *et al.*, “Terahertz pulse imaging: A pilot study of potential applications in dentistry,” *Caries Res.*, vol. 37, no. 5, pp. 352–359, 2003.

[19] P. C. Ashworth *et al.*, “Terahertz pulsed spectroscopy of freshly excised human breast cancer,” *Opt. Express*, vol. 17, no. 15, pp. 12444–12454, 2009.

[20] A. J. Fitzgerald *et al.*, “Terahertz pulsed imaging of human breast tumors,” *Radiology*, vol. 239, no. 2, pp. 533–540, 2006.

[21] C. Yu, S. Fan, Y. Sun, and E. Pickwell-MacPherson, “The potential of terahertz imaging for cancer diagnosis: A review of investigations to date,” *Quant. Imaging Med. Surg.*, vol. 2, no. 1, p. 33, 2012.

[22] S. Cherry, “Edholm’s law of bandwidth,” *IEEE Spectr.*, vol. 41, no. 7, pp. 58–60, 2004.

[23] C. E. Shannon and W. Weaver, *The Mathematical Theory of Communication*. University of Illinois Press, Chicago, IL, 1998.

[24] B. Ferguson and X.-C. Zhang, “Materials for terahertz science and technology,” *Nat. Mater.*, vol. 1, no. 1, pp. 26–33, 2002.

[25] G. Thomas, “Materials science - Invisible circuits,” *Nature*, vol. 389, no. 6654, pp. 907–908, Oct. 1997.

[26] H. Kawazoe, M. Yasukawa, H. Hyodo, M. Kurita, H. Yanagi, and H. Hosono, “P-type electrical conduction in transparent thin films of CuAlO2,” *Nature*, vol. 389, no. 6654, pp. 939–942, 1997.

[27] M. Ohring, *Materials Science of Thin Films*. Academic Press, San Diego, CA, 2002.

[28] P. F. Carcia, R. S. McLean, M. H. Reilly, and G. Nunes Jr, "Transparent ZnO thin-film transistor fabricated by rf magnetron sputtering," *Appl. Phys. Lett.*, vol. 82, no. 7, pp. 1117–1119, 2003.

[29] R. L. Hoffman, B. J. Norris, and J. F. Wager, "ZnO-based transparent thin-film transistors," *Appl. Phys. Lett.*, vol. 82, no. 5, pp. 733–735, 2003.

[30] S. Masuda, K. Kitamura, Y. Okumura, S. Miyatake, H. Tabata, and T. Kawai, "Transparent thin film transistors using ZnO as an active channel layer and their electrical properties," *J. Appl. Phys.*, vol. 93, no. 3, pp. 1624–1630, 2003.

[31] K. Parkhi, "Transparent electronics: Technologies and global markets," BCC research, Market Research Reports IFT065A, Aug. 2010.

[32] J. F. Wager, D. A. Keszler, and R. E. Presley, *Transparent Electronics*. Springer Science & Business Media, New York, NY, 2007.

[33] K. Ellmer, "Past achievements and future challenges in the development of optically transparent electrodes," *Nat. Photonics*, vol. 6, no. 12, pp. 809–817, 2012.

[34] T. Minami, "Transparent conducting oxide semiconductors for transparent electrodes," *Semicond. Sci. Technol.*, vol. 20, no. 4, p. S35, 2005.

[35] S. Calnan and A. N. Tiwari, "High mobility transparent conducting oxides for thin film solar cells," *Thin Solid Films*, vol. 518, no. 7, pp. 1839–1849, 2010.

[36] X. Crispin *et al.*, "The origin of the high conductivity of poly (3, 4-ethylenedioxythiophene)-poly (styrenesulfonate)(PEDOT-PSS) plastic electrodes," *Chem. Mater.*, vol. 18, no. 18, pp. 4354–4360, 2006.

[37] M. Vosgueritchian, D. J. Lipomi, and Z. Bao, "Highly conductive and transparent PEDOT: PSS films with a fluorosurfactant for stretchable and flexible transparent electrodes," *Adv. Funct. Mater.*, vol. 22, no. 2, pp. 421–428, 2012.

[38] H. Ohta, M. Orita, M. Hirano, H. Tanji, H. Kawazoe, and H. Hosono, "Highly electrically conductive indium–tin–oxide thin films epitaxially grown on yttria-stabilized zirconia (100) by pulsed-laser deposition," *Appl. Phys. Lett.*, vol. 76, no. 19, pp. 2740–2742, 2000.

[39] J.-Y. Lee, S. T. Connor, Y. Cui, and P. Peumans, "Solution-processed metal nanowire mesh transparent electrodes," *Nano Lett.*, vol. 8, no. 2, pp. 689–692, 2008.

[40] P. Lee *et al.*, “Highly stretchable and highly conductive metal electrode by very long metal nanowire percolation network,” *Adv. Mater.*, vol. 24, no. 25, pp. 3326–3332, 2012.

[41] K. S. Kim *et al.*, “Large-scale pattern growth of graphene films for stretchable transparent electrodes,” *nature*, vol. 457, no. 7230, pp. 706–710, 2009.

[42] F. Bonaccorso, Z. Sun, T. Hasan, and A. C. Ferrari, “Graphene photonics and optoelectronics,” *Nat. Photonics*, vol. 4, no. 9, pp. 611–622, 2010.

[43] K. S. Novoselov *et al.*, “Two-dimensional atomic crystals,” *Proc. Natl. Acad. Sci. U. S. A.*, vol. 102, no. 30, pp. 10451–10453, 2005.

[44] A. K. Geim, “Graphene prehistory,” *Phys. Scr.*, vol. 2012, no. T146, p. 014003, 2012.

[45] C. Berger *et al.*, “Electronic confinement and coherence in patterned epitaxial graphene,” *Science*, vol. 312, no. 5777, pp. 1191–1196, 2006.

[46] W. A. De Heer *et al.*, “Epitaxial graphene,” *Solid State Commun.*, vol. 143, no. 1, pp. 92–100, 2007.

[47] A. Reina *et al.*, “Large area, few-layer graphene films on arbitrary substrates by chemical vapor deposition,” *Nano Lett.*, vol. 9, no. 1, pp. 30–35, 2008.

[48] S. Bae *et al.*, “Roll-to-roll production of 30-inch graphene films for transparent electrodes,” *Nat. Nanotechnol.*, vol. 5, no. 8, pp. 574–578, 2010.

[49] S. Stankovich *et al.*, “Synthesis of graphene-based nanosheets via chemical reduction of exfoliated graphite oxide,” *carbon*, vol. 45, no. 7, pp. 1558–1565, 2007.

[50] C. Soldano, A. Mahmood, and E. Dujardin, “Production, properties and potential of graphene,” *Carbon*, vol. 48, no. 8, pp. 2127–2150, 2010.

[51] A. Reina *et al.*, “Growth of large-area single-and bi-layer graphene by controlled carbon precipitation on polycrystalline Ni surfaces,” *Nano Res.*, vol. 2, no. 6, pp. 509–516, 2009.

[52] J. Cai *et al.*, “Atomically precise bottom-up fabrication of graphene nanoribbons,” *Nature*, vol. 466, no. 7305, pp. 470–473, 2010.

[53] C. Mattevi, H. Kim, and M. Chhowalla, “A review of chemical vapour deposition of graphene on copper,” *J. Mater. Chem.*, vol. 21, no. 10, pp. 3324–3334, 2011.

[54] P. Y. Huang *et al.*, “Grains and grain boundaries in single-layer graphene atomic

patchwork quilts," *Nature*, vol. 469, no. 7330, pp. 389–392, 2011.

[55] J. W. Suk *et al.*, "Transfer of CVD-grown monolayer graphene onto arbitrary substrates," *ACS Nano*, vol. *5*, no. 9, pp. 6916–6924, 2011.

[56] E. H. Lock *et al.*, "High-quality uniform dry transfer of graphene to polymers," *Nano Lett.*, vol. 12, no. 1, pp. 102–107, 2011.

[57] C. J. L. de la Rosa *et al.*, "Frame assisted H2O electrolysis induced H2 bubbling transfer of large area graphene grown by chemical vapor deposition on Cu," *Appl. Phys. Lett.*, vol. 102, no. 2, p. 022101, 2013.

[58] Y. Chen, X.-L. Gong, and J.-G. Gai, "Progress and challenges in transfer of large-area graphene films," *Adv. Sci.*, vol. 3, no. 8, 2016.

[59] B. Sensale-Rodriguez, R. Yan, L. Liu, D. Jena, and H. G. Xing, "Graphene for reconfigurable terahertz optoelectronics," *Proc. IEEE*, vol. 101, no. 7, pp. 1705–1716, 2013.

[60] X. Du, I. Skachko, A. Barker, and E. Y. Andrei, "Approaching ballistic transport in suspended graphene," *Nat. Nanotechnol.*, vol. 3, no. 8, pp. 491–495, 2008.

[61] B. Sensale-Rodriguez *et al.*, "Broadband graphene terahertz modulators enabled by intraband transitions," *Nat. Commun.*, vol. 3, p. ncomms1787, 2012.

[62] B. Sensale-Rodriguez *et al.*, "Unique prospects for graphene-based terahertz modulators," *Appl. Phys. Lett.*, vol. 99, no. 11, p. 113104, 2011.

[63] L. Ju *et al.*, "Graphene plasmonics for tunable terahertz metamaterials," *Nat. Nanotechnol.*, vol. 6, no. 10, pp. 630–634, 2011.

[64] D.-W. Shin, J. H. Lee, Y.-H. Kim, S. M. Yu, S.-Y. Park, and J.-B. Yoo, "A role of HNO3 on transparent conducting film with single-walled carbon nanotubes," *Nanotechnology*, vol. 20, no. 47, p. 475703, 2009.

[65] D. R. Smith, J. B. Pendry, and M. C. Wiltshire, "Metamaterials and negative refractive index," *Science*, vol. 305, no. 5685, pp. 788–792, 2004.

[66] K. Yang, S. Liu, S. Arezoomandan, A. Nahata, and B. Sensale-Rodriguez, "Graphene-based tunable metamaterial terahertz filters," *Appl. Phys. Lett.*, vol. 105, no. 9, p. 093105, 2014.

[67] R. Yan, B. Sensale-Rodriguez, L. Liu, D. Jena, and H. G. Xing, "A new class of electrically tunable metamaterial terahertz modulators," *Opt. Express*, vol. 20, no. 27, pp. 28664–28671, 2012.

[68] D. Schurig *et al.*, “Metamaterial electromagnetic cloak at microwave frequencies,” *Science*, vol. 314, no. 5801, pp. 977–980, 2006.

[69] H. Yan *et al.*, “Tunable infrared plasmonic devices using graphene/insulator stacks,” *Nat. Nanotechnol.*, vol. 7, no. 5, pp. 330–334, 2012.

[70] J. S. Gomez-Diaz *et al.*, “Self-biased reconfigurable graphene stacks for terahertz plasmonics,” *ArXiv Prepr. ArXiv14053320*, 2014.

[71] S. H. Lee *et al.*, “Switching terahertz waves with gate-controlled active graphene metamaterials,” *Nat. Mater.*, vol. 11, no. 11, pp. 936–941, 2012.

[72] F. Valmorra *et al.*, “Low-bias active control of terahertz waves by coupling large-area CVD graphene to a terahertz metamaterial,” *Nano Lett.*, vol. 13, no. 7, pp. 3193–3198, 2013.

[73] R. Degl’Innocenti *et al.*, “Low-bias terahertz amplitude modulator based on split-ring resonators and graphene,” *ACS Nano*, vol. 8, no. 3, pp. 2548–2554, 2014.

[74] M. Tamagnone, A. Fallahi, J. R. Mosig, and J. Perruisseau-Carrier, “Fundamental limits and near-optimal design of graphene modulators and non-reciprocal devices,” *Nat. Photonics*, vol. 8, no. 7, pp. 556–563, 2014.

[75] R. Yan, S. Arezoomandan, B. Sensale-Rodriguez, and H. G. Xing, “Exceptional terahertz wave modulation in graphene enhanced by frequency selective surfaces,” *ACS Photonics*, vol. 3, no. 3, pp. 315–323, 2016.

[76] W. Zouaghi, D. Voss, M. Gorath, N. Nicoloso, and H. G. Roskos, “How good would the conductivity of graphene have to be to make single-layer-graphene metamaterials for terahertz frequencies feasible?,” *Carbon*, vol. 94, pp. 301–308, 2015.

CHAPTER 2

GRAPHENE-BASED ELECTRICALLY RECONFIGURABLE DEEP-SUBWAVELENGTH METAMATERIALS FOR ACTIVE CONTROL OF THZ LIGHT PROPAGATION

2.1 Abstract

This work studies the terahertz light propagation through graphene-based reconfigurable metasurfaces where the unit cell dimensions are much smaller than the terahertz wavelength. The proposed devices, which pose deep-subwavelength unit cell and active region dimensions, can operate as amplitude and/or phase modulators in certain specific frequency bands determined by the device geometry. Reconfigurability is attained via electrostatically tuning the optical conductivity of patterned graphene layers, which are strategically located in each unit cell. The ultra-small unit cell dimensions can be advantageous for beam shaping applications.

2.2 Introduction

Future compact low-cost terahertz systems, such as beam steerers for MIMO communications approaches, tunable flat lenses for IR/THz cameras, and so on, will demand components capable of achieving some degree of beam shaping. Currently there

The material provided in this chapter is available at: Applied Physics A, 117 (2), pp. 423-426. Reprinted and adapted with permission from Springer.

are only a small number of studies proposing or demonstrating devices achieving terahertz beam steering (e.g., [1-4]). Although these devices represent a significant technological advance, most of them are bulky in size (e.g., either require mechanical actuation or external lasers for optical excitations) and, therefore, unsuitable for compact integration [1-3]. From this point of view, there is a need for compact devices enabling active terahertz beam shaping.

In this context, active semiconductor-based metamaterials were shown capable— at certain frequencies— of producing phase modulation of an arbitrary terahertz beam, whereas not affecting the amplitude of the transmitted wave [5]. This is of special interest in order to construct arbitrary phase gradients, which in turn can shape a beam in accordance to the generalized laws of reflection and refraction [6]. Since in order to achieve maximum control over the properties of the transmitted terahertz beam, the phase gradient should be maximized, it is of interest to develop metamaterials capable of simultaneously: (1) achieving the largest phase modulation per unit cell and (2) having the smallest unit cell dimensions.

This work presents a planar deep-subwavelength active metamaterial (i.e., a metamaterial with unit cell dimensions $<< \lambda/10$). By independently biasing each of the unit cells (meta-atoms), reconfigurable planar phase gradients might be constructed, which can in turn be employed for terahertz beam shaping. The ultrascaled dimensions of the proposed meta-atoms can allow for construction of more abrupt phase gradients than conventional (i.e., no ultrascaled) metasurfaces, which consequently can lead to larger degrees of reconfigurability. Owed to its intrinsic two-dimensional nature, low-cost, and ease of integration [7], graphene is proposed as the active terahertz material in these

devices. The active area of the device— area covered by graphene— is just a 0.5% of the total unit cell area. Therefore, the proposed devices might also enable very fast switching.

2.3 Device structure

Shown in Fig. 2.1(a-b) are the structure of the proposed device, which consists of an array of spiral resonators, and the detail of one unit cell single spiral resonator, respectively. An active graphene layer is placed in the center of each unit cell; its electromagnetic properties and therefore the effective properties of the device can be controlled via controlling the Fermi level of graphene and thus its density of states available for intraband transitions [8-11]. Although graphene metamaterials have been widely employed in devices modulating the amplitude of a transmitted terahertz beam (e.g., [12-14]), graphene-based structures controlling phase have not yet been proposed in the literature.

Actuation over the graphene optical conductivity can be achieved electrostatically via either gating graphene with another graphene layer (self-gated structure) [15-17] or via employing ion-gel as the gating element [18]. Since the optical conductivity of graphene at terahertz frequencies follows a Drude-like dispersion:

$$\sigma(\omega) = \frac{\sigma_{DC}}{1 - j\omega\tau} \tag{2.1}$$

where τ is the momentum relaxation time for carriers, $\omega = 2\pi f$ is angular frequency, and:

$$\sigma_{DC} = q\mu n_s \tag{2.2}$$

is its DC electrical conductivity. It can be easily understood that controlling the charge density n_s in graphene allows us to control its optical conductivity $\sigma(\omega)$. In Eqn. (2.2) q represents electron charge, μ is carrier mobility, and n_s is carrier density. Details of the

self-gated and ion-gel gating structures are sketched in Fig. 2.2(a-b), respectively. As shown in Fig. 2.2(a) by applying a finite voltage between the two capacitively coupled graphene layers, carriers of the opposite type accumulate in each layer. Therefore the overall carrier density and thus optical conductivity can be controlled. For the situation represented in the lower sketch of Fig. 2.2(a) the total terahertz optical conductivity of the structure is given by the sum of the hole conductivity of the bottom layer and the electron conductivity of the top layer.

For a given linear THz polarization metal stripes perpendicular to the polarization direction can be employed as electrodes without altering the transmission properties of the structure, as illustrated in Fig. 2.1(c).

2.4 Discussion

Numerical simulations were performed employing HFFS; graphene was modeled as a 1-nm conductive layer with variable conductivity in the range from 0.1 to 4mS (conductivity can be modified in practice via gating the structure as discussed in the previous section). Polyimide was employed as substrate, SiN as spacer, and the metal was chosen as 100-nm thick gold. The unit cell dimension is 54-μm, the spacing between metal stripes is 3-μm, and the width of the metal stripes is 2-μm. The thickness of the SiN layer is 0.1-μm, whereas the thickness of the substrate was set to 2-μm.

Figure 2.3(a) shows the simulated transmission amplitude versus frequency for different graphene conductivities. Three resonant features are observed, one at around 0.30-040THz, other at around 0.70THz, and the third one at around 1.05THz. At these frequencies the device can operate as an amplitude modulator.

As discussed by Chen *et al.*, the terahertz transmission amplitude and phase are not independent of each other, but are related by Kramers-Kronig (KK) relations [5]. Near frequencies where the amplitude has no strong dependence on the applied voltage bias (has not dependence on graphene conductivity), the phase experiences a maximum shift. In contrast at the frequencies where maximum amplitude modulation is achieved no phase modulation takes place. Shown in Fig. 2.3(b) is phase versus frequency for different graphene conductivities. It is observed that at 0.32 THz, 0.65 THz, and 0.75 THz maximum phase modulation can be achieved. It is worth observing that at these frequencies the amplitude modulation is negligible (see Fig. 2.2(a)), in accordance with the observation by *Chen et al.* [5]. The phase modulation, when tuning graphene conductivity from 0.1 mS to 4 mS, at 0.32 THz, 0.65 THz, and 0.75 THz is 42°, 40°, and 46°, respectively.

Shown in Table 2.1 are the unit cell parameters for several reconfigurable metamaterials proposed in the literature ([5], [19]). The frequency reported for this work is 0.32 THz, at which a phase modulation of 42° was obtained. It can be observed that the devices here discussed can achieve similar phase modulation to those previously reported in the literature, but with unit cell size over wavelength ratio much smaller than that of these prior works. The unit cell to wavelength ratio here reported is just 0.06, which is 2.5 times and 3.33 smaller than those reported by Chen *et al.* and Kafesaki *et al.*, respectively [5, 19]. Moreover, the transmission amplitude at this frequency -40%- is similar to that reported by Kafesaki *et al.* also 40% [19] but smaller than that reported by Chen *et al.* 60% [5]. The transmission amplitude in these cases indicates the loss introduced by the structure. From these points of view, due to the smallest unit cell to wavelength ratio and

comparable phase modulation at resonance, the spiral-resonator graphene-based metamaterials here proposed can promise more abrupt phase gradients than the other two geometries previously analyzed in the literature and therefore provide advantages for terahertz beam steering applications.

The active area dimension in each unit cell is 4μm x 4μm, and thus active area to unit cell area ratio is just 0.5%. Since the speed of these devices is constrained by *RC* time constant limitations, switching speed becomes proportional to the active area, and thus the smaller the active area the fastest the switching speed (see Ref. [10]). For comparison, the active area to unit cell area ratio of previously proposed graphene active terahertz metamaterials lies between 50% and 100% (e.g., [12-15, 18]) with reported switching in the order of 10-kHz (e.g., Ref. [10, 20]); via reducing the active area switching speeds associated with GHz frequencies can be attained.

2.5 Conclusion

We have proposed graphene-based electrically reconfigurable metasurfaces, which poses deep-subwavelength unit cell/active region dimensions. The devices here proposed can achieve similar phase modulation to other devices previously proposed in the literature, but with 2.5X smaller unit cell to wavelength ratio. These ultra-small unit cell dimensions can be advantageous for beam shaping applications.

2.6 Acknowledgement

The authors acknowledge the support from the NSF MRSEC program at the University of Utah under grant # DMR 1121252 and from the NSF CAREER award # 1351389 (monitored by Dimitris Pavlidis).

Table 2.1: Phase modulation in reconfigurable metamaterials.

	Chen *et al.* [5]	Kafesaki *et al.* [19]	This work
Unit cell dimension (μm^2)	50	50	54
Frequency (THz)	0.88	1.20	0.32
Phase modulation	32°	45°	42°
Transmission amplitude	60%	40%	40%
Unit cell to wavelength ratio	0.15	0.20	**0.06**

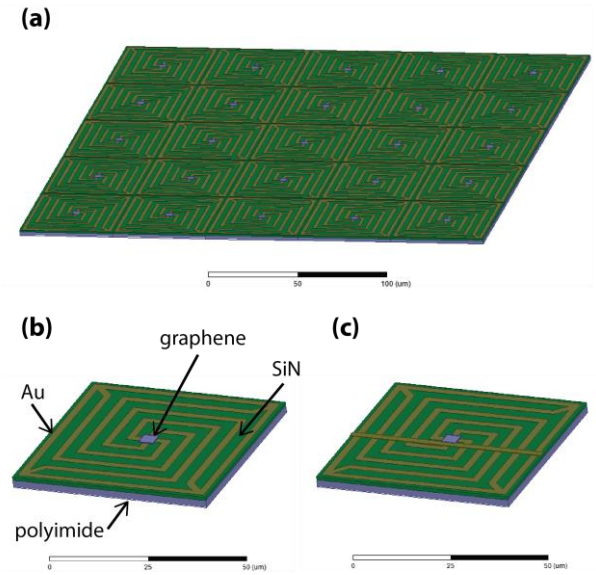

Figure 2.1: (a) Sketch of the device structure. (b) Detail of one element of the array (meta-cell). (c) Gating structure (electrode configuration) for electrically controlling the graphene conductivity.

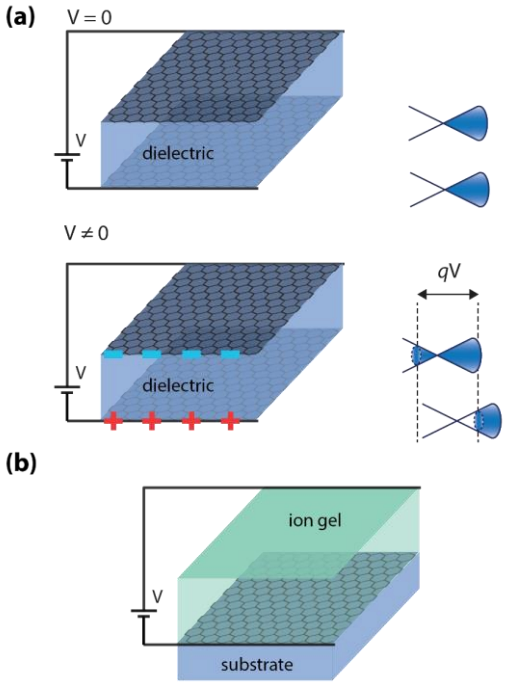

Figure 2.2: (a) Sketch of a self-gated graphene pair. At zero voltage both the top and bottom graphene layers are assumed to be at Dirac point and thus the total free charge density and the effective conductivity approaches zero. When a finite voltage is applied carriers of opposite type accumulate in the graphene layers. (b) Sketch of an ion-gel gated graphene layer.

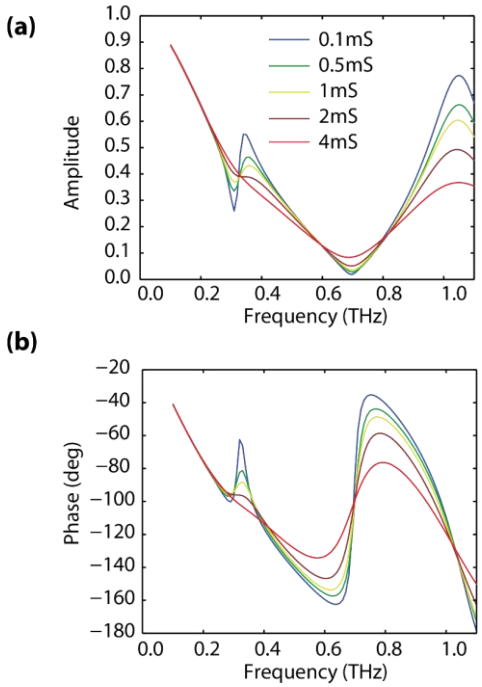

Figure 2.3: (a) Amplitude and (b) phase transmission vs. frequency, for different graphene conductivities. Graphene conductivity is varied from 0.1mS to 4mS.

2.7 References

[1] Y. Monnai, C. Jansen, H. Hillmer, M. Koch, and H. Shinod, "Terahertz beam steering and variable focusing using programmable diffraction gratings," *Optics Express* 21(2): 2347-2354, 2013.

[2] S. Busch, B. Scherger, M. Scheller, and M. Koch, "Optically controlled terahertz beam steering and imaging," *Opt. Lett.* 37(8): 1391–1393, 2012.

[3] H. Fuser and M. Bieler, "Terahertz beam steering by optical coherent control," *Appl. Phys. Lett.* 102: 251109, 2013.

[4] B. Scherger, M. Reuter, M. Scheller, K. Altmann, N. Vieweg, R. Dabrowski, J. A. Deibel, and M. Koch, "Discrete terahertz beam steering with an electrically controlled liquid crystal device," *J. Infrared Milli. Terahz Waves* 33(11): 1117–1122, 2012.

[5] H. T. Chen, W. J. Padilla, M. J. Cich, A. K. Azad, R. D. Averitt, and A. J. Taylor, "A metamaterial solid-state terahertz phase modulator," *Nature Photon.* 3(3): 141–151, 2009.

[6] N. Yu, P. Genevet, M. A. Kats, F. Aieta, J. P. Tatienne, F. Capasso, and Z. Gaburro, "Light propagation with phase discontinuities: generalized laws of reflection and refraction," *Science* 334: 333, 2011.

[7] B. Sensale-Rodriguez, R. Yan, L. Liu, D. Jena, and H. G. Xing, "Graphene for reconfigurable terahertz optoelectronics," *Proceedings of the IEEE* 101(7): 1705-1706, 2013.

[8] J. Horng, C.-F. Chen, B. Geng, C. Girit, Y. Zhang, Z. Hao, H. A. Bechtel, M. Martin, A. Zettl, M. F. Crommie, Y. R. Shen, and F. Wang, "Drude conductivity of Dirac fermions in graphene," *Phys. Rev. B* 83: 165113, 2011.

[9] B. Sensale-Rodriguez *et al*., "Unique prospects for graphene-based terahertz Modulators," *Appl. Phys. Lett.* 99: 113104, 2011.

[10] B. Sensale-Rodriguez, R. Yan, M. M. Kelly, T. Fang, K. Tahy, W. S. Hwang, D. Jena, L. Liu, and H. G. Xing, "Broadband graphene terahertz modulators enabled by intraband transitions," *Nat. Commun*. 3: 780, 2012.

[11] L. Ren, Q. Zhang, J. Yao, Z. Sun, R. Kaneko, Z. Yan, S. Nanot, Z. Jin, I. Kawayama, M. Tonouchi, J. M. Tour, and J. Kono, "Terahertz and infrared spectroscopy of gated large-area graphene," *Nano Letters* 12: 3711, 2012.

[12] S. H. Lee, M. Choi, T.-T. Kim, S. Lee, M. Liu, X. Yin, H. K. Choi, S. S. Lee, C.-G. Choi, S.-Y. Choi, X. Zhang, and B. Min "Switching terahertz waves with gate-

controlled active graphene metamaterials," *Nature Mater.* 11: 936-941, 2012.

[13] S. H. Lee, J. Choi, H. D. Kim, H. Choi, and B. Min "Ultrafast refractive index control of a terahertz graphene metamaterial," *Scientific Reports* 3: 2135, 2013.

[14] W. Gao, J. Shu, K. Reichel, D. V. Nickel, X. He, G. Shi, R. Vajtai, P. M. Ajayan, J. Kono, D. M. Mittleman, and Q. Xu, "High-contrast terahertz wave modulation by gated graphene enhanced by extraordinary transmission through ring apertures," *Nano Letters* 14(3) : 1242-1248, 2014.

[15] R. Yan, B. Sensale-Rodriguez, L. Liu, D. Jena, and H. G. Xing "A new class of tunable metamaterial terahertz modulators," *Optics Express* 20(27): 28664-28671, 2012.

[16] S. J. Koester, and M. Li "High-speed waveguide-coupled graphene-on-graphene optical modulators," *Appl. Phys. Lett.* 100: 171107, 2012.

[17] M. Liu, X. Yin, and X. Zhang "Double-layer graphene optical modulator," *Nano Letters* 12: 1482–1485, 2012.

[18] L. Ju, B. Geng, J. Horng, C. Girit, M. Martin, Z. Hao, H. A. Bechtel, X. Liang, A. Zettl, Y. R. Shen, and F. Wang "Graphene plasmonics for tunable terahertz metamaterials," *Nat. Nanotechnol.* 6: 630–634, 2011.

[19] M. Kafesaki, N. H. Shen, S. Tzortzakis, and C. M. Soukoulis, "Optically switchable and tunable terahertz metamaterials through photoconductivity," *J. Opt.* 14: 114008, 2012.

[20] B. Sensale-Rodriguez, R. Yan, S. Rafique, M. Zhu, W. Li, X. Liang, D. Gundlach, V. Protasenko, M. M. Kelly, D. Jena, L. Liu, and H. G. Xing "Extraordinary control of terahertz beam reflectance in graphene electro-absorption modulators," *Nano Letters* 12: 4518–4522, 2012.

CHAPTER 3

GEOMETRICAL TRADEOFFS IN GRAPHENE-BASED DEEPLY-SCALED ELECTRICALLY RECONFIGURABLE METASURFACES

3.1 Abstract

In this work we study the terahertz light propagation through deeply-scaled graphene-based reconfigurable metasurfaces, i.e. metasurfaces with unit cell dimensions much smaller than the terahertz wavelength. Two types of deeply-scaled metacell geometries are analyzed and compared, which consist of: (i) multi split ring resonators, and (ii) multi spiral resonators. Two figures of merit, related to: (a) the loss and (b) the degree of reconfigurability achievable by such metamaterials —when applied in beam shaping applications— are introduced and discussed. Simulations of these two types of deep-subwavelength geometries, when changing the metal coverage fraction, show that there is an optimal coverage fraction that gives the best tradeoff in terms of loss versus degree of reconfigurability. For both types of geometries the best tradeoff occurs when the area covered by the metallic region is around 40% of the metacell total area. From this point of view, deeply-scaled metamaterials can indeed provide a superior performance for beam shaping applications when compared to not deeply-scaled ones; however,

---

The material provided in this chapter is available at: Scientific Report. 2015; 5: 8834.
Reprinted and adapted with permission from Nature Publishing Group.

counterintuitively, employing very highly-packed structures might not be beneficial for such applications.

3.2 Introduction

Terahertz technology is a growing technological field, which in recent years has been finding multiple emerging applications in diverse areas, including medical imaging, biochemical sensing, security, wireless communications, and so on.[1] In this context, future compact low-cost terahertz systems, such as beam steerers for MIMO communications, tunable flat lenses for terahertz cameras, etc., will demand components capable of achieving active beam-shaping at some degree. Reconfigurable terahertz metamaterials[2] were shown capable of modulating the phase of an arbitrary terahertz beam,[3] which is of special interest for beam-shaping applications. In this regard, via independently biasing each metacell, arbitrary phase gradients can be constructed,[3] which in turn can shape the reflected or transmitted beams in accordance with the recently proposed generalized laws of reflection and refraction (generalized Snell's law).[4]

When a phase gradient is placed in the interface between two media of refractive index n_t and n_i, Snell's law of transmission should be rephrased as the generalized law of reflection and refraction[4]:

$$\sin(\theta_t)\, n_t - \sin(\theta_i)\, n_i = \frac{\lambda_0}{2\pi}\frac{d\phi}{dx}, \tag{3.1}$$

where θ_i and θ_t are the angle of incidence and the transmitted angle, respectively, λ_0 is the vacuum terahertz wavelength, and $d\phi/dx$ represents the phase gradient. Assuming normal incidence and $n_i = n_t = 1$, Eqn. (3.1) can be rewritten as:

$$\sin(\theta_t) = \frac{\lambda_0}{2\pi}\frac{d\phi}{dx}\,. \qquad (3.2)$$

Therefore, it can be easily seen that the shape of the transmitted beam can be arbitrarily controlled via designing an adequate phase gradient. For instance, assuming an incident collimated beam, a linear phase gradient can tilt the transmitted beam, whereas a parabolic phase gradient can focus it. Therefore, the use of electrically-driven reconfigurable metamaterial phase modulators for constructing these arbitrary phase gradients is of interest. However, in order to enable the design of these arbitrary phase gradients, each metacell in the device should be able to provide: (a) the same transmission amplitude, and (b) 360° (2π) control over the transmitted phase. In this context, it can be observed, as discussed by Chen *et al.*,[3] that the terahertz transmission amplitude and phase through a metacell are not independent of each other, but they are related by Kramers-Kronig (KK) relations. At near frequencies where the amplitude has a strong dependence on the applied voltage bias, the phase experiences a maximum shift. In contrast at the frequencies where maximum amplitude modulation is achieved no phase modulation takes place. From this point of view (a) is guaranteed. Since terahertz metamaterial phase modulators proposed to date exhibit phase modulation much smaller than 360° (see Ref.[3, 5]), epitaxial stacking of multiple layers[3] is necessary in order to achieve (b), which in turn increases the loss in the device. Moreover, construction of arbitrary phase gradients is also limited by the geometrical length of each unit cell. This is due to the fact that, when employing metamaterials, a continuous phase gradient is approximated by a discretely spatially-varying one. From this point of view, the smaller the unit cell length (when compared to the target terahertz wavelength), the better one can approximate an arbitrary phase gradient, and therefore the more functionality and better performance the metamaterial beam shaper

might achieve. In this context, a problem of metamaterial structures proposed to-date as phase modulators is that the unit cell to wavelength ratio is not small enough to provide good performance. For instance, in order to provide ~90° control over the transmission angle using a 10 element phase-gradient discretization, a unit cell length < $\lambda_0/10$, thus a unit cell to wavelength ratio <0.1, is required. Terahertz metamaterial phase shifters reported to-date have unit cell to wavelength ratios in the order of ~0.15/~0.2 (see Ref.[3, 5]). From this point of view, *one of the main challenges of terahertz metamaterial phase modulators is: designing a metamaterial with small unit cell to wavelength ratio, which has a large phase modulation and large transmission at the frequencies at which maximum phase modulation takes place.* In this work, the terahertz (THz) light propagation through deeply-scaled graphene-based reconfigurable metasurfaces is studied in the context of beam-shaping applications. Although graphene is used as an example of reconfigurable semiconductor in these devices, the discussion presented here is general enough and the results are also valid if employing other semiconductor materials.

3.3 Results

Two types of deep-subwavelength metamaterial geometries are studied and compared. These consist of: (i) *multi spiral resonators* (MSRs), and (ii) *multi split ring resonators* (MSRRs), as depicted in Fig. 3.1(a) and Fig. 3.1(b), respectively. A sheet of graphene was considered as the tunable element to reconfigure the terahertz transmission properties of the metamaterial,[6-8] which was placed in some strategic regions of the device, as depicted in Fig. 3.1. The electromagnetic properties of this graphene layer, and therefore the effective properties of the metamaterial, can be adjusted via controlling the Fermi level

of graphene and therefore its density of states available for intraband transitions and thus its optical conductivity.[6] Although graphene metamaterials have been widely employed in devices modulating the amplitude of a transmitted terahertz beam,[9-12] to the author's knowledge, graphene-based terahertz metasurfaces controlling the phase of a transmitted terahertz beam under normal incidence, have not yet been proposed to-date. In terms of reflection, graphene-based metamaterials have theoretically been shown capable of modulating phase in reflect-array geometries[13]; however, these structures do not provide constant amplitude of reflection when the phase is reconfigured. Actuation over the graphene terahertz optical conductivity can be achieved electrostatically via either gating graphene with another graphene layer (self-gated structure)[14], or via employing ion-gel as the gating element.[15]

Shown in Fig. 3.2 are the characteristic transmission and phase frequency responses as a function of graphene conductivity for one of these metamaterials (a MSR with 30% metal to unit cell area coverage fraction). Maximum phase modulation, 108°, was observed at 500GHz; at this frequency the transmittance was found to be 20%, independently of the graphene conductivity.

Metacells consisting of MSRRs and MSRs were numerically simulated. In order to extract useful information regarding the design tradeoffs in these structures, simulations were performed by changing the metal coverage fraction in each of both geometries. The width of the metal rings/spirals was set to 2-μm, which is a dimension comparable with that of the minimum features achievable in optical lithography; the unit cell edge length was taken between 52-μm and 58-μm (depending on the particular metacell). The graphene sheet area was set to 4-μm by 4-μm in the MSR structure and 2-mm by 4-μm in the MSRR

structure. Therefore, a larger coverage fraction translates into: (a) a larger number of rings and smaller spacing between adjacent rings for the MSRR metacell geometries, or (b) a larger number of turns and smaller spacing in-between metals for the MSR metacell geometries. Shown in Fig. 3.3 are the sketches of the eight simulated devices (4 MSRR geometries and 4 MSR geometries, each of them having a different metal coverage fraction); the results of these simulations are shown in Table 3.1 (where f_p stands for the frequency at which maximum phase modulation takes place).

3.4 Discussion

As discussed in the introductory section, for beam shaping applications, an ideal metamaterial geometry should provide: (i) large phase modulation, (ii) large transmittance, and (iii) small unit cell to wavelength ratio. Arbitrary phase gradients need to be constructed when reconfiguring the phase-shift inserted by each metacell. Therefore, a full control of the transmitted phase, i.e. between 0 and 360°, is desirable in each unit cell in order to achieve truly arbitrary designs. But the phase modulation achievable by each metacell is finite, e.g., prior metamaterial phase-modulator proposals[3, 5] show phase modulation < 50°; therefore, epitaxial stacking of layers is required in order to obtain a 360° control over phase in each metacell. When many layers are epitaxially stacked, although the phase shifts can be added,[3] loss increases with number of layers, which is not desirable. From this point of view, the following figure of merit, related to loss, is defined: $FoM_1 = PM \times T / ([360°] \times [100\ \%])$, where PM is the metacell maximum attainable phase modulation, and T is the transmittance through the metacell at the frequency where maximum phase modulation takes place. For an ideal metacell geometry FoM_1 should

approach unity (since *PM* and *T* are bounded by 360° and 100%, respectively); the larger the FoM_1 the more suitable a metamaterial geometry is for beam steering, i.e. the less loss the device will provide. But also, a small unit cell to wavelength ratio is required in order to construct sharp phase gradients, which are needed, for instance, in order to achieve large swings in beam steering applications as discussed in the introductory section. From this point of view, a second figure of merit is defined: $FoM_2 = L / \lambda_P$, where L is the edge-length of the metacell and λ_p is the wavelength associated with the frequency at which maximum phase modulation takes place. For an ideal metacell geometry FoM_2 should approach zero, the smaller the FoM_2 the most suitable a metamaterial geometry is for beam steering.

As depicted in Table 3.1, it was observed that for MSRRs, the resonance always red-shifts as the metal coverage fraction is increased. However, for MSRs, when the coverage fraction is increased, the resonance frequency first starts red-shifting and then blue-shifts. Moreover, if the metal coverage fraction is further increased (as depicted in Fig. 3.4), the response becomes even less monotonic. The first blue-shift is observed when the metal coverage fraction is increased to larger values (i.e. from 50% to 64%). The trends observed in both structures can be qualitatively explained with an equivalent circuit model (the series of an equivalent inductance and an equivalent capacitance), see Ref.[16,17] For instance, for the case of MSRRs, the equivalent inductance (L_0) is given by the average inductance of the rings. Therefore, the unit cell size will be determinant in L_0; since for the simulated structures the unit cell dimensions remain almost constant, the equivalent inductance can be considered as independent of the metal coverage fraction. Shown in Fig. 3.5(a)-(b) are sketches of the equivalent circuit models for MSR and MSRR

geometries, respectively. Here C_0 is the total capacitance (capacitance between two adjacent rings) and L_0 is the equivalent inductance; in the figure it is assumed that this capacitance, which is related to the spacing between rings, remains constant and its value is C_0. It is worth mentioning that effects such as the capacitance between nonadjacent rings and the resistances arising from losses in the metal and the dielectric will be neglected. As the metal coverage fraction increases (by adding more turns to the structure) the total effective capacitance of the structure increases as depicted in Fig. 3.5(b). In practice, because of the smaller spacing when coverage fraction is increased, C_0 also increases. This increase in effective total capacitance explains the observed red-shifting of the resonance frequency in MSRRs as the metal coverage fraction is increased. The equivalent circuit model for a MSR geometry consisting of two spirals is shown in Fig. 3.5(a). As the metal coverage fraction is increased, there are two competing effects taking place in this geometry: (i) as the number of turns increases, as depicted in Fig. 3.4(a), the equivalent capacitance first (at small number of turns) increases and then (at large number of turns) decreases. From this point of view, since indeed the number of turns is increased when the coverage fraction is increased, the resonance is expected to blue-shift for very large metal coverage fractions. On the other hand, (ii) as the coverage fraction is increased, C_0 increases due to a smaller spacing. From this point of view, the resonance is expected to red-shift. These two effects, (i) and (ii), are competing and both are important when increasing the coverage fraction. For small coverage fractions the same resonance-frequency evolution trend as in the MSRR is observed. However, for large coverage fractions (i) can become dominant, and the overall effect we observe might be a decrease in the equivalent circuit capacitance, and therefore a resonance frequency blue-shift.

However, when the metal coverage fraction is increased even further, (ii) can become dominant again and cause the resonance frequency to again red-shift; this leads to a very nonmonotonic characteristic at large coverage fractions.

It can be also observed (Fig. 3.4) that when the resonance red-shifts its strength diminishes, until eventually it becomes so weak that it disappears (blue, red, and sky-blue data points which correspond to 30%, 42%, and 49% metal coverage fractions, respectively). When the metal coverage fraction is further increased then a former higher-order resonance becomes the first resonance (e.g., purple data point, which corresponds to 64% metal coverage fraction), leading to a saw-tooth characteristic for resonance-frequency versus metal coverage fraction as observed in Fig. 3.4. The resonance strengths for metal coverage fractions above 80% become considerably weaker since the gaps between adjacent gold-stripes become much smaller than the width of the gold-stripes and thus the structure, effectively, is mostly covered with metal.

Shown in Fig. 3.6 are the plots of FoM_1 and FoM_2 versus metal coverage fraction for the two metamaterial geometries that were studied. When analyzing FoM_1, it is observed that in MSRs the smallest coverage fractions give the best tradeoffs. However, in MSRRs, decreasing the coverage fraction below 30% significantly decreases transmission and phase modulation due to a very weak interaction between rings. Therefore, it can be noticed that moderate coverage fractions (i.e., around 40%) give the best tradeoff.

When analyzing FoM_2, in MSRRs, it can be observed that large coverage fractions give the best tradeoff. This is a result of the monotonically increasing dependence of effective capacitance with coverage fraction in this geometry. However, in contrast, for

MSRs a completely different trend is observed when the metal coverage fraction is increased. There is an optimal coverage fraction, which occurs around 40%, that gives the best tradeoff. This is a result of the nonmonotonic dependence of equivalent capacitance with coverage fraction in this geometry.

When (overall) considering all the above described trends, it can be concluded that for both types of geometries the best tradeoff between FoM_1 and FoM_2 occurs in the region where coverage fraction is around 40%. *From this point of view, deeply-scaled metamaterials can indeed provide a better performance than traditional metamaterials in beam-shaping applications. However, counterintuitively, use of very highly packed structures can actually be not beneficial. There is an optimal metal coverage fraction, ~40%, which offers the best tradeoff. Interestingly, this optimal coverage fraction is the same for both types of metamaterial geometries, MSRRs and MSRs.*

3.5 Methods

Numerical simulations and structural parameters. In the analyzed metamaterials, gold was chosen as the material for the metallic layers, whereas Al_2O_3 was considered as the dielectric-in-between (see Fig. 3.1). These materials were set in top of a 2-μm thick polyimide layer, which has the role of a substrate; the thickness of the gold and Al_2O_3 layers was 1-μm. The metamaterials were numerically simulated employing high frequency structural simulator (HFSS). In these simulations graphene was taken as a finite-thickness material with 1-nm thickness, as discussed in Ref.[11, 18]

Table 3.1. Simulation results for the geometries depicted in Fig. 3.3

MSRR					MSR				
Metal coverage fraction	f_p (GHz)	T @ f_p	PM @ f_p	unit cell (μm)	Metal coverage fraction	f_p (GHz)	T @ f_p	PM @ f_p	unit cell (μm)
62%	220	60%	19°	(58)	64%	510	20%	33°	(52)
48%	290	34%	36°	(58)	42%	320	40%	42°	(54)
39%	350	28%	66°	(56)	37%	400	26%	67°	(52)
24%	440	17%	55°	(56)	30%	500	20%	108°	(54)

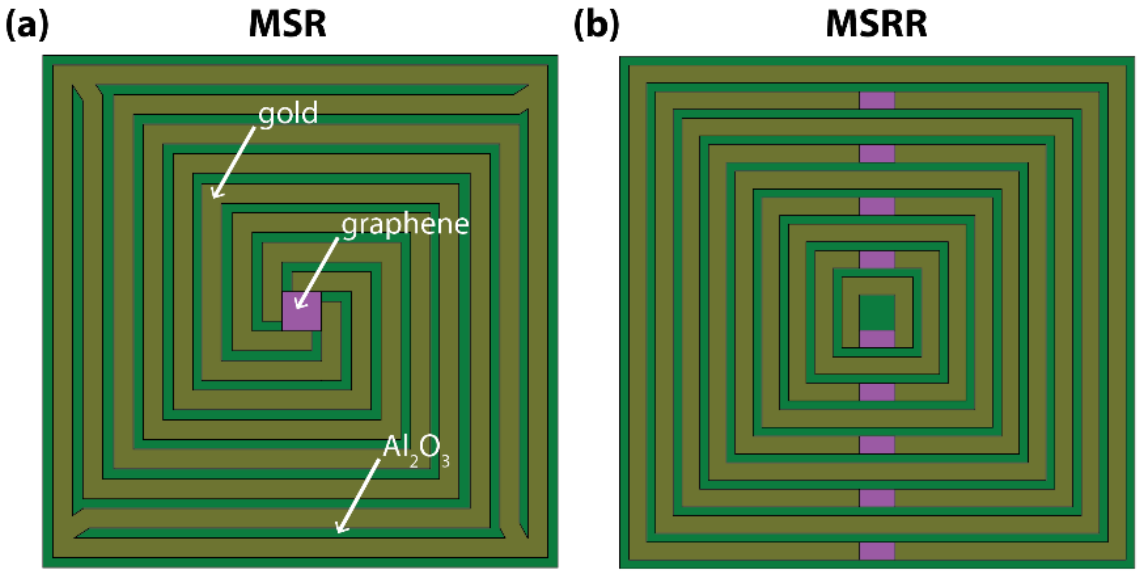

Figure 3.1. Sketches of the analyzed metacell geometries**.** (a) A multi spiral resonator (a), and (b) a multi split ring resonator.

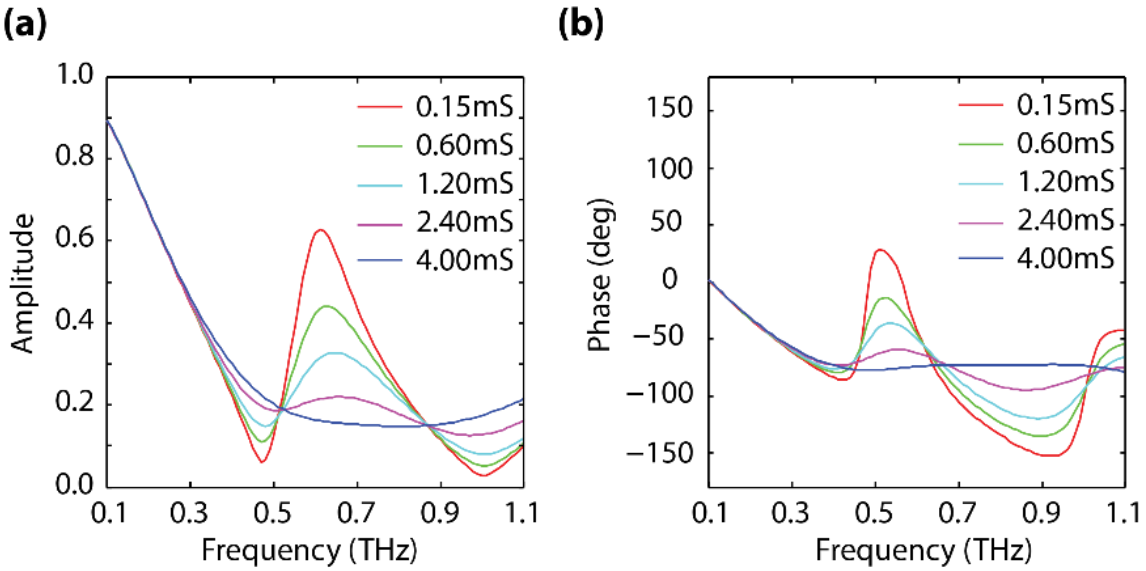

Figure 3.2. Characteristic response of one of the analyzed metamaterials. (a) Amplitude and (b) phase of the transmission as a function of frequency for different graphene conductivities —for a MSR with 30% metal coverage fraction. The conductivity of graphene is varied from 0.15mS to 4mS.

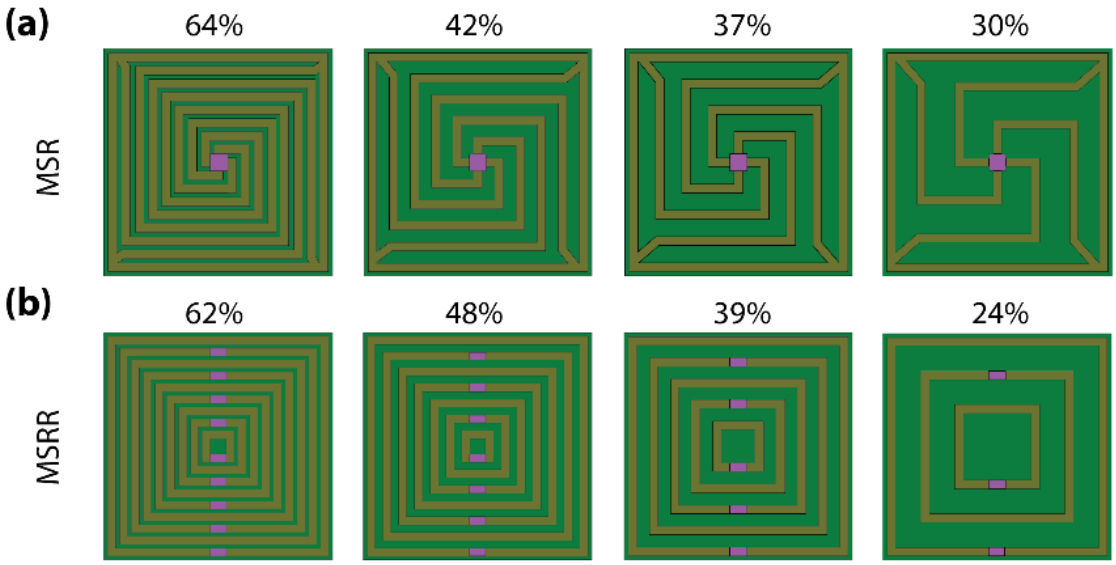

Figure 3.3. Sketch of the simulated metamaterial geometries. (a) Multi spiral resonators with metal coverage fraction 64%, 42%, 37% and 30%, and (b) multi split ring resonators with metal coverage fraction 62%, 48%, 39%, and 24%. The coverage fraction is defined as the ratio between the area covered by metal and the total area of a metacell.

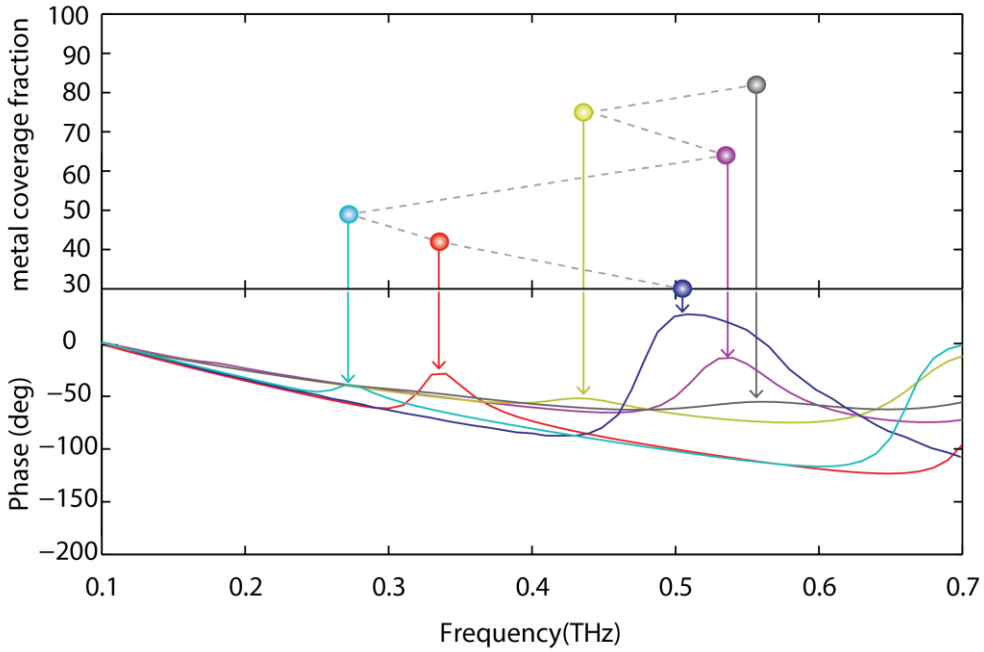

Figure 3.4. Phase of transmission for different metal coverage fraction in MSRs. The upper plot depicts the frequency at which maximum phase modulation takes place versus metal coverage fraction. The lower plot shows phase versus frequency for different metal coverage fractions.

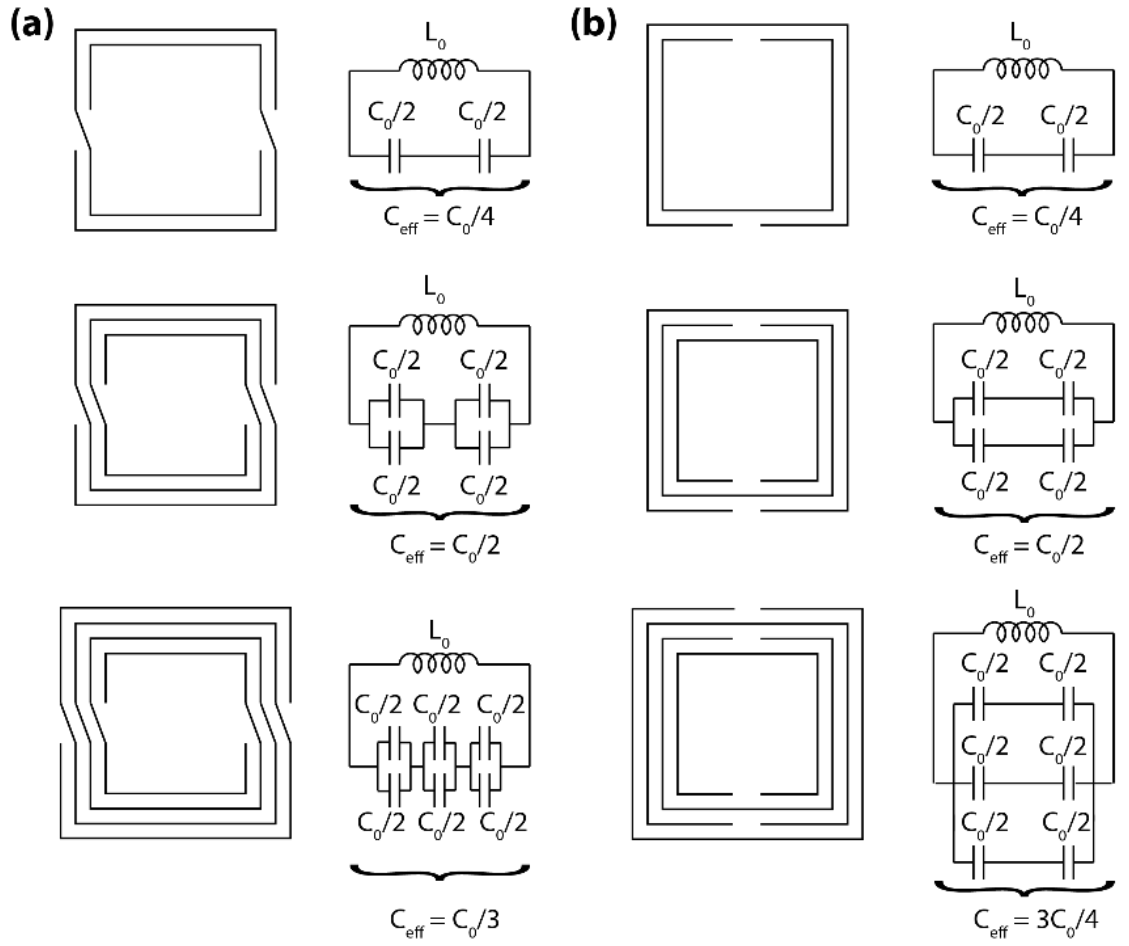

Figure 3.5. Equivalent circuit models. Different (a) MSR and (b) MSRR structures and their equivalent circuit model (following the discussion in Ref.[14]). For MSRs equivalent capacitance first (at small number of turns) increases and then (at large number of turns) decreases when the number of turns is increased, whereas for MSRRs the equivalent capacitance always increases. Here C_0 is the total capacitance between two adjacent rings, which is assumed to be the same for all the depicted structures.

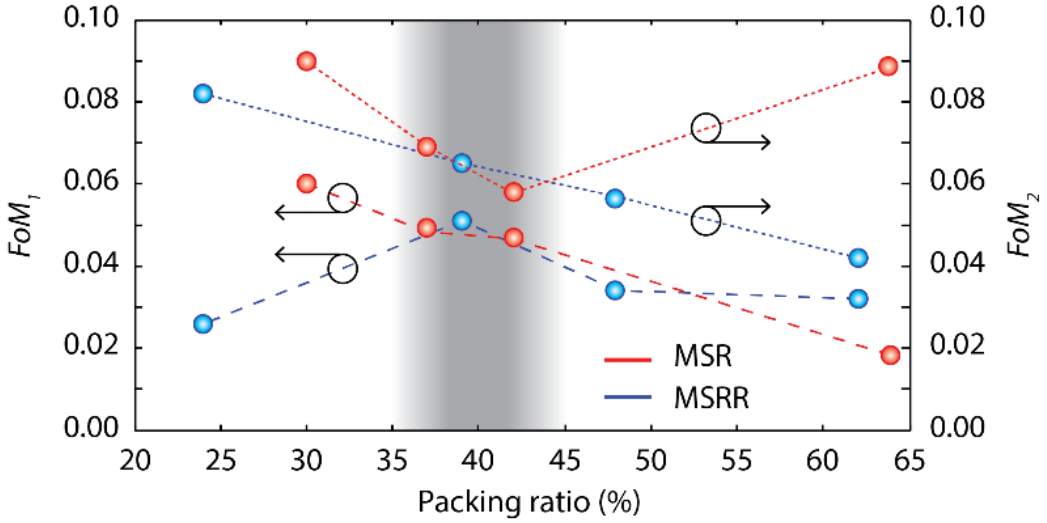

Figure 3.6. Figures of merit (*FoM*$_1$ and *FoM*$_2$) versus metal coverage fraction for both analyzed metamaterial geometries. In both cases, the best tradeoff occurs when the metal coverage fraction is around 40% (gray shaded region).

3.6 References

1. M. Tonouchi. Cutting-edge terahertz technology. *Nature Photon.* **1**, 97-105 (2007).

2. H. T. Chen, W. J. Padilla, J. M. Zide, A. C. Gossard, A. J. Taylor, and R. D. Averitt. Active terahertz metamaterial devices. *Nature* **444**, 597-600 (2006).

3. H. T. Chen, W. J. Padilla, M. J. Cich, A. K. Azad, R. D. Averitt, and A. J. Taylor. A metamaterial solid-state terahertz phase modulator. *Nature Photon.* **3**, 141–151 (2009).

4. P. Genevet, M. A. Kats, F. Aieta, J.-P. Tetienne, F. Capasso, and Z. Gaburro. Light propagation with phase discontinuities: generalized laws of reflection and refraction. *Science* **334**, 333–337 (2011).

5. M. Kafesaki, N. H. Shen, S. Tzortzakis, C. M. Soukoulis. Optically switchable and tunable terahertz metamaterials through photoconductivity. *Journal of Optics* **14**, 114008 (2012).

6. B. Sensale-Rodriguez, R. Yan, M. M. Kelly, T. Fang, K. Tahy, W. S. Hwang, D. Jena, L. Liu, and H. G. Xing. Broadband graphene terahertz modulators enabled by intraband transitions. *Nature Comm.* **3**, 780 (2012).

7. S. Arezoomandan, K. Yang, and B. Sensale-Rodriguez. Graphene-based electrically reconfigurable deep-subwavelength metamaterials for active control of THz light propagation. *Applied Physics A* 117, 423-426 (2014).

8. B. Sensale-Rodriguez, R. Yan, L. Liu, D. Jena, and H. G. Xing. Graphene for reconfigurable terahertz optoelectronics. *Proc. IEEE* **101**, 1705-1716 (2013).

9. S. H. Lee, M. Choi, T.-T. Kim, S. Lee, M. Liu, X. Yin, H. K. Choi, S. S. Lee, C.-G. Choi, S.-Y. Choi, X. Zhang, and B. Min. Switching terahertz waves with gate-controlled active graphene metamaterials. *Nature Mater.* **11**, 936-941 (2012).

10. M. Amin, M. Farhat, and H. Bagci. A dynamically reconfigurable Fano metamaterial through graphene tuning for switching and sensing applications. *Sci. Rep.* **3**, 2105 (2013).

11. R. Yan, B. Sensale-Rodriguez, L. Liu, D. Jena, and H. G. Xing. A new class of electrically tunable metamaterial terahertz modulators. *Opt. Express* **20**, 28664 (2012).

12. W. Gao, J. Shu, K. Reichel, D. V. Nickel, X. He, G. Shi, R. Vajtai, P. M. Ajayan, J. Kono, D. M. Mittleman, and Q. Xu. High-contrast terahertz wave modulation by gated graphene enhanced by extraordinary transmission through ring apertures. *Nano Lett.* **14**, 1242-1248 (2014).

13. E. Carrasco, M. Tamagnone, and J. Perruisseau-Carrier. Tunable graphene reflective cells for THz reflectarrays and generalized law of reflection. *Appl. Phys. Lett*. 102, 104103 (2013).

14. M. Liu, X. Yin, and X. Zhang. Double-layer graphene optical modulator. *Nano Lett.* **12**, 1482–1485 (2012).

15. L. Ju, B. Geng, J. Horng, C. Girit, M. Martin, Z. Hao, H. A. Bechtel, X. Liang, A. Zettl, Y. R. Shen, and F. Wang. Graphene plasmonics for tunable terahertz metamaterials. *Nat. Nanotechnol.* **6**, 630–634 (2011).

16. F. Bilotti, A. Toscano, and L. Vegni. Design of spiral and multiple split-ring resonators for the realization of miniaturized metamaterial samples. *IEEE Trans. Antennas. Propag.* 55, 2258–2267 (2007).

17. J.D. Baena, J. Bonache, M. Ferran, R. Marqués Sillero, F. Falcone, T. Lopetegi, M. Laso, J. Garcia-Garcia, I. Gil, M Portillo, and M. Sorolla. Equivalent-circuit models for split-ring resonators and complementary split-ring resonators coupled to planar transmission lines. *IEEE Trans. Microwave Theory and Techniques* **53**, 1451-1461 (2005).

18. K. Yang, S. Liu, S. Arezoomandan, A. Nahata, and B. Sensale-Rodriguez. Graphene-based tunable metamaterial terahertz filter. *Appl. Phys. Lett.* **105**, 093105 (2014).

3.7 Acknowledgement

The authors thank David Schurig and Ajay Nahata for useful discussions. The authors acknowledge the support from the NSF MRSEC program at the University of Utah under grant # DMR 1121252 and from the NSF CAREER award #1351389 (monitored by Dimitris Pavlidis).

AUTHOR CONTRIBUTIONS: S. A. and B. S-R. carried out the numerical simulations, analyzed the data, and contributed to the preparation of the manuscript.

AUTHOR INFORMATION: The authors declare no competing financial interests. Correspondence and request for materials should be addressed to Berardi Sensale-Rodriguez (berardi.sensale@utah.edu).

CHAPTER 4

GRAPHENE-BASED RECONFIGURABLE TERAHERTZ PLASMONICS AND METAMATERIALS

4.1 Abstract

This work discusses and compares two proposed practical approaches for realizing graphene-based reconfigurable terahertz metamaterials, namely, graphene-only plasmonic structures, and graphene/metal hybrid structures. From rigorous theoretical analysis, full-wave electromagnetic numerical simulations, as well as supporting experiments, several reconfigurable structures are analyzed and compared in terms of their: (i) Quality-factor, (ii) Extinction-ratio, (iii) Unit cell dimensions, and (iv) Resonance-frequency tunability-range. From this analysis it is observed that at terahertz frequencies, although typically possessing larger unit cell dimensions and being limited by a restricted resonance-frequency tunability-range, reconfigurable metamaterials based on graphene/metal hybrid structures can provide much larger quality-factors, extinction levels, and, when reconfigured, smaller extinction-level degradation than graphene-only plasmonic structures. As a result, when analyzed in the context of reconfigurable terahertz metamaterials, graphene might be attractive as a reconfigurable media providing tunability

The material provided in this chapter is available at: Carbon 112, pp.177-184 (2017).
Reprinted and adapted with permission from Elsevier.

to otherwise passive metallic structures rather than as a reconfigurable plasmonic material per-se.

4.2 Introduction

Over recent years, graphene has emerged as an attractive material for plasmonic and metamaterial applications [1-3]. Due to the possibility of efficiently tuning its electromagnetic properties via controlling its Fermi level [4-5], graphene is particularly appealing for applications demanding reconfiguration. Proposals and demonstrations of such reconfigurable structures have been reported in a wide range of frequencies, ranging from the microwave to the near-infrared [6-9]. In particular, at terahertz frequencies, multiple device structures have been proposed for realizing graphene-based reconfigurable metamaterials. In this regard, one of the main advantages of graphene resides on the possibility of integrating it onto arbitrary substrates, i.e., low-loss, low-*k* substrates. Graphene-based metamaterials can be loosely classified in two categories: (*a*) *graphene-only plasmonic structures*, and (*b*) *graphene/metal hybrid metamaterial structures*. Whereas in the first type of structures graphene is used as both the plasmonic media as well as the reconfigurable media, in the second type graphene behaves solely as the reconfigurable media, i.e., the electromagnetic response of the structure is completely set by the metal geometry. At terahertz frequencies reconfigurable *graphene-only plasmonic structures* were first shown by Ju *et al.* in 2011 employing arrays of graphene stripes gated by ion-gel [10]. Later work by Yan *et al.* experimentally demonstrated tunable properties in plasmonic structures consisting or graphene/insulator stacks arranged in disk arrays, where tunability was achieved by means of chemical doping [11]. More recently, Gomez-

Diaz *et al.* showed that self-biased graphene structures, i.e., capacitively coupled graphene layers, could be used for such applications [12]. Moreover, Liu *et al.*reported on electrically tunable graphene anti-dot array terahertz plasmonic crystals exhibiting multi-band resonances [13], and Zouaghi *et al,* on a simulation study, analyzed split-ring resonator arrays made completely of graphene, identifying the Drude scattering-time as an important parameter affecting the device performance [14]. Early work on reconfigurable *graphene/metal hybrid metamaterial structures* was driven by modulator [15] applications. In this context, Lee *et al.* showed that large-area unpatterned graphene could be employed as the tunable element in metamaterial switches consisting of graphene together with hexagonal and double split-ring-resonator metallic structures [16]. Later work by Yan *et al.* discussed the geometrical tradeoffs in such structures for modulator applications, finding that the graphene-to-metal separation is a key parameter, which controls the strength of light-matter interaction in graphene [17-18]. Experimental demonstrations of terahertz modulators based on structures consisting of active graphene and passive metallic split-ring resonators have been also reported by Valmorra *et al.* [19] and Degl'Inocenti *et al.* [20]. More recently, Gao *et al.* reported on graphene/metal hybrid structures using ring resonators with modulation depth approaching 50% and low loss [21], and Liu *et al.* [22] demonstrated a tunable modulator by coupling graphene plasmons to a metamaterial. In terms of theoretical analysis, Tamagnone *et al.* studied the fundamental limits of graphene-only and graphene/metal hybrid structures in terms of modulation performance via performing random simulations and exploring the geometrical parameter design space [23]. However, besides modulating the transmission amplitude at resonance, graphene/metal hybrid terahertz metamaterials have also been shown capable of actively

tuning its resonance-frequency (e.g., work by Yang *et al.* [24]). *In this context of recent advances in both graphene-only and graphene/metal hybrid structures, the aim of this paper is to rigorously discuss and compare both approaches for realizing graphene-based reconfigurable terahertz metamaterials*. In particular, structures enabling active tuning of their resonance-frequency will be discussed, which can find application as reconfigurable terahertz filters.

4.3 Discussion

In order to give physical insight into the properties of *graphene-only plasmonic structures,* let us consider an array of periodically patterned graphene disks, as studied in Ref. [11], and as depicted in Fig. 4.1(a). Such structure is chosen as a well-known example, one of the few that has an analytical solution, so to address the advantages and limitations of graphene-only plasmonic structures at terahertz frequencies. The physical origin and the properties of plasmons in such structures can be readily derived starting from the Drude terahertz conductivity of graphene. By employing classical electromagnetic analysis based on Maxwell-Garnett theory, and neglecting disk-to-disk interactions, the following average effective conductivity is obtained (see [25]):

$$\sigma_{av,eff} = F \frac{\sigma_{graphene}(\omega)}{1+\frac{\pi\sigma_{graphene}(\omega)}{2d\varepsilon_0(1+\varepsilon_S)i\omega}} \ , \tag{4.1}$$

where F is the filling factor, i.e., fraction of the area covered by the disks, d is the disk radius, ε_0 is the vacuum permittivity, ε_s is the substrate relative permittivity, and $\omega = 2\pi f$ is the angular frequency. Moreover:

$$\sigma_{graphene}(\omega) = \frac{\sigma_{DC}}{1+i\omega\tau} \ , \tag{4.2}$$

is the terahertz sheet conductivity of graphene, where σ_{DC} represents its DC sheet conductivity and τ its electron momentum relaxation time. In the terahertz regime the conductivity of graphene can be modeled by a Drude model [26-29] since the contribution arising from interband transitions is negligible at this frequency range. At normal incidence, the transmission (T) through such structure —normalized to that of the substrate (T_0)— is given by [11]:

$$\frac{T}{T_0} = \frac{1}{\left|1+\frac{Z_0\sigma_{av,eff}(\omega)}{1+\sqrt{\varepsilon_S}}\right|^2} \ , \tag{4.3}$$

where $Z_0 = 377\ \Omega$ is the vacuum impedance, and the substrate was assumed to be optically thick. By substituting Eqn. (4.1) and (4.2) into Eqn. (4.3), the following expressions can be derived:

$$\omega_p = \sqrt{\frac{\pi\sigma_{DC}}{2d\varepsilon_0(1+\varepsilon_S)\tau}} \ , \tag{4.4}$$

$$E = 1 - \frac{T}{T_0}\Big|_{@\omega_p} = 1 - \frac{1}{\left|1+\frac{Z_0 F\sigma_{DC}}{1+\sqrt{\varepsilon_S}}\right|^2} \ , \tag{4.5}$$

$$Q = \omega_p\tau\sqrt{1-E} \ , \tag{4.6}$$

where ω_p, and Q represent the frequency and quality factor of the plasmonic resonance, respectively, and E represents the extinction evaluated at the plasmonic resonance frequency. The detailed derivation of these equations is presented in the *Supplementary Information*. In this regard it is worth mentioning that Eqns. (4.5) and (4.6) are general enough to hold for any convex geometry, e.g., squares, rectangles, triangles, etc. From Eqn. (6) it results the following fundamental upper bound for the quality factor: $Q < \omega_p\tau$. From this perspective, *this simple example demonstrates that quality factors above unity are not possible in structures designed to exhibit resonances at frequencies such that* $\omega_p <$

$1/\tau$. In this context, due to typical wavelengths practically employed in terahertz technology being on the order of > 100 μm (where 100 μm corresponds to 3 THz) and therefore terahertz beam spot sizes being > 100 μm^2, single-layer graphene samples with area > 100 μm x 100 μm are usually required for terahertz applications. From this point of view, large-area chemical vapor deposition (CVD) grown graphene films are normally employed for terahertz plasmonic and metamaterial applications. In this regard, it is worth noticing that the electron momentum relaxation time in such samples is typically on the order of < 0.1 ps (e.g., Ref. [30], where τ < 0.1 ps was observed even in CVD graphene samples grown on single-crystal copper), and thus, in practice, $Q << 1$ in structures exhibiting plasmonic resonances up to 1.6 THz.

The DC sheet conductivity of graphene can be expressed as:

$$\sigma_{DC} = \sqrt{n_{2D}}\tau e^2 v_F/\sqrt{\pi}\hbar \,, \tag{4.7}$$

where v_F is the Fermi velocity in graphene ($v_F \approx 10^6 m/s$), n_{2D} is the graphene electron sheet density, $\hbar$ is the reduced Planck constant, and e is the electron charge. It is worth mentioning that the charge density dependence in Eqn. (4.7) is different from what is seen in typical (parabolic-band) semiconductor materials, where a n_{2D} dependence rather than $\sqrt{n_{2D}}$ is observed. In the limit when $E \to 1$, which is desired in terms of practical applications, it results:

$$\omega_p^2 = \frac{\sqrt{\pi}e^2 v_F}{2\hbar\varepsilon_0(1+\varepsilon_s)}\frac{\sqrt{n_{2D}}}{d} \,, \tag{4.8}$$

$$Q = \frac{1+\sqrt{\varepsilon_s}}{Z_0 F}\frac{\pi^{3/4}\sqrt{\hbar}}{e\sqrt{2\varepsilon_0(1+\varepsilon_s)v_F}}\frac{1}{d n_{2D}^{1/4}} \,, \tag{4.9}$$

where Eqn. (4.8) has been directly derived by substituting Eqn. (4.7) into Eqn. (4.4), and Eqn. (4.9) has been derived from Eqn. (4.6) via a Taylor expansion. From Eqns. (4.8) and

(4.9) it is observed that when $E \to 1$, the relaxation time, which is related to the graphene quality, affects neither ω_p nor Q. It is worth noticing that for the extinction-ratio to approach unity, large filling-fraction, approaching the hexagonal packing density of $F = (\pi\sqrt{3})/6 \approx 0.91$ is desired, in addition to: small substrate refractive index, and large τ, as well as large n_{2D} in accordance with Eqns. (4.5) and (4.7). However, as can be noticed in Eqn. (8), terahertz plasmonic resonances require small n_{2D} in addition to large geometric dimensions, i.e., large d. By inspecting Eqn. (4.9) it is observed that small n_{2D} is also associated with large Q, yet, since Q is inversely proportional on d, small dimensions are preferred from this point of view. In general, there are multiple tradeoffs between these parameters. Shown in Fig. 4.1(b) are the contour plots of ω_p and Q versus d and n_{2D}, in accordance with Eqns. (4.8) and (4.9), and assuming $\varepsilon_s = 1$ (so to maximize E). The curves for which $\omega_p = 0.5$ THz and $\omega_p = 1$ THz are depicted in orange-colored and red-colored solid-traces, respectively. Contour plots for Q are filled in blue color-scale (light-blue representing $Q < 1$ and dark-blue representing $Q > 1$). It is observed that $Q > 1$ and $\omega_p = 1$ THz requires $n_{2D} < \sim 7\text{x}10^{12}$ cm^{-2}, whereas for $Q > 1$ and $\omega_p = 0.5$ THz, $n_{2D} < \sim 2\text{x}10^{12}$ cm^{-2} is required.

In order to describe the most general behavior of the structure we lifted the assumption of $E \to 1$. Shown in the *Supplementary Information*, Fig. A.1, are the general contour plots for Q, E, and ω_p versus n_{2D} and d for different values of ε_s and τ, in accordance with Eqns. (4.4)-(4.7). It is observed that for a fixed disk geometry (i.e., constant d): (*i*) for $\tau < 1$ ps, as n_{2D} is increased Q increases; (*ii*) for $\tau \sim 1$ ps, Q depends very slightly on n_{2D} (when n_{2D} is varied), which is particularly evident on low permittivity environments (i.e., when ε_s approaches unity); (*iii*) for $\tau > 1$ ps, as n_{2D} is increased Q decreases. Case (*iii*)

typically corresponds to a situation where $E \to 1$, thus Q follows the behavior described by Eqn. (4.9) and depicted in Fig. 4.1(b). Moreover, it is also observed that for a given ω_p design-target, i.e., when looking at the curves representing constant ω_p in Fig. A.1, if $\tau \sim$ 0.1 - 0.2 ps, Q cannot be significantly altered by changing d and n_{2D}. In these cases it is particularly difficult to achieve $Q > 1$. On the other hand, when $\tau > 1$ ps, as both n_{2D} and d are simultaneously varied (so that ω_p is fixed), it is observed that E increases as the values of these parameters are increased, but at the expenses of a lower Q (in agreement with the discussion in Fig. 4.1(b)). In synthesis, *at typical frequencies of interest of terahertz technology*, i.e., f < 2 THz, *it is extremely difficult to attain simultaneously high-Q* (i.e., $Q > 1$) *and large extinction* (i.e., $E > 0.8$), *unless employing graphene with very large* τ (i.e., τ exceeding 1 ps), *which from a practical perspective is extremely challenging in large-area CVD-grown graphene*; *the lower the* ω_p *design-target the more pronounced this tradeoff.*

On the other hand, *graphene/metal hybrid metamaterials* can also provide for active tuning of resonance properties [24]. Depicted in Fig. 4.2(a) is the sketch of one such a structure composed of metallic split-ring resonators (SRRs) in conjunction with strategically-placed active graphene layers. The reason why tuning of the resonance-frequency is observed when altering the graphene conductivity, rather than tuning of the transmission amplitude at resonance, is a result of the strategic placement of the patterned graphene film, which is located solely inside the SRR gap. Figure 4.2(b) shows an equivalent circuit model for the structure. In this model, which is validated in the *Supplementary Information*, graphene is modelled as an impedance of value $Z_g = R_g + i\omega L_g$, where R_g and L_g represent its associated resistance and inductance, respectively. Moreover,

the metallic pattern is represented by the series connection of a resistor (R), an inductor (L), and two capacitors (C, and C_{gap}) [31-34]. In this regard, it is worth noticing that L represents the self-inductance of the metal loop and R the metal losses. Furthermore, whereas the capacitor C results from the separation between adjacent unit cells [34], the capacitor C_{gap} has its geometric origin on the gaps inserted along the metal loops (see e.g., [35]). When the graphene conductivity is altered, therefore, R_g is varied, the structure switches between the two-resonant states as depicted on the center and right panels of Fig. 4.2(b), corresponding to $R_g = 0$ and $R_g \rightarrow \infty$. These two resonant-states are uniquely set by the geometry of the metallic pattern. In this case the graphene quality (τ) has a negligible role in the overall response of the structure.

4.4 Results

In order to provide a comprehensive study, *we prepared two sets of samples, consisting of: (Sample Set #1) graphene-only plasmonic structures made of arrays of periodically patterned graphene-disks which are set on a hexagonal lattice.* Different from previous works (e.g., Ref. [11]), our plasmonic structures were designed so to exhibit resonances at $f < 1$ THz. Therefore, large disk radii are employed (radius > 10 μm). *(Sample Set #2) graphene/metal hybrid metamaterial structures consisting of split-ring resonator arrays, in which graphene is strategically-placed inside the SRR gap* (as proposed in Ref. [24]). Moreover, a third geometry is also analyzed, but solely via numerical simulations: *(Sample Set #3) high-Q metal/graphene hybrid metamaterials; where graphene is integrated as an active element in the high-Q metallic metamaterial geometry described in Ref.* [36], *which consists of concentric ring-resonators with*

interdigitated-fingers (ICRs). The fabricated samples (*Sample Set #1* and *Sample Set #2*) are schematically depicted in Fig. 4.3(a). Each sample contains a control region from where the graphene properties are directly extracted by means of terahertz spectroscopy and FTIR measurements. Sketches of the unit cells for all the analyzed structures, together with details of their relevant geometric dimensions, are pictured in Fig. 4.3(b). For details about the experimental methods, sample fabrication, and full-wave electromagnetic numerical simulation procedures please refer to the *Methods Section*.

At this end we proceed to study the *graphene-only plasmonic structures* (*sample Set #1*). These samples consist of disk-patterned single layer CVD graphene on top of a 4 μm thick polyimide (PI) substrate. The graphene conductivity was altered by means of chemical doping (see *Methods Section*). Disks were arranged on a hexagonal lattice as depicted in Fig. 4.1(a); the disk radius (d) was set to d = 23 μm, whereas the separation between centers of adjacent disks was set to 50 μm. From terahertz and FTIR transmittance measurements through the control region of the sample after successive cycles of chemical doping, sheet conductivity / relaxation-time values of: (*i*) 1.4 mS / 50.5 fs, (*ii*) 1.9 mS / 63.4 fs, and (*iii*) 2.4 mS / 57.4 fs were extracted. Full-wave electromagnetic simulations were performed for the disk array employing these extracted graphene parameters. The simulated extinction is depicted in Fig. 4.4(a); cases (*i*), (*ii*), and (*iii*) are depicted in red, green, and blue-colored curves, respectively. A decrease in E is observed as the graphene conductivity, thus ω_p, is decreased, in accordance with Eqn. (4.5). Quality factors, Q, of 0.16, 0.23, and 0.24 are observed for cases (*i*), (*ii*), and (*iii*), respectively, as depicted in Fig. 4.4(b). In all cases $Q << 1$ in accordance with the previous theoretical discussion. Shown in Fig. 4.4(c) is the measured extinction through the fabricated samples after each

cycle of chemical doping together with an optical image (inset in the figure) depicting a section of the array; a good qualitatively agreement is observed between measurements (Fig. 4.4(c)) and the full-wave electromagnetic simulations (Fig. 4.4(b)).

We also studied samples consisting of *graphene/metal hybrid structures (Sample Set #2).* These samples consist of SRRs, whose geometry was optimized following the discussion in Ref. [24], but for a target resonance-frequency swing between 0.4 THz (low-frequency resonant-state) and 0.7 THz (high-frequency resonant-state). These structures consist of a 110 nm thick metallic metamaterial structure laying on top of a 4 μm thick PI substrate, and contain wet-transferred single-layer CVD graphene whose conductivity is reconfigured by means of stacking different number of layers following the procedure in Ref. [18] (see *Methods Section*). Shown in Fig. 4.5(a) is an optical microscopy image of one of the fabricated samples. The inner and outer radii (R_{in} and R_{out}) were set to 110 and 120 μm, respectively, the gap width (g) was set to g = 2 μm, and the unit cell (separation between centers of adjacent rings) was set to 300 μm. The measured and simulated (HFSS) extinctions through these structures are depicted in Figs. 4.5(b) and 4.5(c), respectively. The resonance-frequency red-shifts as the overall graphene conductivity is increased, i.e., when the number of transferred graphene layers is increased from zero to five as shown by the blue (zero layers), red (one layer), yellow (two layers), violet (three layers), and green curves (five layers), respectively. The observed resonance red-shift in structures with three and five graphene layers is larger than that in structures containing one and two layers, which is owed to the transmission through the structure being a nonlinear function of the graphene conductivity. In this regard, it is worth noticing that it exists a particular conductivity level that maximizes the sensitivity of extinction to graphene conductivity.

Overall the resonance shifts from 0.65 to 0.45 THz. The frequency-tunability range of this reconfigurable structure is set by the geometry of the metallic SRRs; as the graphene conductivity is enhanced, the resonance approaches that of the complete rings (black colored curves). This can be physically understood on basis of the equivalent circuit model depicted in Fig. 4.2(b). A fit of the data to the equivalent circuit model together with a discussion on the effect of momentum relaxation time on the electromagnetic response of the structure, which is found to be negligible, is discussed in the *Supplementary Information* (Figs. A.2, A.3, and A.4). Figure 4.5(d) shows the quality-factor (extracted from the full-wave simulation data plotted in Fig. 4.5(c)) as a function of graphene conductivity; the quality factor shows a nonmonotonic dependence on conductivity. Q ranging between 2.2 and 1.0 is observed when the graphene sheet conductivity is varied from σ_{DC} = 0.15 to 2.4 mS. In this regard it is worth mentioning that the quality factor at the limit resonant-states are 3.0 (no-graphene) and 1.5 (complete ring), respectively.

Finally, we analyzed structures consisting of concentric ring resonators with interdigitated fingers (ICRs) (*Sample Set #3*). As discussed by Jensen *et al.* [36], such structures can attain even larger quality factors at terahertz frequencies. In order to provide for reconfiguration, the structure is modified by inserting graphene on a section of the gap between the rings and the interdigitated fingers as depicted in Fig. 4.3(b). A 4 μm thick PI substrate is assumed. The inner and outer radius (R_{in} and R_{out}) were set to 35 and 90 μm, respectively; the width of each ring (l) was set to l = 20 μm, thus leading to a distance between rings ($d + a$) of 15 μm. The finger length (w) was set to w = 2 μm, whereas d was set to 12 μm. The unit cell was set to 300 μm. The length of the gap where graphene is placed (g) is varied in order to optimize the sensitivity of the structure to a typical graphene

sheet conductivity swing; a swing between 0.15 mS and 2.4 mS was assumed in accordance with previous discussions. Depicted in Figs. 4.6(a-c) is the simulated (HFSS) extinction when the graphene sheet conductivity is varied. Three cases are analyzed, corresponding to g = 0.25 um, g = 0.75 um, and g = 1.25 um, which are depicted in Figs. 4.6(a), 4.6(b), and 4.6(c), respectively. In a similar way to what has been shown in *Sample Set #2*, as the graphene conductivity is increased, the resonance red-shifts; the structure again shifts between two resonant-states, which are uniquely set by the metal geometry. For smaller gaps (Fig. 4.6(a)), the resonances tend to cluster near the low-frequency resonant-state, whereas for large gaps (Fig. 4.6(c)), the resonances tend to cluster near the high-frequency state. An optimal gap-length (g ~ 0.5 μm) exists. Depicted in Fig. 4.6(d) is the resonance-frequency versus graphene conductivity for the three analyzed gap-lengths showing the latter effect; moreover, it can be observed that for a fixed graphene conductivity as the gap-length is increased the resonance-frequency increases. This can be understood as a result of the associated gap-capacitance (C_{gap}) decreasing as the gap-length is increased. Therefore, as the gap-length is increased the overall capacitance associated with the structure decreases, which results in a resonance blue-shift. When the graphene conductivity is varied, the quality factor ranges between 3 and 5 (see Fig. 4.6(e)); this is ~ 3X larger than what we observed in *Sample Set #2* and > 10X larger than what was observed in Sample Set #1. However, the resonance-frequency tunability range attainable in *Sample Set #3* is just 40 GHz (~ 0.47 to ~0.51 THz), which is much smaller than what is achievable in *Sample Set #1* (unconstrained frequency tunability) and *Sample Set #2* (~200 GHz).

4.5 Methods

The fabrication procedure for all samples is analogous to the process we reported in Ref. [18]. It starts with coating a glass substrate with polyimide (PI-2600) and curing it by gradually increasing the temperature to 300°C. Fabrication for *Sample Set #1* is followed by transfer of a graphene layer. Single-layer graphene films (monolayer percentage >95%) grown by means of CVD on a copper foil were obtained from a commercial vendor (Bluestone). These films are transferred to the samples using PMMA and wet etch methods [37]; in this process, graphene grown on copper foil is first covered by means of spin-coating PMMA (950-PMMA-C2). Then, the graphene on the back side of the foil, i.e., the side not covered by PMMA, is etched employing reactive ion etching (RIE). Subsequently, the copper foil is etched in copper etchant (COPPER ETCHANT APS-100), and the suspended graphene-on-PMMA layer is moved to DI water. Finally, transfer into the desired substrate is carried out in the DI water. Depicted in the *Supplementary Information* (Fig. A.5) are typical Raman spectra for our graphene films showing characteristic features of single layer graphene. The transferred films are then patterned by means of photolithography and RIE steps. Finally, the fabricated sample is peeled off from the glass substrate, forming a flexible, free-standing, ultrathin film. In *Sample Set #2*, after the PI film is coated and cured, we proceed to define the metal pattern. For this purpose, photolithography (Shipley 1813 photoresist process) and metal deposition processes are employed. Ti/Au with thickness of 10nm/100nm are deposited to define the metallic structure. After this, one to five layers of graphene are transferred. Finally, we perform lithography and RIE steps so that graphene remains just in the gap region.

In *Sample Set#1*, the graphene conductivity is varied by means of chemical doping.

In this regard, nitric acid (HNO_3) is well known to be a *p*-type dopant for graphitic materials such as carbon nanotubes and graphene [37-38]. Chemical doping was realized by immersing a single-layer graphene in a HNO_3 solution, followed by a dry and baking step at 85℃, as we previously reported in Ref. [18]. In these samples, no change in the doping level was observed over time. In *Sample Set #2*, we observed that the metallic film defining the metamaterial peels-off when immersing the sample in nitric acid solution. This is the reason why the conductivity in *Sample Set #2* was varied by means of stacking graphene layers rather than by means of chemical doping.

It is also important to mention that in order t*o account for the process induced variations on the graphene properties in order to therefore improve the accuracy when comparing our experimental results with simulations and theory, each fabricated sample is composed of two regions: (i) a test region, consisting of the structure under test (left part of the sample), and (ii) a control region, consisting of unpatterned-graphene (right part of the sample),* as shown in Fig. 4.3(a). The graphene properties are directly extracted by means of terahertz spectroscopy and FTIR measurements over the control region of each sample. The optical conductivity of graphene is determined by fitting the transmission spectra through the control region to an analytical model. In this regard, a Drude model is employed to represent the frequency-dependent graphene optical conductivity, as dictated by Eqn. (4.3). The experimentally extracted relaxation time (τ) and DC sheet conductivity (σ_{DC}) of graphene were then used to validate our experimental results with simulations. A discussion on the fitting and typical results obtained from this procedure is depicted in the *Supplementary Information* (Fig. A.6) showing an excellent fit to a Drude model.

Full-wave 3-D electromagnetic numerical simulations were conducted employing

High Frequency Structure Simulator (ANSYS HFSS) by considering graphene as a zero-thickness graphitic layer (layered impedance) with sheet conductivity set to the experimentally determined values. In this regard it is worth mentioning that results using a finite thickness model for graphene (e.g., [17]) match those obtained employing the layered impedance model as discussed in our early work (Ref. [18]). Depicted in the *Supplementary Information* (Fig. A.7) is a detail of some of the simulated geometries as set in HFSS. It can be observed that the simulated geometries represent exactly the fabricated ones and fully take into account the effect of the substrate. In this regard, a relative permittivity of 3.24 was assumed for polyimide [39-40]. Periodic boundary conditions were set around the unit cells so to represent an infinite array and to account for interactions between adjacent elements.

For terahertz characterization, a CW THz spectrometer (Toptica Photonics) was employed, which is based on InGaAs photo-mixers at 1550 nm for both generation and coherent detection [41]. A sketch of the system, which can cover a spectral range from 0.1 to 2 THz, is depicted in the *Supplementary Information* (Fig. A.8). A FTIR system (Bruker IFS-88) was employed for finding the spectra at shorter wavelengths (i.e., above 4 THz) and thus extract the momentum relaxation time through the control regions of the samples by means of fitting the measured transmittance to an analytical model, as previously discussed. All the reported terahertz data are normalized to a reference polyimide substrate.

4.6 Conclusions

In this work we analyzed and compared the terahertz response of graphene-only plasmonic and graphene-metal hybrid metamaterial structures. In these structures, when the graphene conductivity is altered, e.g., by means of changing its Fermi level, the resonance is shifted. From theory, simulations, as well as supporting experiments, we find that graphene-metal hybrid structures can offer: (*a*) stronger resonances, (*b*) larger quality factors, and (*c*) less sensitivity to the graphene quality (given by momentum relaxation time) than the graphene-only plasmonic structures. However this occurs at the expense of a limited resonance frequency-shift and increased unit cell footprint. Overall, we conclude that at terahertz frequencies graphene might be more attractive as a reconfigurable media providing tunability to otherwise passive, metallic structures rather than as a reconfigurable plasmonic material by itself.

4.7 Acknowledgement

The authors acknowledge the support from the NSF MRSEC program at the University of Utah under grant no. DMR 1121252. B.S.-R. and H.C.Q. also acknowledge support from the NSF CAREER award no. 1351389 and the NSF award ECCS #1407959. Students N.R. and C.N. acknowledge support through the University of Utah MRSEC REU program.

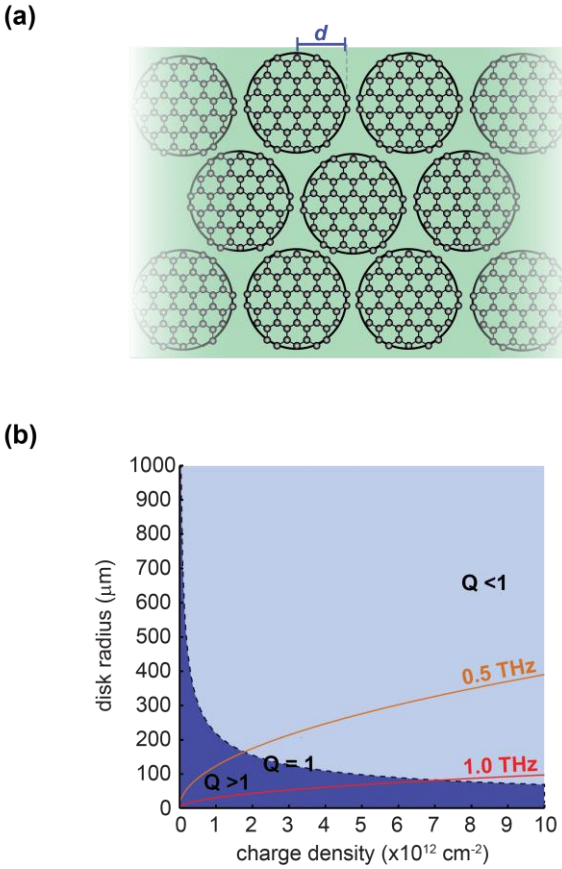

Fig. 4.1. (a) Sketch of a plasmonic structure consisting of an array of graphene disks. **(b)** Contour plots of quality factor (*Q*) and resonance-frequencies as a function of charge density and disk radius (in the limit when assuming the extinction to approach unity).

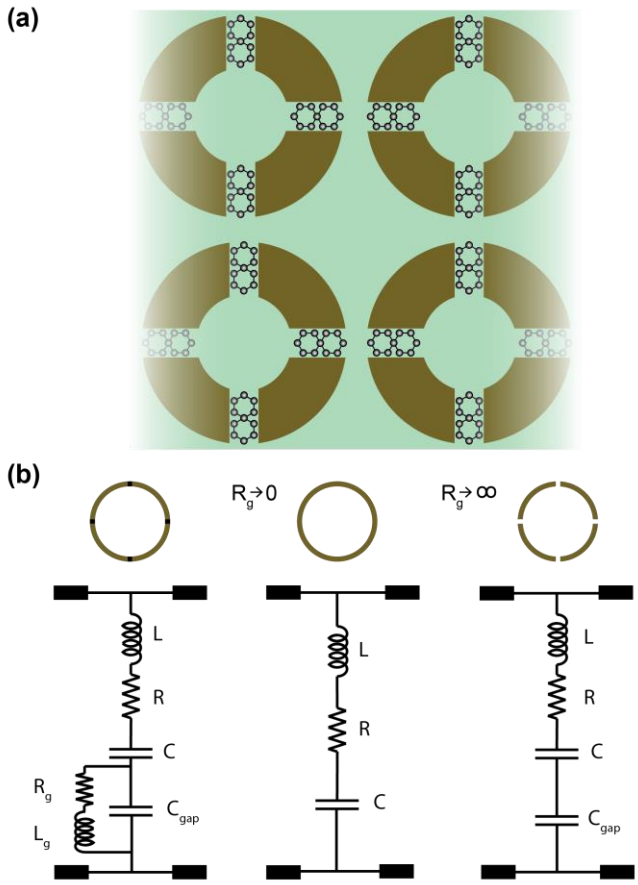

Fig. 4.2. (a) Sketch of a graphene/metal hybrid metamaterial structure consisting of SRRs with graphene placed inside the gaps. **(b)** Equivalent circuit model for the structure. Graphene is modelled as an impedance of value $Z_g = R_g + i\omega L_g$.

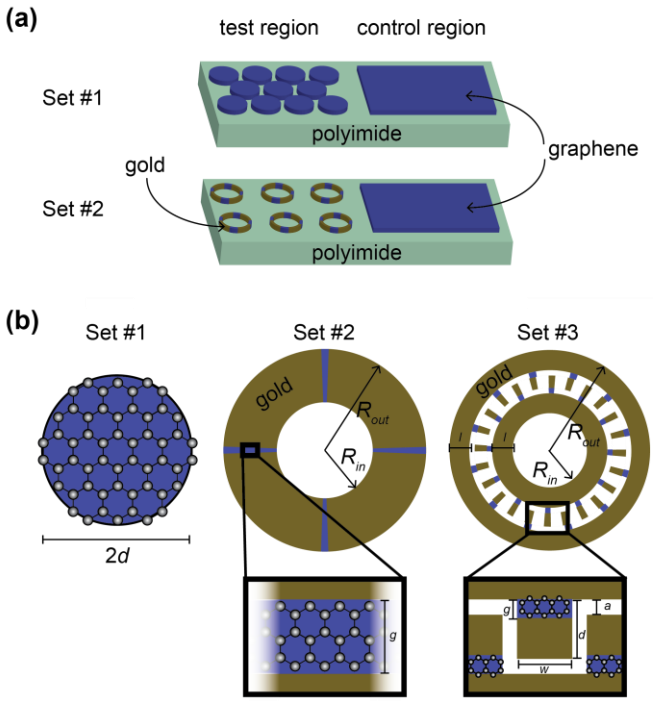

Fig. 4.3. (a) Schematic of the fabricated samples (*Sample Set #1* and *Sample Set #2*). The right half of the samples (control region), which contains unpatterned graphene in top of polyimide, is used to monitor the sheet conductivity of graphene. **(b)** Unit cell detail and parameter definition for all the analyzed structures.

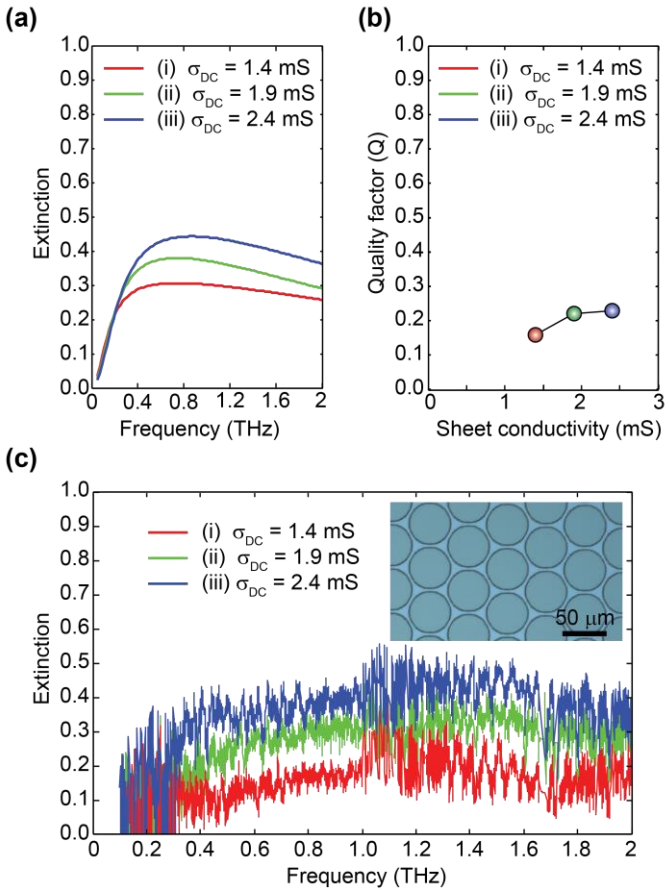

Fig. 4.4. (a) Simulated extinction versus frequency for Sample Set #1. **(b)** Quality factor as a function of sheet conductivity (extracted from the data in (a)). **(c)** Measured extinction versus frequency for Sample Set #1. The inset depicts an optical micrograph detail of a fabricated sample before removing the photoresist.

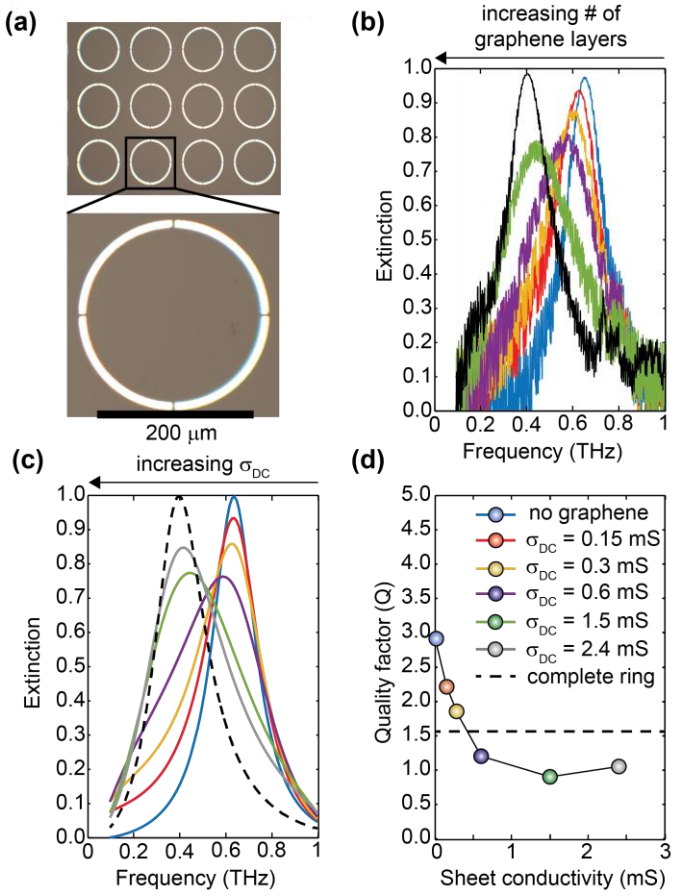

Fig. 4.5. (a) Optical image showing a detail of the graphene/metal hybrid metamaterial structure consisting of SRRs (*Sample Set #2*). **(b)** Measured extinction versus frequency for the sample depicted in (a) when varying the number of stacked graphene layers in the gap. **(c)** Simulated extinction versus frequency. **(d)** Extracted quality factor as a function of graphene sheet conductivity.

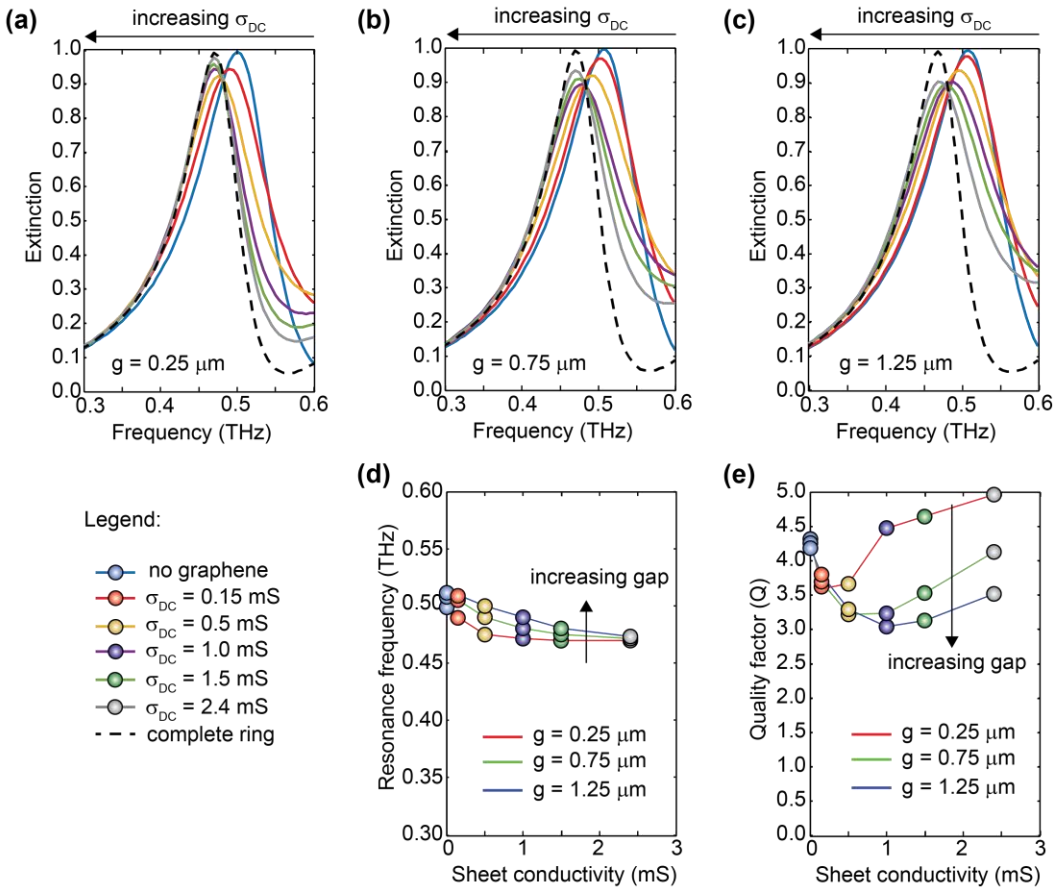

Fig. 4.6. (a)-(c) Simulated extinction versus frequency for *Sample Set #3*. Cases (a), (b), and (c) correspond to g = 0.25, 0,75, and 1.25 μm, respectively. **(d)** Extracted resonance-frequency versus sheet conductivity for the cases depicted in (a)-(c). **(e)** Extracted quality factor versus sheet conductivity for the cases depicted in (a)-(c).

4.8 References

[1] Koppens FHL, Chang DE, García de Abajo FJ. Graphene Plasmonics: A platform for strong light–matter interactions. Nano Letters. 2011;11(8):3370-7.

[2] Grigorenko AN, Polini M, Novoselov KS. Graphene plasmonics. Nat Photon. 2012;6(11):749-58.

[3] Low T, Avouris P. Graphene plasmonics for terahertz to mid-infrared applications. ACS Nano. 2014;8(2):1086-101.

[4] Li ZQ, Henriksen EA, Jiang Z, Hao Z, Martin MC, Kim P, et al. Dirac charge dynamics in graphene by infrared spectroscopy. Nat Phys. 2008;4(7):532-5.

[5] Wang F, Zhang Y, Tian C, Girit C, Zettl A, Crommie M, et al. Gate-variable optical transitions in graphene. Science. 2008;320(5873):206-9.

[6] Chen J, Badioli M, Alonso-Gonzalez P, Thongrattanasiri S, Huth F, Osmond J, et al. Optical nano-imaging of gate-tunable graphene plasmons. Nature. 2012;487(7405):77-81.

[7] Fei Z, Rodin AS, Andreev GO, Bao W, McLeod AS, Wagner M, et al. Gate-tuning of graphene plasmons revealed by infrared nano-imaging. Nature. 2012;487(7405):82-5.

[8] Sensale-Rodriguez B, Yan R, Liu L, Jena D, Xing HG. Graphene for reconfigurable terahertz optoelectronics. Proceedings of the IEEE. 2013;101(7):1705-16.

[9] Balci O, Polat EO, Kakenov N, Kocabas C. Graphene-enabled electrically switchable radar-absorbing surfaces. Nat Commun. 2015;6.

[10] Ju L, Geng B, Horng J, Girit C, Martin M, Hao Z, et al. Graphene plasmonics for tunable terahertz metamaterials. Nat Nano. 2011;6(10):630-4.

[11] Yan H, Li X, Chandra B, Tulevski G, Wu Y, Freitag M, et al. Tunable infrared plasmonic devices using graphene/insulator stacks. Nat Nano. 2012;7(5):330-4.

[12] Gomez-Diaz JS, Moldovan C, Capdevila S, Romeu J, Bernard LS, Magrez A, et al. Self-biased reconfigurable graphene stacks for terahertz plasmonics. Nat Commun. 2015;6.

[13] Liu PQ, Valmorra F, Maissen C, Faist J. Electrically tunable graphene anti-dot array terahertz plasmonic crystals exhibiting multi-band resonances. Optica. 2015;2(2):135-40.

[14] Zouaghi W, Voß D, Gorath M, Nicoloso N, Roskos HG. How good would the

conductivity of graphene have to be to make single-layer-graphene metamaterials for terahertz frequencies feasible? Carbon. 2015;94:301-8.

[15] Sensale-Rodriguez B, Yan R, Kelly MM, Fang T, Tahy K, Hwang WS, et al. Broadband graphene terahertz modulators enabled by intraband transitions. Nat Commun. 2012;3:780.

[16] Lee SH, Choi M, Kim T-T, Lee S, Liu M, Yin X, et al. Switching terahertz waves with gate-controlled active graphene metamaterials. Nat Mater. 2012;11(11):936-41.

[17] Yan R, Sensale-Rodriguez B, Liu L, Jena D, Xing HG. A new class of electrically tunable metamaterial terahertz modulators. Opt Express. 2012;20(27):28664-71.

[18] Yan R, Arezoomandan S, Sensale-Rodriguez B, Xing HG. Exceptional terahertz Wave modulation in graphene enhanced by frequency selective surfaces. ACS Photonics. 2016;3(3):315-23.

[19] Valmorra F, Scalari G, Maissen C, Fu W, Schönenberger C, Choi JW, et al. Low-bias active control of terahertz waves by coupling large-area CVD graphene to a terahertz metamaterial. Nano Letters. 2013;13(7):3193-8.

[20] Degl'Innocenti R, Jessop DS, Shah YD, Sibik J, Zeitler JA, Kidambi PR, et al. Low-bias terahertz amplitude modulator based on split-ring resonators and graphene. ACS Nano. 2014;8(3):2548-54.

[21] Gao W, Shu J, Reichel K, Nickel DV, He X, Shi G, et al. High-contrast terahertz wave modulation by gated graphene enhanced by extraordinary transmission through ring apertures. Nano Letters. 2014;14(3):1242-8.

[22] Liu PQ, Luxmoore IJ, Mikhailov SA, Savostianova NA, Valmorra F, Faist J, et al. Highly tunable hybrid metamaterials employing split-ring resonators strongly coupled to graphene surface plasmons. Nat Commun. 2015;6:8969.

[23] Tamagnone M, Fallahi A, Mosig JR, Perruisseau-Carrier J. Fundamental limits and near-optimal design of graphene modulators and non-reciprocal devices. Nat Photon. 2014;8(7):556-63.

[24] Yang K, Liu S, Arezoomandan S, Nahata A, Sensale-Rodriguez B. Graphene-based tunable metamaterial terahertz filters. Applied Physics Letters. 2014;105(9):093105.

[25] Allen SJ, Störmer HL, Hwang JCM. Dimensional resonance of the two-dimensional electron gas in selectively doped GaAs/AlGaAs heterostructures. Physical Review B. 1983;28(8):4875-7.

[26] Mikhailov SA, Ziegler K. New electromagnetic mode in graphene. Physical Review

Lett. 2007;99(1):016803.

[27] Hill A,Mikhailov SA, Ziegler K. Dielectric function and plasmons in graphene. EPL(Eurphysics Letters). 2009; 87(2):27005.

[28] Horng J, Chen CF, Geng B, Giriy C, Zhang Y, Hao Z, et al. Drude conductivity of Dirac fermions in graphene. Physical Review B. 2011;83(16):165113.

[29] Ren L, Zhang Q, Yao J, Sun Z, Kaneko R, Yan Z, et al. Terahertz and infrared spectroscopy of gated large-area graphene. Nano Letters. 2012;12(7):3711-15.

[30] Buron JD, Petersen DH, Bøggild P, Cooke DG, Hilke M, Sun J, et al. Graphene conductance uniformity mapping. Nano Letters. 2012;12(10):5074-81.

[31] Lee, C.K., Langley, R.J. Equivalent-circuit models for frequency-selective surfaces at oblique angles of incidence. IEEE Proceedings H-Microwaves, Antennas and Propagation. 1985; 395–399.

[32] Yilmaz, A.E., Kuzuoglu, M. Design of the square loop frequency selective surfaces with particle swarm optimization via the equivalent circuit model. Radioengineering. 2009; 18: 95–102.

[33] Keyrouz, S., Perotto, G., Visser, H.J. Lumped-elements tunable frequency selective surfaces. EUCAP; 2014: 475–478.

[34] Dewani, A.A., O'Keefe, S.G., Thiel, D.V., Galehdar, A. Optically transparent frequency selective surfaces on flexible thin plastic substrates. AIP Adv. 2015; 5: 27107.

[35] Yasar-Orten, P., Ekmekci, E., Turhan-Sayan, G. Equivalent circuit models for split-ring resonator arrays. PIERS Proceedings. 2010; 534–537.

[36] Jansen C, Al-Naib I.A.I., Born N, Koch M. Terahertz metasurfaces with high Q-factors. Applied Physics Letters. 2011;98(5):051109.

[37] Bae S, Kim H, Lee Y, Xu X, Park J-S, Zheng Y, et al. Roll-to-roll production of 30-inch graphene films for transparent electrodes. Nat Nano. 2010;5(8):574-8.

[38] Dong-Wook S, Jong Hak L, Yu-Hee K, Seong Man Y, Seong-Yong P, Ji-Beom Y. A role of HNO3 on transparent conducting film with single-walled carbon nanotubes. Nanotechnology. 2009;20(47):475703.

[39] Tao, H., Strikwerda, A.C., Fan, K., Bingham, C.M., Padilla, W.J., Zhang, X., Averitt, R.D. Terahertz metamaterials on free-standing highly-flexible polyimide substrates. J. Phys. Appl. Phys. 2008; 41: 232004.

[40] Choi, M., Lee, S.H., Kim, Y., Kang, S.B., Shin, J., Kwak, M.H., Kang, K.-Y., Lee, Y.-H., Park, N., Min, B. A terahertz metamaterial with unnaturally high refractive index. Nature. 2011; 470: 369–373.

[41] Deninger AJ, Göbel T, Schönherr D, Kinder T, Roggenbuck A, Köberle M, et al. Precisely tunable continuous-wave terahertz source with interferometric frequency control. Review of Scientific Instruments. 2008;79(4):044702.

CHAPTER 5

TUNABLE TERAHERTZ METAMATERIALS EMPLOYING LAYERED 2D-MATERIALS BEYOND GRAPHENE

5.1 Abstract

In this work we extend recent investigations on graphene/metal hybrid tunable terahertz metamaterials to other two-dimensional (2D) materials beyond graphene. For the first time, use of a nongraphitic 2D-material, molybdenum disulfide (MoS_2), is reported as the active medium on a terahertz metamaterial device. For this purpose, high-quality few-atomic layer MoS_2 films with controlled numbers of layers were deposited on host substrates by means of pulsed laser deposition (PLD) methods. The terahertz conductivity swing in those films is studied under optical excitation. Although no appreciable conductivity modulation is observed in single-layer MoS_2 samples, a substantial conductivity swing, i.e., 0 to ~0.6 mS, is seen in samples with ~60 atomic layers. Therefore, although exhibiting a much smaller maximum terahertz conductivity than that in graphene, which is a consequence of a much smaller carrier mobility, MoS_2 can still be employed for terahertz applications by means of utilizing multilayer films. With this in mind, we design and demonstrate optically-actuated terahertz metamaterials that

---

© 2017 IEEE. Reprinted, with permission, from S. Arezoomandan et al, Tunable Terahertz Metamaterials Employing Layered 2-D Materials Beyond Graphene, IEEE Journal of Selected Topics in Quantum Electronics 23 (1), 1-7, Feb. 2017.

simultaneously exhibit a large modulation depth (i.e., >2X larger than the intrinsic modulation depth by a bare MoS_2 film) and low insertion loss (i.e., <3 dB). The advantages of using a 2D material with a bandgap, such as MoS_2, rather than a gapless material, such as graphene, are: (a) a reduced insertion loss, which is owed to the possibility of achieving zero minimum conductivity, and (b) an enhanced modulation depth for a given maximum conductivity level, which is due to the possibility of placing the active material in a much closer proximity to the metallic frequency selective surface, thus allowing us to take full advantage of the near-field enhancement. These results indicate the promise of layered 2D materials beyond graphene for terahertz applications.

Index Terms— Terahertz, Metamaterials, Optoelectronics, 2D materials, Graphene, MoS_2.

5.2 Introduction

The terahertz region of the spectrum comprises the broad set of frequencies lying between the microwave and the optical spectral ranges. Terahertz technology promises multiple diverse applications including imaging, communications, spectroscopy, security, astronomy, and so on [1-2]. However, the scarcity of active materials capable of efficiently responding and effectively manipulating terahertz waves currently limits the progress in developing many of these applications. In this regard, tunable terahertz metamaterials have been proposed as an efficient means for manipulating terahertz wave propagation. Significant research has been carried out over the last decade on tunable metamaterial terahertz modulators enabling amplitude [3] or phase modulation [4], and employing various actuation mechanisms, i.e., including: optical [5-6], electrical [3-4, 7-8], thermal

[9], and mechanical [10] actuation. In this context, graphene has been proposed as a promising active material for reconfigurable terahertz applications because it can be integrated into a wide variety of substrates, its low cost, and its excellent terahertz response [11-18]. However, a key design factor (i.e., the possibility of tailoring the electric field enhancement in graphene) has been largely unexplored [19].

Graphene-based metamaterials demonstrated to-date usually comprise two elements: (*i*) a passive metallic frequency selective surface (FSS), and (*ii*) a single layer - or multiple layers- of graphene. Although in most reported metamaterials the graphene layers are placed in the same plane as the FSS, vertically stacking these layers and optimizing the separation between them can lead to better modulation performance. In this regard, Yan *et al.* showed both theoretically as well as experimentally that the field enhancement in graphene could be controlled via tailored placement of the graphene layers away from the plane of the FSS [20]. In general, the higher the electric-field enhancement in the plane of graphene, the more sensitive the terahertz transmission is to the graphene conductivity. However, close placement is often accompanied by a high insertion loss, which is owed to graphene having a finite minimum conductivity; i.e., if graphene is placed very close to the FSS the minimum conductivity of graphene will lead to a large loss in the terahertz transmission through the structure. Therefore, in graphene-based metamaterials, there exists a trade-off between modulation depth and insertion loss, which needs to be taken into account (and optimized) when designing the geometry of these structures [20]. Proof-of-principle demonstration of this phenomenon was shown using graphene layers, which were separated by a polyimide (PI) spacer from a passive metallic FSS. By placing the active graphene layers at various distances from the FSS, it was demonstrated that: (*a*)

it is possible to tailor the strength of the interaction between the terahertz waves and graphene, which is equivalent to arbitrarily enhancing the effective conductivity of graphene; and, (*b*) for a given conductivity swing in graphene, there exists an optimal placement leading to optimal modulation depth versus insertion loss tradeoff. *In this work we extend this hybrid terahertz metamaterial concept to other 2D-materials beyond graphene.*

Our discussion will be focused on metamaterials employing molybdenum disulfide (MoS_2). In recent years, a number of investigators have reported on time-resolved terahertz conductivity measurements in 2D-MoS_2 films. For instance, Strait *et al.* performed low temperature mobility measurements in multilayer MoS_2 and reported acoustic phonon scattering as the mobility limiting mechanism [21]. Studies on exciton annihilation in optically excited monolayers of MoS_2 were performed by Sun *et al.* [22]. Furthermore, Docherty *et al.* demonstrated ultrafast photoconductive response (< 1ps) in a single layer of MoS_2 [23]. These early works shed light on the potential of molybdenum disulfide for use in terahertz applications. More recently, *Cao et al*. reported terahertz modulators based on large-area multilayer MoS_2 films in Si-substrates [24]. The enhancement in the terahertz modulation was achieved by *p*-type doping of the MoS_2 sample. Moreover, a recent study by Chen *et al.* [25], showed an optically pumped Si-MoS_2 terahertz modulator with a high modulation depth (~75%). However, (i) optical excitation in these experiments not only altered the terahertz optical properties of the MoS_2 films, but also altered the properties of the Si substrate, and (ii) large levels of modulation depth were observed in cases where the MoS_2 samples were intrinsically doped (i.e., there was an initial finite terahertz conductivity even in the absence of optical pump). Thus, these reported modulation depth

levels were not only heavily dependent on the initial doping in MoS_2, but also, more importantly, *the fact that large modulation was observed could be attributed to an enhanced sensitivity of the terahertz transmission to the terahertz conductivity swing in the Si substrate under optical illumination, rather than by an enhanced terahertz absorption by MoS_2.*

5.3 Sample fabrication

The MoS_2 films employed in this work were fabricated using a pulsed laser deposition technique. For this purpose, a pulsed KrF excimer laser with a wavelength of 248 nm and pulse width of 25 ns was used along with a polycrystalline MoS_2 target, which was made by pressing MoS_2 powder. The substrate, single crystal sapphire with (0001) orientation, was kept at 700˚C and at a vacuum pressure of 1×10^{-6} torr during the deposition process. *The quantity of MoS_2 layers in these films was controlled by means of controlling the number of laser pulses*. Further details on the experimental growth procedures and on the quality of the films are given in [26].

Three samples, with different number of MoS_2 layers are analyzed in this work. These samples contain 1, 4, and 60 atomic layers of MoS_2. Figure 5.1 shows an optical image of the samples organized by number of layers (low-to-high from left-to-right). These MoS_2 samples were studied by means of terahertz time domain spectroscopy (with and without optical excitation) from where their dynamic terahertz response could be extracted (*Section III. A*). Following the metamaterial concept reported in Ref. [20], we then proceeded to fabricate MoS_2/metal hybrid structures. To fabricate these structures, we spin coated polyimide (PI-2600) on the MoS_2-on-sapphire samples. The polyimide was

cured by gradually increasing temperature to 300˚C. The sample was held at this set point for 30 minutes and then gradually cooled down to room temperature. Samples with varied polyimide spacer thickness were fabricated by means of altering the spin casting conditions. Finally, lithography, metal deposition, and lift-off steps were performed to define the metallic FSS. In Fig. 5.2a, we show a sketch of the final metamaterial structure. Either Al (in structures with finite PI spacer thickness) or Ti/Au (in structures with no PI spacer) were employed as the FSS metals. The choice of metal arises from the fact that Al adheres well to PI but Ti/Au does not adhere; conversely, Al does not adhere to MoS_2 while Ti/Au does. The overall metal thickness was set to 100 nm. Figure 5.2b shows an optical microscope image of a section of the fabricated metamaterial device and a detail of a unit cell.

5.4 Results and discussion

5.4.1 *Terahertz conductivity of PLD grown MoS2 films*. Samples were measured using a conventional terahertz time domain spectroscopy (TDS) setup, where the terahertz beam was generated via optical rectification in a ZnTe crystal pumped using an 810 nm amplified Ti-Sapphire laser with a pulse width of 75 nm and repetition rate of 1 kHz. The generated terahertz beam was normally incident on the samples that were placed between a set of parabolic mirrors. The transmitted THz beam was measured using an optical probe beam employing a second ZnTe crystal using an electro-optic sampling technique [27]. The measured time-domain terahertz waveform was Fourier transformed to extract the frequency response of the sample.

To optically excite the MoS_2 samples, a broadband 250 W quartz tungsten halogen

(QTH) lamp color temperature of 3400 K was employed. The lamp radiation was focused onto the sample yielding an optical intensity of 5 W/cm^2. A detailed diagram of the terahertz measurement setup is depicted in Fig. 5.3.

Each sample was measured with and without optical excitation. The extracted terahertz spectra was normalized to that of a reference sapphire substrate under the same illumination conditions. We found that samples measured in the absence of optical excitation (dark) showed unity transmittance, corresponding to zero terahertz conductivity, which is evidence of the as-grown samples being intrinsically undoped. However, when they were optically excited using the halogen lamp we observed evidence of a finite terahertz conductivity that increased with number of layers. The measured terahertz spectra for samples with 1, 4 and 60 atomic layers of MoS_2 (under lamp illumination) are depicted in Fig. 5.4; the extracted terahertz conductivities under these conditions were: 0.01 ± 0.07, 0.42 ± 0.06, and 0.65 ± 0.08 mS, respectively. The reason why the conductivity does not scale linearly with the number of layers is unclear at this point and will be the subject of future investigations. In the case of a single layer film, where the transmission is very close to 1.0, drift in the laser power can lead to an apparent transmission that is greater than unity at some frequencies.

5.4.2 *MoS_2/metal hybrid metamaterials: numerical simulations*. In order to predict the behavior of MoS_2/metal hybrid metamaterials, numerical simulations were performed using ANSYS HFSS. The unit cell dimensions were taken as 265 x 265 μm^2, and the length and width of the cross-shaped apertures were set to 194 and 23 μm, respectively, as depicted in Fig. 5.2b. MoS_2 films were modeled as layered impedances due to their small thickness, i.e., a few atomic layers, which is much smaller than the

relevant terahertz wavelengths. A relative permittivity of 10 was assumed for MoS_2 in accordance with Ref. [28]. No frequency dispersion was considered at this end. *In the first set of simulations, we varied the PI spacer thickness for a given MoS_2 conductivity*. Figure 5.5a depicts the simulated transmittance spectra for 0 mS and 0.65 mS conductivity levels, respectively, in agreement with the maximum conductivity swing observed in our films (see Fig. 5.4). In accordance with the discussion in Ref. [20], *it was observed that maximum modulation depth takes place in structures without PI spacer, which results from a stronger near-field light-matter interaction under this condition*.

We also analyzed the effect of electron relaxation time (τ) on the terahertz transmittance. For this purpose, the MoS_2 films were modelled employing a Drude dispersion. Assuming an effective mass of $0.45m_0$ [29-30] and mobility ranging between 2 and 100 $cm^2/V.s$ [31], which correspond to typical reported values in MoS_2, it can be observed that a common range of values for its electron momentum relaxation time should be between ~1 and ~25 fs. The Drude model used in our simulations is therefore of the form:

$$\sigma = \sigma_{DC}/(1 + \omega^2\,\tau^2); \quad \epsilon = \epsilon_r - (\sigma_{DC}\tau/\epsilon_0)/(1 + \omega^2\,\tau^2), \tag{5.1}$$

where $\varepsilon_r = 9$ is employed in agreement with the results in Ref. [32] for multilayer MoS_2. In the above expression σ_{DC} corresponds to the DC conductivity of the MoS_2 film (in [S/m] as per the HFSS definition) and ε_0 is the vacuum permittivity. A thickness of 5 nm was assumed during the constitutive parameter definition. However, results are independent of the assumed thickness due to the material being effectively modelled in HFSS as a zero-thickness layered impedance. It is also worth mentioning that the transmission is dominated by the components arising from σ_{DC}, and thus the results do not depend on the

assumed value for ε_r. In Fig. 5.5b, we show the simulated transmittance versus frequency for metamaterial samples with 2 μm PI spacer thickness and a MoS_2 conductivity level of 0.65 mS for various relaxation times (0, 1, 10, and 25 fs). Aside from a small red-shift in resonance, which is accompanied by a small increase in transmittance, no substantial differences are observed between all these four cases. *From this point of view, employing a frequency independent conductivity model can be assumed as a good (first order) approximation when modeling MoS_2 films*. This is consistent with our previous observations in graphene reported in Ref. [20].

5.4.3 *Experimental results on optically-actuated MoS_2/metal hybrid metamaterials.* We experimentally analyzed the terahertz transmission, with and without illumination, through multiple fabricated metamaterial samples. The samples were illuminated from the substrate side so that a similar amount of light flux reaches the MoS_2 layers upon illumination as in the case without FSS. As predicted by our simulations, the resonance in these structures occurs in the 0.2 to 0.4 THz frequency interval. In Fig. 5.6a, we show the measured transmittance through structures with varied PI spacer of d = 0, 2, and 6 μm, with and without illumination. We find that the closer the MoS_2 film is to the FSS, the largest the modulation depth, in accordance with the discussion in [20] and with the simulation results discussed in the previous section. This observation is a result of the strong light-matter interaction in the near field (see Fig. 5.5(c)). Moreover, it is noticed that the resonance blue-shifts as the PI spacer thickness is increased; the reasons behind this trend will be discussed in *Section 5.4.4*. In order to evaluate the effect of conductivity swing, or more precisely, maximum attainable conductivity, on the modulation performance, we measured the transmittance through samples with a different number of

MoS_2 layers (4 and 60 layers) and no polyimide spacer. The results from these measurements are shown in Fig. 5.6b. Not surprisingly, and in agreement with the simulation results depicted in Fig. 5.4, we find that samples having a larger number of MoS_2 layers provide a larger modulation depth. *The maximum experimentally achieved modulation depth in these MoS_2/metal hybrid metamaterial structures is ~20%, i.e., >2X larger than the intrinsic modulation by the same MoS_2 films when on the bare sapphire substrate.*

Finally, it is worth mentioning that the fact that the experimentally observed modulation is much smaller than what our simulations predict, as depicted in Fig. 5.5a, and also smaller than what we observed in our previous work utilizing graphene [20], is not because of the maximum conductivity attainable in MoS_2 being small, but rather a result attributable to the following two mechanisms: (*i*) since the MoS_2 films are grown on top of a sapphire substrate (n = 3.3), they are immersed in larger surrounding refractive index than the ones in our previous work, in which polyimide (n = 1.7) was the substrate. Overall, an environment with larger refractive index reduces the sensitivity of the terahertz transmission to the MoS_2 conductivity. (*ii*) In our samples, the MoS_2 films are placed in close proximity to the metallic FSS, which alters the optical field at the MoS_2 plane. Consequently, most of the optical excitation power could be reflected by the overall structure rather than being absorbed by the MoS_2 film as in the case without FSS. As a result, the effective optical power in the MoS_2, which determines the terahertz conductivity level in the material, can be much smaller than that in structures without an FSS. From this point of view, when placed in metamaterial structures and under optical illumination, the effective conductivity swing in MoS_2 might dramatically reduce from that under the

experimental conditions in Fig. 5.4.

Finally, it is worth mentioning that in terms of operation speed, the transient evolution of photo-excited carriers in MoS_2 is much slower than that in graphene. In this regard, decay times on the order of nanoseconds have been observed [33-34], which is longer than the picosecond times typically observed in graphene [35]. From this perspective, the maximum attainable operation speeds would be 3 orders of magnitude slower in MoS_2 structures than in graphene structures. Moreover, if employing electrical actuation in order to reconfigure the MoS_2 conductivity, we will also expect a much slower response due to the smaller carrier mobility in MoS_2 [31] than in graphene.

5.4.4 *Equivalent circuit model. The trends observed from our experimental and simulation results can be analytically described by representing the metamaterial structure via employing an equivalent circuit model,* as discussed in Ref. [20]. In this model, the MoS_2 film can be modelled as a parallel impedance of value $1/\sigma_{MoS2}$, where σ_{MoS2} corresponds to an "effective" terahertz conductivity, which can account for the near-field enhancement effects [20]. In the absence of optical excitation, σ_{MoS2} is zero, and the simulated transmission spectra can be described by:

$$\frac{T}{T_0} = \left|\frac{2}{2+j\omega C Z_o + Z_o/(j\omega L+R)}\right|^2. \quad (5.2)$$

The parameters R, L and C, derived from the equivalent circuit model depicted in Fig. 5.7a, can be extracted by fitting of the numerically simulated transmission spectra to Eqn. (5.2). In order to estimate these parameters for our particular FSS geometry and dielectric environment, we fitted our numerical simulation results for a device geometry with no PI spacer to the above formula, from where it was determined that: R = 0.35 Ω, L = 9.8 pH and C = 32 fF. A very good agreement is observed between the model and the

simulation data, as shown in Fig. 5.7b.

In addition, by analyzing Eqn. (5.2), we see that the resonance frequency in the metamaterial is given by:

$$\omega_0 = \sqrt{\frac{1}{LC} - \frac{R^2}{L^2}}. \tag{5.3}$$

Therefore, the fact that the resonance blue-shifts as *d* are increased can be understood from a decrease in the equivalent circuit capacitance, which is owed to a diminished effective permittivity seen by the FSS as the PI spacer thickness is increased. This trend is opposite to the tendency observed in our previous work [20]. The reason behind this difference is that whereas in our previous work increasing PI thickness increases the effective capacitance due to the PI layer being placed on top of the FSS, in our current work, the PI spacer is placed below the FSS rather than on top. Thus, since the refractive index of sapphire is larger than that of PI, it follows that the effective capacitance should decrease as *d* is increased. Moreover, although the FSS dimensions in this work are the same as those in our previous work, we notice that the equivalent circuit capacitance is ~3X larger, which can also be explained by the larger terahertz permittivity of sapphire with respect to that in polyimide.

Furthermore, when analyzing the transmittance at resonance, it can be shown that:

$$\frac{T}{T_0} = \left| \frac{1}{1+\frac{Z_0 RC}{2L}} \right|^2. \tag{5.4}$$

From Eqn. (5.4), two observations can be made: (a) the fact that the transmittance levels under no illumination through the metamaterial structures studied in this work, where sapphire is the substrate, is on the order of ~70%, whereas in our prior work, where polyimide substrates were employed, transmittance was >80%, is a result of having a larger

equivalent circuit capacitance; and (b) since as C decreases the transmittance increases; therefore, the transmittance peak not only blue-shifts as *d* is increased, but it also increases in magnitude as clearly depicted in Fig. 5.5.

5.5 Conclusion

In conclusion, we have analyzed 2D-material/metal hybrid tunable terahertz metamaterials. We showed for the first time that a layered 2D material other than graphene could be used. Through optical-actuation in few-atomic layer MoS_2 films, we showed that terahertz metamaterials simultaneously exhibiting modulation depth levels >2X larger than the intrinsic modulation depth by the MoS_2 film and low insertion loss (<3dB) can be realizable. The trends observed in our experimental measurements as well as in our simulation results were explained by an equivalent circuit model. Although MoS_2 was chosen as an example 2D material, the discussion in this work is general enough and can be extended to any other 2D material. Overall our results indicate the promise of 2D materials beyond graphene for terahertz applications. However, these materials need to be employed in multilayer form, and the operation speed is expected to be much smaller than that in graphene-based devices.

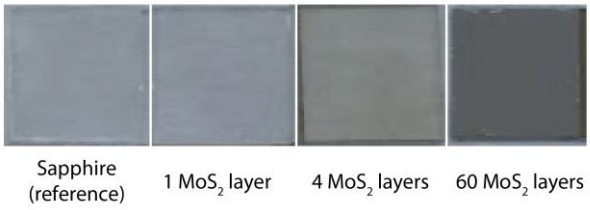

Fig. 5.1. Optical image of various MoS_2 films grown in sapphire substrates.

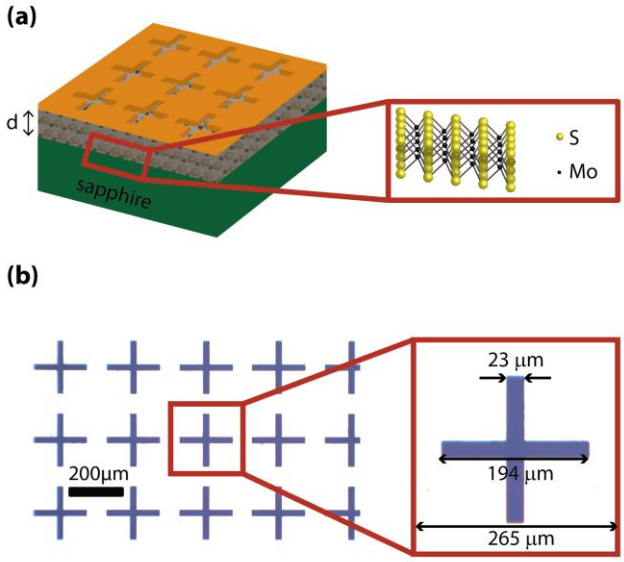

Fig. 5.2. (a) Schematic of a MoS_2/metal hybrid metamaterial structure. The polyimide spacer thickness, *d*, is varied in our experiments and simulations. (b) Optical image of a section of the metamaterial and detail of a unit cell.

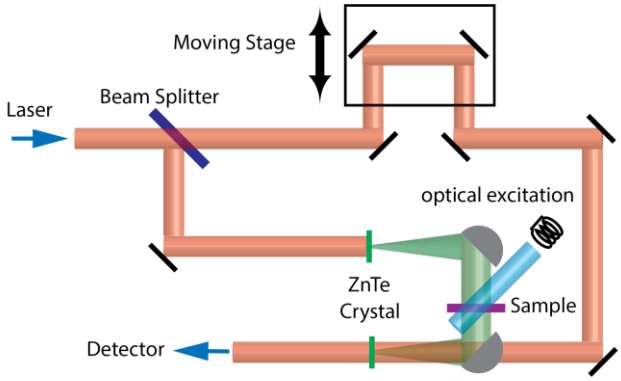

Fig. 5.3. Diagram of the terahertz time domain spectroscopy (TDS) setup. Actuation over MoS_2 is obtained via optical illumination employing a quartz tungsten halogen (QTH) lamp. The samples were illuminated through the substrate side.

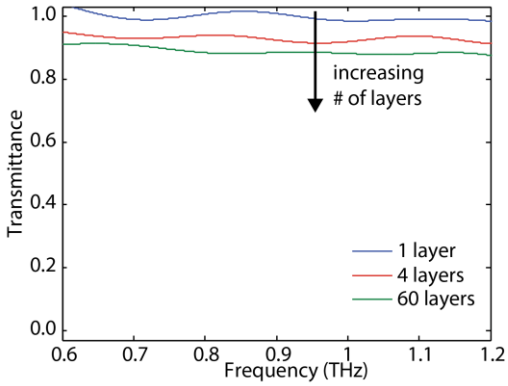

Fig. 5.4. Terahertz transmittance versus frequency for samples with varied number of MoS_2 layers under optical excitation. The measured transmittance under no optical excitation (not shown) is unity for all the analyzed samples, which is evidence of the as-grown material being intrinsically undoped.

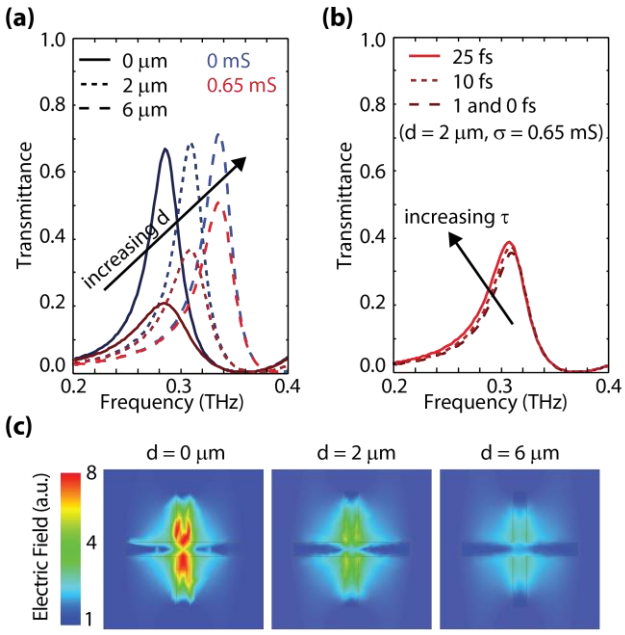

Fig. 5.5. (a) Simulated terahertz transmittance for metamaterial structures with varied spacer thickness (d = 0, 2, and 6 μm) and MoS_2 conductivity levels of 0 and 0.65 mS. (b) Simulated terahertz transmittance for metamaterial structures when employing a Drude model for MoS_2 and varying the electron momentum relaxation time (τ = 0, 1, 10, and 25 fs). The PI spacer thickness and MoS_2 conductivity were set to 2 μm and 65 mS, respectively. (c) Simulated electric field at resonance at the position where the MoS_2 film is placed for different PI thicknesses.

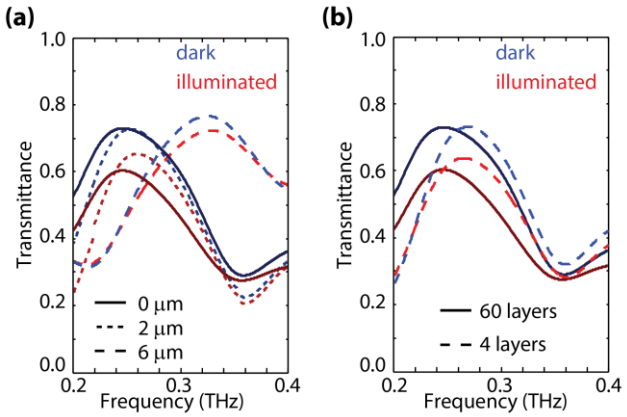

Fig. 5.6. (a) Measured terahertz transmittance (with and without illumination) for metamaterial structures with different spacer thickness (d = 0, 2, and 6 μm) for a sample with 60 atomic layers of MoS_2. (b) Measured terahertz transmittance (with and without illumination) for samples with no PI spacer and 4 and 60 MoS_2 layers. In all cases the insertion loss is <3 dB.

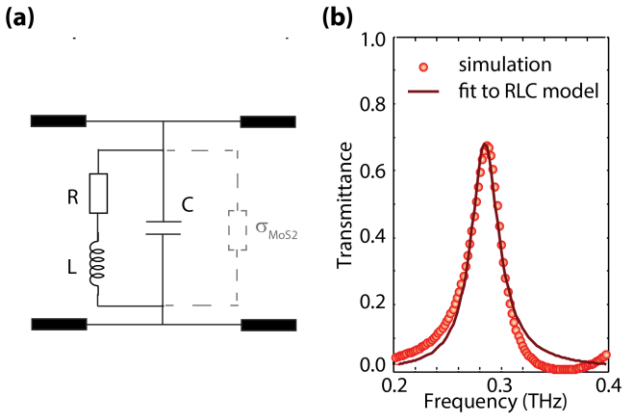

Fig. 5.7. (a) Equivalent circuit model. (b) Simulated and fitted transmission spectra for a structure containing the FSS in top of the sapphire substrate.

5.6 References

[1]. M. Tonouchi, "Cutting-edge terahertz technology," *Nat. Photon.,* vol. 1, pp. 97–105, 2007.

[2]. P. H. Siegel, "Terahertz technology," *IEEE Trans. Microw. Theory Tech.,* vol. 50, pp. 910-928, 2002.

[3]. H.-T. Chen, W. J. Padilla, J. M. O. Zide, A. C. Gossard, A. J. Taylor, and R. D. Averitt, "Active Terahertz Metamaterial Devices," *Nature,* vol. 444 pp. 597–600, 2006.

[4]. H.-T. Chen, W. J. Padilla, M. J. Cich, A. K. Azad, R. D. Averitt, and A. J. Taylor, "A metamaterial solid-state terahertz phase modulator," *Nature Photon.,* vol. 3, pp. 141–151, 2009.

[5]. H.-T. Chen, J. F. O'Hara, A. K. Azad, A. J. Taylor, R. D. Averitt, D. B. Shrekenhamer, and W. J. Padilla, "Experimental demonstration of frequency-agile terahertz metamaterials," *Nature Photon.,* vol. 2, pp. 295-298, 2008.

[6]. M. Kafesaki, N. H. Shen, S. Tzortzakis, and C. M. Soukoulis, "Optically switchable and tunable terahertz metamaterials through photoconductivity," *Journal of Optics,* vol. 14, p. 114008, 2012.

[7]. O. Paul, C. Imhof, B. Lagel, S. Wolff, J. Heinrich, S. Hofling, A. Forchel, R. Zengerle, R. Beigang, and M. Rahm, "Polarization-independent active metamaterial for high-frequency terahertz modulation," *Opt. Express,* vol. 17, no. 2, pp. 819-827, 2009

[8]. H.-T. Chen, S. Palit, T. Tyler, C. M. Bingham, J, M. O. Zide, J. F. O'Hara, D. R. Smith, A. C. Gossard, R. D. Averitt, W. J. Padilla, N. M. Jokerst, and A. J. Taylor, "Hybrid metamaterials enable fast electrical modulation of freely propagating terahertz waves," *Appl. Phys. Lett.,* vol. 93, p. 091117, 2008.

[9]. J. Han, and A. Lakhtakia, "Semiconductor split-ring resonators for thermally tunable terahertz metamaterials," *J. Mod. Opt.,* vol. 56, no. 4, pp. 554–557, 2009.

[10]. H. Tao, A. C. Strikwerda, K. Fan, W. J. Padilla, X. Zhang, and R. D. Averitt, "Reconfigurable terahertz metamaterials," *Phys. Rev. Lett.,* vol. 103, p. 147401, 2009.

[11]. B. Sensale-Rodriguez, R. Yan, L. Liu, D. Jena, and H. G. Xing, "Graphene for reconfigurable terahertz optoelectronics," *Proc. IEEE,* vol. 101, no. 7, pp. 1705–1716, 2013.

[12]. R. Degl'innocenti, D. S. Jessop, Y. D. Shah, J. Sibik, A. Zeitler, P. R. Kidambi, S. Hofmann, H. E. Beere, and D. Ritchie, "A Low-bias terahertz amplitude modulator based on split-ring resonators and graphene," *ACS Nano,* vol. 8, pp. 2548-2554, 2014.

[13]. F. Valmorra, G. Scalari, C. Maissen, W. Fu, C. Schönenberger, J. W. Choi, H. G. Park, M. Beck, J. Faist, C. L. Scho, "Low-bias active control of terahertz waves by coupling large-area CVD graphene to a terahertz metamaterial," *Nano Lett*., vol. 13, no. 7, pp. 3193–3198, 2013.

[14]. B. Sensale-Rodriguez, R. Yan, M. M. Kelly, T. Fang, K. Tahy, W. S. Hwang, D. Jena, L. Liu, and H. G. Xing, "Broadband graphene terahertz modulators enabled by intraband transitions," *Nat. Commun.*, vol. 3, p. 780, 2012.

[15]. B. Sensale-Rodriguez, R. Yan, S. Rafique, M. Zhu, W. Li, X. Liang, D. Gundlach, V. Protasenko, M. M. Kelly, D. Jena, L. Liu, and H. G. Xing, "Extraordinary control of terahertz beam reflectance in graphene electro-absorption modulators," *Nano Lett.*, vol. 12, no. 9, pp. 4518–4522, 2012.

[16]. H. K. Choi, S. H. S. Lee, C. Choi, S.-Y. Choi, X. Zhang, M. Choi, T.-T. Kim, M. Liu, X. Yin, B. Min, "Switching terahertz waves with gate-controlled active graphene metamaterials," *Nat. Mater.* vol. 11, no. 11, pp. 936–941, 2012.

[17]. H. Yan, X. Li, B. Chandra, G. Tulevski, Y. Wu, M. Freitag, W. Zhu, P. Avouris, and F. Xia, "Tunable infrared plasmonic devices using graphene/insulator stacks," *Nat. Nanotechnol.*, vol. 7, no. 5, pp. 330–334, 2012.

[18]. W. Gao, J. Shu, K. Reichel, D. V. Nickel, X. He, G. Shi, R. Vajtai, P. M. Ajayan, J. Kono, D. M. Mittleman, and Q. Xu, "High-contrast terahertz wave modulation by gated graphene enhanced by extraordinary transmission through ring apertures," *Nano Lett*., vol. 14, pp. 1242-1248, 2014.

[19]. R. Yan, B. Sensale-Rodriguez, L. Liu, D. Jena, and H. G. Xing, "A new class of electrically tunable metamaterial terahertz modulators," *Opt. Express*, vol. 20, no. 27, pp. 28664–28671, 2012.

[20]. R. Yan, S. Arezoomandan, B. Sensale-Rodriguez, and H. G. Xing, "Exceptional terahertz wave modulation in graphene enhanced by frequency selective surfaces," *ACS Photonics*, vol. 3, no. 3, pp. 315-323, 2016.

[21]. J. H. Strait, P. Nene, and F. Rana, "High intrinsic mobility and ultrafast carrier dynamics in multilayer metal-dichalcogenide MoS2," *Phys. Rev. B*, vol. 90, no. 24, pp. 245402, 2014.

[22]. D. Sun, Y. Rao, G. A. Reider, G. Chen, Y. You, L. Brezin, A. R. Harutyunyan, and T. F. Heinz, "Observation of rapid exciton–exciton annihilation in monolayer molybdenum disulfide," *Nano Letters*, vol. 14, no. 10, pp. 5625-5629, 2014.

[23]. C. J. Docherty, P. Parkinson, H. J. Joyce, M.-H Chiu, C.-H Chen, M.-Y Lee, L.-J Li, L. M. Herz, and M. B. Johnston, "Ultrafast transient terahertz conductivity of

monolayer MoS2 and WSe2 grown by chemical vapor deposition." *ACS Nano*, vol. 8, no. 11, pp. 11147-11153, 2014.

[24]. Y. Cao, S. Gan, Z. Geng, J. Liu, Y. Yang, Q. Bao, and H. Chen, "Optically tuned terahertz modulator based on annealed multilayer MoS2." *Scientific Reports*, vol. 6, p. 22899, 2016.

[25]. S. Chen, F. Fan, Y. Miao, X. He, K. Zhang, and S. Chang,"Ultrasensitive terahertz modulation by silicon-grown MoS2 nanosheets." *Nanoscale*, vol. 8, no. 8 pp. 4713-4719, 2016.

[26]. G. P. Siegel, Y. P. Venkata Subbaiah, M. C. Prestgard, and A. Tiwari, "Growth of centimeter-scale atomically thin MoS2 films by pulsed laser deposition," *APL Mater*., vol. 3, p. 056103, 2015.

[27]. J. Wang, S. Liu, and A. Nahata, "Reconfigurable plasmonic devices using liquid metals," *Opt. Express*, vol. 20, p. 12119, 2012.

[28]. X. Chen, Z. Wu, S. Xu, L. Wang, R. huang, W. Ye, W. Xiong, T. Han, G. Long, Y. Wang, Y. He, Y. Cai, P. Sheng, and N. Wang, "Probing the electron states and metal insulator transition mechanisms in molybdenum sisulfide vertical heterostructures," *Nature Comm.*, vol. 6, p. 6088, 2015.

[29]. T. Cheiwchanchamnangij, and W. R. L. Lambrecht, "Quasiparticle band structure calculation of monolayer, bilayer, and bulk MoS2," *Phys. Rev. B*, vol. 85, p. 205302, 2012.

[30]. H. Pelaeers, and C. G. Van de Walle, "Effects of strain on band structure and effective masses in MoS2," *Phys. Rev. B*, vol. 86, p. 241401(R), 2012.

[31]. S. Kim, A. Konar, W.-S. Hwang, J. H. Lee, J. Lee, J. Yang, C. Jung, H. Kim, J.-B. Yoo, J.-Y. Choi, Y. W. Jin, S. Y. Lee, D. Jena, W. Choi, and K. Kim, "High-mobility and low-power thin-film transistors based on multilayer MoS2 crystals," *Nat. Commun*., vol. 3, p. 1011, 2012.

[32]. X. Chen, Z. Wu, S. Xu, L. Wang, R. Huang, Y. Han, W. Ye, W. Xiong, T. Han, G. Long, Y. Wang, Y. He, Y. Cai, P. Sheng and N. Wang, "Probing the electron states and metal-insulator transition mechanisms in molybdenum disulphide vertical heterostructures," *Nat. Commun.*, vol. 6, p. 6088, 2015.

[33]. X. Liu, H. Yu, Q. Ji, Z. Gao, S. Ge, J. Qiu, Z. Liu, Y. Zhang, D. Sun, "An ultrafast terahertz probe of the transient evolution of the charged and neutral phase of photo-excited electron-hole gas in a monolayer semiconductor," *2D Materials*, vol. 3, no. 1, p. 014001, 2008.

[34]. S. Kar, Y. Su, R.R. Nair, A.K. Sood, “Probing photoexcited carriers in a few-layer mos2 laminate by time-resolved optical pump–terahertz probe spectroscopy,” *ACS Nano*, vol. 9, no. 12, pp. 12004-12010, 2015.

[35]. G. Jnawali, Y. Rao, H. Yan, T.F. Heinz, “Observation of a transient decrease in terahertz conductivity of single-layer graphene induced by ultrafast optical excitation,” *Nano Lett.*, vol. 13, no. 2, pp. 524-530, 2013.

CHAPTER 6

TERAHERTZ CONDUCTIVITY OF ULTRA HIGH ELECTRON CONCENTRATION 2DEGS IN NTO/STO HETEROSTRUCTURES

6.1 Abstract

We analyze the terahertz properties of complex oxide hetero-structures with record-high carrier concentration approaching 10^{15} cm^{-2}. Our results evidence a large room temperature terahertz conductivity, which corresponds to 3X to 6X larger nanoscale mobility than what is extracted from electrical measurements. That is, in spite of a relatively lower mobility, when taking into account its ultralarge carrier concentration, the 2DEG in complex oxide hetero-structures can still attain a large terahertz conductivity, which is comparable with that in traditional high-mobility semiconductors or large-area CVD graphene films.

The presence of a two-dimensional electron gas (2DEG) at the hetero-interface between, otherwise insulating, complex oxides has recently captured considerable attention [1-6]. This highly conductive 2DEG exists as a result of polarity discontinuities at the interface of the perovskite oxide crystals resulting from valence mismatch due to the presence of dangling bonds. Moreover, these hetero-structures exhibit intriguing physical phenomena and hold potential for novel electronic devices with promising properties like

The material provided in this chapter is available at: APL Materials 4 (7), 076107 (2017). Reprinted and adapted with permission from AIP Publishing.

a high breakdown voltage and an ultrahigh 2D electron density [7-8]. In addition, other interesting properties such as ferro-electricity [9-11], superconductivity [12-15], and negative magnetoresistance [16-17], have also been reported in these 2DEGs. In this context, complex oxide 2DEGs have been shown to support electron densities that are ~2 orders of magnitude larger than those in traditional semiconductor hetero-structures. Whereas for 2DEGs in III-V semiconductor hetero-structures typical maximum electron densities are in the order of $\sim 10^{13}$ cm^{-2} [18-19], two-dimensional electron densities approaching $\sim 10^{15}$ cm^{-2}, thus half an electron per unit cell, have been reported in complex oxide hetero-structures [20]. Based on the above properties, complex oxide 2DEGs hold promise as suitable candidates for the next generation of electronic and terahertz devices.

In recent work, via band engineering, Xu *et al*. [20] discovered and demonstrated the possibility of attaining a 2DEG with ultrahigh electron density at the interface of $NdTiO_3$ (NTO) and $SrTiO_3$ (STO). Although neither oxide conducts electricity as a pure material, such a 2DEG can be formed at the interface between polar NTO and nonpolar STO layers, and is confined within the STO side of the interface. Moreover, electronic reconstruction behavior above a certain critical thickness in these layers leads to a further enhancement in the electron density; hence, a record-high electron density of $\sim 3 \times 10^{15}$ cm^{-2} was reported in these 2DEGs. The room-temperature electron mobility from Hall measurements under a Van der Paw configuration was reported to be in the order of 1 to 10 $cm^2/V.s$. In this regard, it is worth noticing that the length-scale at which the 2DEG properties are characterized plays an important role on the measured values. In (DC) electrical measurements the characteristic length-scales at which electron transport is probed are set by the separation between contacts and thus are in the order of micrometers/millimeters.

Therefore, the extracted electron transport properties can be affected by extended effects over >μm areas. At such large scales, these properties can be significantly affected by scattering by dislocations, defects, and stacking faults. However, these extended effects can become considerably less pronounced if probing with high-frequency excitations in a contactless, quasi-optical manner. For instance, if probing with a quasi-optical excitation associated with frequencies in the terahertz range, i.e., by means of THz spectroscopy, one can probe for a spatially-averaged nanoscale sheet conductivity due to the very high frequency alternating current (AC) electric fields associated with the THz radiation [21]. In this case, typical characteristic length-scales for semiconductors as well as for metals are in the order of a few nanometers [22-23], and thus the extent to which such effects will degrade the extracted transport properties will be greatly diminished. In this context, *the aim of this paper is to analyze and compare the 2DEG transport properties extracted from DC measurements with the nanoscale properties extracted from THz spectroscopy in NTO/STO samples. For the first time, to the best of our knowledge, characterization of the electronic properties of such ultrahigh electron concentration 2DEGs in NTO/STO hetero-structures is performed via a noncontact method using THz spectroscopy. Our results evidence terahertz sheet conductivity >1 mS in all the analyzed samples at room-temperature. These extracted values correspond to 3X to 6X larger conductivity than what is extracted from DC measurements, which is an indication of a much larger nanoscale transport mobility than what is evidenced from the electrical measurements. Our results overall indicate that the 2DEG in these complex oxide hetero-structures can possess large THz conductivity, comparable with those in the 2DEGs of traditional high-mobility semiconductors or in typical-quality large-area CVD graphene films, and, therefore,*

despite a still lower mobility, might result in attractive active material for multiple terahertz as well as electronic applications.

Three different samples were analyzed: Sample #1 and #2 correspond to NTO/STO structures grown under different conditions, whereas Sample #3 corresponds to a STO/NTO/STO hetero-structure containing two 2DEGs, one at each interface. Depicted in Fig. 6.1a are sketches of the structures as well as a typical TEM detail of the grown films and interfaces. All the samples were grown by means of molecular beam epitaxy (MBE) employing LSAT ($[La_{0.3}Sr_{0.7}][Al_{0.65}Ta_{0.35}]O_3$) substrates. Details about the growth conditions for these samples are discussed in the *Experimental Section*. The electron concentration and mobility were obtained from Hall measurements; Table 6.1 depicts the extracted electrical transport properties as well as the thicknesses of the films forming the hetero-structures for each sample. The 2DEG in these hetero-structures shows indeed an ultrahigh carrier concentration ranging from ~0.3 to ~0.7×10^{15} cm^{-2}; that is two orders of magnitude larger than what is typical in traditional semiconductor 2DEGs. The carrier mobility ranged from ~2 to ~4 $cm^2/V.s$ at room temperature. The extracted DC sheet conductivity was 0.47 mS, 0.20 mS, and 0.19 mS, for Samples #1, #2 and #3, respectively.

Terahertz transmission measurements were performed for all samples employing a TOPTICA CW THz spectrometer [24]. The frequency sweep was limited to the range between 0.4 and 0.7 THz in such measurements in order to use a long averaging while not compromising on total scan time. Moreover, at this frequency range the terahertz properties of the LSAT substrate show very small frequency dependence [25]. Shown in Fig. 6.1b is the measured transmittance versus frequency for Sample #1, Sample #2, as well as a reference LSAT substrate. In order to extract the sheet conductivity of the 2DEG

from the THz transmission spectra, the experimental data are fitted to an analytical model. In this regard, the effect of the 2DEG on THz transmittance can be evaluated using the scattering matrix formalism [26]. The air/NTO-STO hetero-structure/substrate region is modelled with Fresnel coefficients (S) by neglecting the optical thicknesses of the NTO and STO layers, which is a reasonable assumption since these layers are in the order of a few nanometers and thus much smaller than the relevant THz wavelengths [26-27]. The associated S-matrix representing this region is given by:

$$S_{air/NTO-STO\ /\ substrate} = \begin{bmatrix} \frac{2n_{air}}{n_{air}+n_{substrate}+Z_0\sigma_{2DEG}} & \frac{n_{substrate}-n_{air}-Z_0\sigma_{2DEG}}{n_{air}+n_{substrate}+Z_0\sigma_{2DEG}} \\ \frac{n_{air}-n_{substrate}-Z_0\sigma_{2DEG}}{n_{air}+n_{substrate}+Z_0\sigma_{2DEG}} & \frac{2n_{substrate}}{n_{air}+n_{substrate}+Z_0\sigma_{2DEG}} \end{bmatrix}, \quad (6.1)$$

where Z_0 = 376.73 Ω is the vacuum impedance, σ_{2DEG} is the 2DEG sheet conductivity, n_{air} and $n_{substrate}$ are the refractive index of air (n_{air} =1) and the substrate (LSAT), respectively. For each of the other interfaces and for the propagation in the substrate, classical formulas for the Fresnel coefficients can be employed:

$$S_{substrate\ /\ air} = \begin{bmatrix} \frac{2n_{substrate}}{n_{air}+n_{substrate}} & \frac{n_{air}-n_{substrate}}{n_{air}+n_{substrate}} \\ \frac{n_{substrate}-n_{air}}{n_{air}+n_{substrate}} & \frac{2n_{air}}{n_{air}+n_{substrate}} \end{bmatrix}, \quad (6.2)$$

$$S_{propagation\ substrate} = \begin{bmatrix} e^{-jn_{substrate}k_0 d} & 0 \\ 0 & e^{-jn_{substrate}k_0 d} \end{bmatrix}, \quad (6.3)$$

where d is the substrate thickness, and $k_0 = 2\pi/\lambda_0$. With $\lambda_0 = c/f$, where c is the speed of light in vacuum, and f is frequency. Since we are working in the 0.3 to 0.7 THz frequency interval, where the LSAT properties do not show a significant frequency dispersion [25], the substrate will be modeled in Eqn. (6.1)-(6.3) using a frequency independent complex index of refraction. Depicted in Fig. 6.1c are the calculated transmission spectra that best fit to the experimental data in Fig. 6.1b employing the model in Eqn. (6.1)-(6.3); the real

and imaginary part of the substrate permittivity as well as the substrate thickness are set as fitting parameters thus extracted from the THz measurements. The substrate thickness was found to be non-uniform between samples, which explains the different positions of the Fabry-Perot peaks observed in the transmission spectra. The extracted 2DEG sheet conductivities obtained from fitting the experimental spectra to the model were 1.44 mS and 1.13 mS, for Samples # 1 and #2, respectively. This is 3.1X and 5.6X larger than the correspondent values extracted from DC measurements, respectively.

At this end, we proceed to study Sample #3. In contrast with Samples #1 and #2, which are grown in a 5 mm x 5 mm LSAT substrates, Sample #3 was grown in a 10 mm x 10 mm substrate, which besides being a suitable dimension for analysis in our CW THz system, where the spot size at the plane of the sample is in the order of 2 mm, it also constitutes a suitable dimension for analysis in our THz time-domain spectroscopy (TDS) system, where the spot size is in the order of 5 mm and the setup is more sensitive to sample misalignments. By selecting an appropriate time-window, so to subtract for contributions from multiple reflections, the 2DEG sheet conductivity can be experimentally determined by fitting the TDS transmission spectra to the following model, where a Drude dispersion was assumed for the 2DEG conductivity [28]:

$$\frac{T(\omega)}{T_0(\omega)} = \left| \frac{1}{1+Z_0\sigma_{2DEG}/(1+n_{substrate})(1+\omega^2\tau^2)} \right|^2 , \tag{6.4}$$

where $T(\omega)$ and $T_0(\omega)$ are the measured (power) transmissions through the NTO/STO sample under test and through a LSAT reference substrate, respectively. Here, τ is the electron momentum relaxation time in the 2DEG, and $\omega = 2\pi f$ is the angular frequency. In the 0.4 to 1.2 THz frequency range the real part of the LSAT refractive index slightly increases from 4.8 to 4.9, whereas its imaginary part (κ) is in the order of 0.02 [25]. For

the purpose of Eqn. (6.4), we will neglect the contribution of κ and assume $n_{substrate}$ = 4.8 as the refractive index of the LSAT substrate. The maximum error introduced by these assumptions was evaluated to be <1%. The relaxation time τ and the conductivity σ_{2DEG} are unknowns in Eqn. (6.4) and thus are found from fitting of the measured TDS transmittance spectra to Eqn. (6.4). Since our THz TDS setup is integrated with a cryostat, and in order to obtain a further insight into the electronic properties of this ultrahigh carrier density 2DEG, we studied the temperature dependence of the extracted electrical transport properties in the temperature range from 77K to room-temperature. The measured transmission spectra as well as its fit to Eqn. (6.4), for various temperatures, are depicted in Fig. 6.2a. We observe a decrease in transmission as the temperature decreases, a signature of an increased sheet conductivity, and, therefore, increased mobility at low temperature. Moreover, the Drude-like frequency dependence becomes more clearly apparent as temperature is decreased, which is a signature of a longer momentum relaxation time at low temperature. From these measurements, sheet conductivity and momentum relaxation time were extracted as a function of temperature by fitting of the experimental data to Eqn. (6.4). Depicted in Table 6.2 is a summary of the extracted parameters from these TDS measurements at various temperatures. In this regard, it is worth noticing that at room-temperature an excellent agreement is observed between the extracted conductivities from TDS and CW measurements as can be observed by scrutinizing Table 6.1 and Table 6.2. Moreover, a >2X increase in momentum relaxation time is observed when temperature is decreased from room temperature to 77K, which correlates well with the observed increase in conductivity. Sample # 3 was also electrically characterized as a function of temperature, from where its temperature dependent DC conductivity was

extracted. Shown in Fig. 6.2b are the extracted conductivities as a function of temperature from TDS as well as electrical measurements. On this regard, we notice that the >2X increase in the terahertz-extracted conductivity is accompanied by a similar increase in the DC-extracted conductivity when temperature is decreased from room temperature to 77K. A strong correlation is observed between the temperature trends for conductivity when comparing the results from THz and DC measurements. The fact that the ratio between these two measurements weakly depends on temperature could be interpreted as a signal of these methods probing transport at different scales, and, therefore, the differences in the extracted conductivity levels being mainly related to structural effects in the sample, which are temperature independent.

Overall, across all three studied samples, and across all the analyzed temperature range, the conductivity extracted from THz measurements (either CW or TDS) is consistently 3X to 6X larger than that extracted from DC measurements. At THz frequencies, the conductivity is determined by an effective characteristic length scale that follows a Debye model [29]. Assuming a diffusive electron transport under THz excitation [29-31], the characteristic length (L) follows:

$$L = \frac{D}{2\pi f}, \tag{5}$$

where:

$$D = \frac{\sigma_{DC} K_B T}{n_s e}. \tag{6}$$

with D being the diffusion constant, f the frequency, n_s the carrier density, e the elementary charge, σ_{DC} the sheet conductivity, K_B Boltzmann's constant, and T temperature. For the range of 2DEG electron densities and sheet conductivities extracted in our samples, we

find that at THz frequencies, i.e., $f > 300$GHz, the characteristic length is always < 10 nm. The scale of this characteristic length indicates that the sheet conductivity extracted from THz measurements is, in fact, a spatially-averaged nanoscale conductivity and is thus less affected by microscopic scale effects [30]. In contrast, the effects of defects and dislocations introduced during growth can compromise the values of sheet conductivity extracted from electrical measurements, where transport is probed at much larger length scales. Thus, *measurement using a noncontact method and gauging the nanoscale properties, such as THz spectroscopy, provides a relevant estimate of the intrinsic electrical properties of the 2DEG*. The behavior of the 2DEG as a less-defective layer in the nanoscale transport lengths probed by THz spectroscopy in contrast with its behavior as a highly-defective sheet in the microscopic transport length scales probed by electrical measurements is an explanation for the discrepancy between the THz-extracted and electrical-extracted sheet conductivity values as well as for the much larger THz-extracted levels. The THz-extracted sheet conductivity seems more pertinent when projecting the use of such 2DEGs in optoelectronic or nanoelectronic devices, where the relevant dimensions for electron transport, as dictated for instance by the gate-length in nanoscale field effect transistors, are also in the order of nanometers.

In conclusion, we discussed on the transport properties of ultrahigh electron concentration 2DEGs in complex oxides hetero-interfaces. Samples with record-high 2DEG electron density in NTO/STO were analyzed. We showed that contactless THz spectroscopy can probe the spatially-averaged nanoscale transport properties in these 2DEGs, whereas electrical measurements are highly sensitive to microscale effects, thus the THz-extracted properties constitute a better estimate of the intrinsic 2DEG electronic

properties. Our analysis reveals that the THz-extracted average sheet conductivity, thus nanoscale mobility in these 2DEGs, is 3-6X larger than what is extracted from DC measurements, which probe transport properties at much longer characteristic lengths. This can be attributed to defects, dislocation, and surface discontinuities which dominate on the microscale response. Our study suggests that NTO/STO hetero-structures can be attractive for electronic devices, and terahertz applications (e.g., in modulators), since the maximum attainable conductivity levels in its 2DEG are similar to those in III-V hetero-structures, such as AlGaN/GaN, or typical quality large-area CVD graphene.

The epitaxial oxide layers with cube-on-cube relationship with the substrates were grown on commercial, high structure quality (001) LSAT substrates (Crystech GmbH, Germany) using an hybrid MBE technique [MBE system: EVO 50, Omicron Nanotechnology, Germany] at a base pressure of 10^{-10} torr, as explained in Ref. [32]. The NTO/STO heterostructures were sequentially grown employing a metal-organic precursor of titanium tetraisopropoxide (TTIP) (99.999% from Sigma-Aldrich, USA) as a Ti source, which provides oxygen for the process. First a 3 nm stoichiometric STO layer was grown using an effusion cell as Sr source (99.99%, Sigma Aldrich APL, Milwaukee,Wisconsin) at 970º C; next the NTO layer was grown at substrate temperature of 900º C employing an effusion cell for Nd (99.99% from Ames Lab, USA). Postgrowth, the structure stoichiometry was characterized with X-ray diffraction and thin film diffractometric techniques [33].

The macroscopic electronic properties of the heterostructures were measured by a four-point Van der Pauw method [20]. For this purpose, wire-bonded contacts were applied at the corners of the samples, connecting to the STO interface as well as to the NTO

interface. For sample # 1 and #2, 300 nm of Au on top of 50 nm of Ti were sputtered as ohmic contacts for the NTO/STO/LSAT heterostructures, while 300 nm of Au on 20 nm Ni on top of 40 nm of Al were sputtered as ohmic contacts for the STO/NTO/STO/LSAT sample (Sample #3). The contacts were strategically placed so that they make a direct contact with the 2DEGs at the interfaces following the methods in [20].

For THz characterization two different setups were used, namely, a Continuous Wave (CW) THz spectrometer and a THz time-domain spectroscopy setup (THz-TDS). The CW THz spectrometer is a commercial setup from TOPTICA photonics, using InGaAs photo-mixers at 1550nm [24]. In the THz-TDS setup, a broadband THz pulse was generated by optical rectification of optical pulse in 1 mm thick (110) ZnTe crystal. The generated THz radiation is focused onto the sample and the response was modulated on the optical pulse using electro-optic sampling on the similar ZnTe crystal at the detector end [34]. The transmission is Fourier transformed to obtain the frequency response of the signal, which when normalized to the response of the LSAT reference provided for the properties of the complex oxide hetero-structures under test.

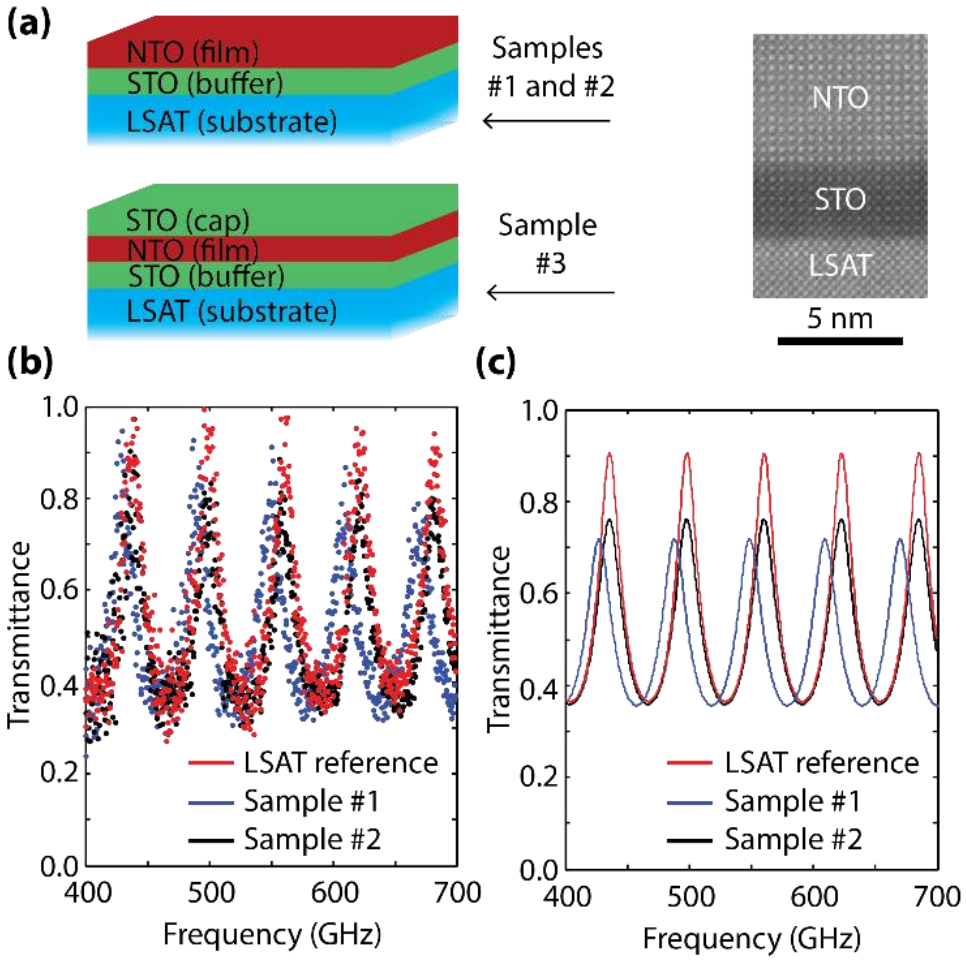

Figure 6.1. (a) Structure of the analyzed samples and TEM detail of the NTO/STO/LSAT interfaces. **(b)** Measured transmittance versus frequency for Samples #1, #2, and a LSAT reference substrate. **(c)** Best fit using the model in Eqns. (6.1)-(6.3) to the data in (b). Measurements were performed employing a CW THz spectrometer.

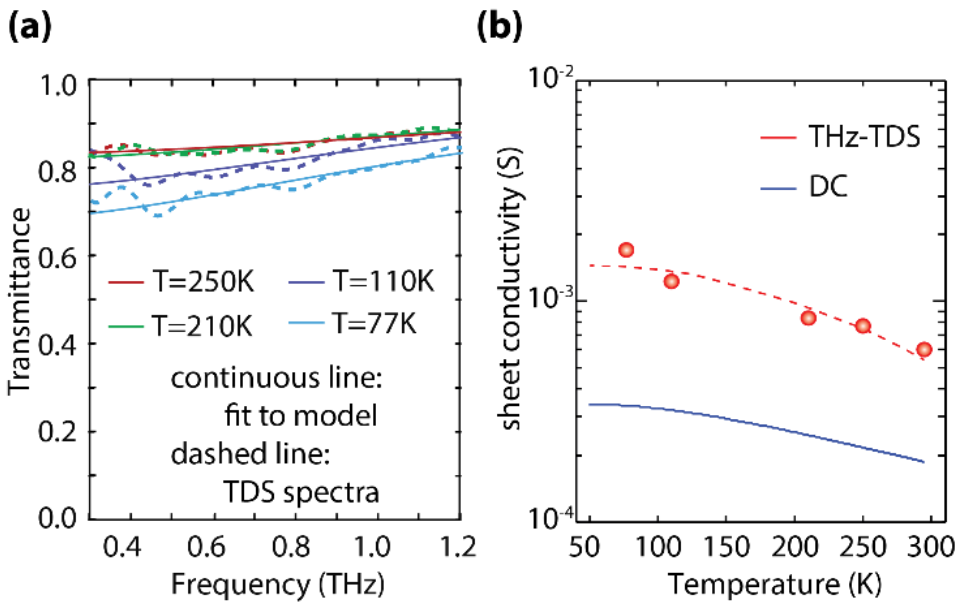

Figure 6.2. (a) Measured (dashed) and fitted (continuous) transmittance versus frequency for Sample #3 at various temperatures. Measurements were performed employing a THz-TDS setup, results were fitted to the model in Eqn. (6.4). **(b)** Extracted sheet conductivity versus temperature from THz-TDS measurements (red) as well as electrical measurements (blue).

Table 6.1. Sample properties and parameters extracted from electrical as well as CW-THz measurements

Sample	Structure	n_{2DEG} (cm^{-2})	μ_{HALL} ($cm^2/V.s$)	$\sigma_{extracted,\ DC}$ (mS)	$\sigma_{extracted,\ CW\text{-}THz}$ (mS)	$\mu_{nanoscale}/\mu_{HALL}$
#1	NTO/STO	$7.16x10^{14}$	4.11	0.47	1.44	3.1X
#2	NTO/STO	$3.64x10^{14}$	3.36	0.20	1.13	5.6X
#3 [(a)]	STO/NTO/STO	$5.20x10^{14}$	2.33	0.19	0.65 (x2)	3.4X

[(a)] Sample #3 contains two 2DEGs; the values listed in the table correspond to those in a single 2DEG, for this purpose the THz-extracted conductivity was divided by a factor of 2 for the purpose of listing in this table.

Table 6.2. Extracted sheet conductivity and relaxation time for various temperatures in Sample #3 from TDS measurements

Temperature (K)	$\sigma_{extracted,\ TDS}$ (mS)	$\tau_{extracted,\ TDS}$ (fs)
300	1.25 ± 0.02	<65
250	1.55 ± 0.02	93 ± 2.1
210	1.68 ± 0.02	111 ± 1.9
110	2.47 ± 0.04	140 ± 3.15
77	3.41 ± 0.04	147 ± 2.1

6.2 References

[1] Ohtomo, Akira, et al. "Artificial charge-modulation in atomic-scale perovskite titanate superlattices." Nature 419.6905 (2002): 378-380.

[2] Ohtomo, A., and H. Y. Hwang. "A high-mobility electron gas at the LaAlO3/SrTiO3 heterointerface." Nature 427.6973 (2004): 423-426.

[3] Nakagawa, Naoyuki Y., Harold Y. A. Hwang, and David A. Muller. "Why Some Interfaces Cannot Be Sharp." Nature Materials 5.3 (2006): 204-09.

[4] Park, J. W., et al. "Creation of a two-dimensional electron gas at an oxide interface on silicon." Nature Communications 1 (2010): 94.

[5] Thiel, Stefan, et al. "Tunable quasi-two-dimensional electron gases in oxide heterostructures." Science 313.5795 (2006): 1942-1945.

[6] Schlom, Darrell G., and Jochen Mannhart. "Oxide electronics: Interface takes charge over Si." Nature Materials 10 (2011): 168-169.

[7] Hwang, H. Y., Iwasa, Y., Kawasaki, K., Keimer, B., Nagaosa, N., and Tokura, Y. "Emergent phenomena at oxide interfaces." Nature Materials 11.2 (2012): 103-13.

[8] Zubko, P., Gariglio, S., Gabay, M., Ghosez, P., & Triscone, J. M. “Interface physics in complex oxide heterostructures.” Annu. Rev. Condens. Matter Phys., 2.1 (2011). 141-165.

[9] Brinkman, A, Huijben, M, Van Zalk, M, Huijben, J, Zeitler, U, Maan, J C, Van Der Wiel, W G, Rijnders, G, Blank, D H A, and Hilgenkamp, H. "Magnetic Effects at the Interface between Non-magnetic Oxides." Nature Materials 6.7 (2007)

[10] Bert, Julie A., et al. "Direct imaging of the coexistence of ferromagnetism and superconductivity at the LaAlO3/SrTiO3 interface." Nature Physics 7.10 (2011): 767-771.

[11] Ngo, T.D.N., Chang, J.-W., Lee, K., Han, S., Lee, J.S., Kim, Y.H., Jung, M.-H., Doh, Y.-J., Choi, M.-S., Song, J., and Kim, J. "Polarity-tunable magnetic tunnel junctions based on ferromagnetism at oxide heterointerfaces." Nature Communications 6 (2015)

[12] Reyren, Nicolas, et al. "Superconducting interfaces between insulating oxides." Science 317.5842 (2007): 1196-1199.

[13] Ueno, K., S. Nakamura, H. Shimotani, A. Ohtomo, N. Kimura, T. Nojima, H. Aoki, Y. Iwasa, and M. Kawasaki. "Electric-field-induced superconductivity in an insulator."

Nature Materials 7, no. 11 (2008): 855-858.

[14] Qing-Yan, Wang, Li Zhi, Zhang Wen-Hao, Zhang Zuo-Cheng, Zhang Jin-Song, Li Wei, Ding Hao et al. "Interface-induced high-temperature superconductivity in single unit-cell FeSe films on SrTiO3." Chinese Physics Letters 29, no. 3 (2012): 037402.

[15] Cheng, Guanglei, et al. "Electron pairing without superconductivity." Nature 521.7551 (2015): 196-199.

[16] Tsukazaki, A, Ohtomo, A, Kita, T, Ohno, Y, Ohno, H, and Kawasaki, M. "Quantum Hall effect in polar oxide heterostructures." Science 315.5817 (2007): 1388-91.

[17] Gardner, H. Jeffrey, Ashwani Kumar, Liuqi Yu, Peng Xiong, Maitri P. Warusawithana, Luyang Wang, Oskar Vafek, and Darrell G. Schlom. "Enhancement of superconductivity by a parallel magnetic field in two-dimensional superconductors." Nature Physics 7, no. 11 (2011): 895-900.

[18] Dang, X. Z., et al. "Influence of surface processing and passivation on carrier concentrations and transport properties in AlGaN/GaN heterostructures." Journal of Applied Physics 90.3 (2001): 1357-1361.

[19] Chau, R., Datta, S., and A. Majumdar. "Opportunities and challenges of III-V nanoelectronics for future high-speed, low-power logic applications." Compound Semiconductor Integrated Circuit Symposium, 2005. CSIC'05. IEEE. IEEE, 2005.

[20] P. Xu, T. C. Droubay, J. S. Jeong, K. A. Mkhoyan, P. V. Sushko, S. A. Chambers, and B. Jalan. "Quasi 2D ultrahigh carrier density in a complex oxide broken-gap heterojunction." Advanced Materials Interfaces 3.2 (2016)

[21] L. P. Gorkov, A. I. Larkin, and D. E. Khmelnitskii, “Particle conductivity in a two-dimensional random potential.” JETP Lett. 30, 248 (1979)

[22] Cooke, D. G., et al. "Transient terahertz conductivity in photoexcited silicon nanocrystal films." Physical Review B 73.19 (2006): 193311.

[23] Henning, P. F., et al. "Infrared studies of the onset of conductivity in ultrathin Pb films." Physical Review Letters 83.23 (1999): 4880.

[24] A. J. Deninger, T. Göbel, D. Schönherr, T. Kinder, A. Roggenbuck, M. Köberle, F. Lison, T. Müller-Wirts, and P. Meissner. "Precisely tunable continuous-wave terahertz source with interferometric frequency control." Review of Scientific Instruments 79, no. 4 (2008): 044702.

[25] T. Kiwa and M. Tonouchi. "Time-domain terahertz spectroscopy of (100)(LaAlO3)0.3 - (Sr2AlTaO6)0.7 substrate." Japanese Journal of Applied Physics

40.1A (2001): L38.

[26] Saleh, B. and Teich, M., *Fundamentals of Photonics, 2nd ed.*, Wiley, New York, NY, 2007.

[27] Sensale-Rodriguez, B., R. Yan, M. M. Kelly, T. Fang, K. Tahy, W. S. Hwang, D. Jena, L. Liu, and H. G. Xing. "Broadband graphene terahertz modulators enabled by intraband transitions." Nature Communications 3 (2012): 780.

[28] Tinkham, M. “Energy gap interpretation of experiments on infrared transmission through superconducting thin films”. Phys. Rev. 104, 845–846 (1956).

[29] Lundstrom, Mark, *Fundamentals of Carrier Transport*, Cambridge University Press, New York, NY, 2009.

[30] Buron, J. D., D. H. Petersen, P. Bøggild, D. G. Cooke, M. Hilke, J. Sun, E. Whiteway, P. F. Nielsen, O. Hansen, A. Yurgens, and P. U. Jepsen. "Graphene conductance uniformity mapping." Nano Letters 12.10 (2012): 5074-81.

[31] Buron, Jonas D., et al. "Electrically continuous graphene from single crystal copper verified by terahertz conductance spectroscopy and micro four-point probe." *Nano Letters* 14.11 (2014): 6348-6355.

[32] Wang, T., Ganguly, K., Marshall, P., Xu, P., & Jalan, B. (2013). Critical thickness and strain relaxation in molecular beam epitaxy-grown SrTiO3 films. Applied Physics Letters, 103(21), 212904.

[33] Xu, Peng, et al. "Stoichiometry-driven metal-to-insulator transition in NdTiO3/SrTiO3 heterostructures." Applied Physics Letters 104.8 (2014): 082109.

[34] Wang, Jinqi, Shuchang Liu, and Ajay Nahata. "Reconfigurable plasmonic devices using liquid metals." *Optics Express* 20.11 (2012): 12119-12126.

CHAPTER 7

THZ CHARACTERIZATION AND DEMONSTRATION OF VISIBLE TRANSPARENT/TERAHERTZ-FUNCTIONAL ELECTROMAGNETIC STRUCTURES IN ULTRACONDUCTIVE LA-DOPED BASNO3 FILMS

7.1 Abstract

We report on terahertz characterization of La-doped $BaSnO_3$ (BSO) thin-films. BSO is a transparent complex oxide material, which has attracted substantial interest due to its large electrical conductivity and wide bandgap. The complex refractive index of these films is extracted in the 0.3 to 1.5 THz frequency range, which shows a metal-like response across this broad frequency window. The large optical conductivity found in these films at terahertz wavelengths makes them an interesting platform for developing electromagnetic structures having a strong response at terahertz wavelengths, i.e., terahertz-functional, while being transparent at visible and near-IR wavelengths. As an example of such application, we demonstrate a visible-transparent terahertz polarizer.

The material provided in this chapter is available at: Scientific Report. 2018; 8: 3577. Reprinted and adapted with permission from Nature Publishing Group.

7.2 Introduction

Transparent electronics have garnered significant attention since the introduction of the first transparent thin film transistor [1]–[3]. In terms of commercial products, the market has been steadily flourishing, with demand being mostly led by the photovoltaic and the optoelectronic industries. Furthermore, these materials are expected to be convenient alternatives to conventional metals as well as doped-semiconductors in order to develop fully transparent devices. Several types of transparent conductive oxides (TCOs) have been introduced and characterized for different applications in plasmonics, photovoltaics, and so on, namely tin-doped indium oxide (ITO), gallium-doped zinc oxide (GZO), and aluminum-doped zinc oxide (AZO), among others [4]. Also, because of their large transmission in the near-IR and visible spectral ranges, TCOs could be employed as contacts in terahertz optoelectronic devices, terahertz photoconductive antennas, photo-active metamaterial structures, plasmon-assisted spectroscopy of materials, etc. [5]–[7], applications wherein the underlying material needs to be accessed optically. Moreover, being visible-transparent, these materials could be used to design structures whose optical response is encrypted at terahertz frequencies. On the other hand, spectroscopic characterization of these materials at terahertz frequencies reveals its high-frequency AC electronic transport properties, which could enrich the understanding of carrier dynamics in these materials and hence, help develop prospective devices with wider ranges of applications [8]–[10].

With rapid proliferation of optoelectronic devices and need for improved performance, demand for highly conductive and cost-effective TCOs has been on the rise. Among the TCOs demonstrated thus far, ITO has been shown to possess the largest

conductivity of ~10^4 S/cm, where Indium oxide is degenerately alloyed with Tin ($n \sim 10^{20}$ cm^{-3}) [11], [12]. However, in the future ITO might face a major bottleneck due to the potential scarcity of Indium, which could translate into higher production costs. In this regard, doped Zinc-oxide compounds have been proposed as potential replacements for ITO; however, these materials suffer from a much lower electrical conductivity [13]. Recently, thin films of ultraconductive $BaSnO_3$ (BSO) doped with Lanthanum were demonstrated and characterized [14], showing room-temperature conductivity ~10^4 S/cm; and high mobility of 120 $cm^2/V.s$ at carrier concentrations of ~ $3x10^{20}$ cm^{-3}. It is to be noted here that these mobility values are exceptionally high for such high carrier concentrations. This has been made possible due to a combination of low electron effective mass and weaker phonon scattering. A wide band-gap of 3 eV, together with ultrahigh conductivity and relatively high mobility in thin films, makes BSO a strong candidate as a transparent conducting oxide. Further characterization is required to reveal the true potentials of this material for different applications, including terahertz applications. Terahertz frequencies occupy a crucial region of the electromagnetic spectrum; introduction of ultrahigh conductive TCOs as a building block for visible-transparent terahertz devices would enrich the emerging technologies in this field.

Here, we present a comprehensive study on terahertz characterization of ultra-conductive La-doped BSO films grown on $(La_{0.3}Sr_{0.7})(Al_{0.65}Ta_{0.35})O_3$ LSAT(001). Details of film growth, structural and electronic characterizations can be found elsewhere [14]–[16]. Three sets of samples have been analyzed, with different levels of conductivity. The optical-transparency of the films at visible wavelengths was studied using visible spectroscopy while the terahertz optical properties and high-frequency carrier transport

properties were characterized using terahertz spectroscopy. By fitting the results to proper models, the optical properties of this material were extracted. Finally, we demonstrate a terahertz polarizer as a proof-of-concept visible-transparent terahertz-functional electromagnetic structure. The extracted results are compared with those reported in the literature from terahertz studies in ITO. Our results reveal BSO as an efficient visible-transparent terahertz-functional material in addition to establishing new avenues of research directions in this novel wide band-gap oxide films as potential TCO applications.

7.3 Experimental

In this study, BSO/LSAT(001) samples were prepared using a hybrid molecular beam epitaxy (MBE) technique [15], [16]. The films were grown epitaxially on 5mm x 5mm, 0.5 mm thick LSAT (001) substrates, where 45 nm thick undoped BSO was grown as a buffer layer. Next, an active layer of conductive La-doped BSO, $Ba_{1-x}La_xSnO_3$ was grown, where the value of *x* and, therefore, the carrier concentration *n* can be varied by changing the La-cell temperature during growth. In this study, three samples with different dopant densities are analyzed. For *Sample #1*, a 49 nm BSO film with nominally stoichiometric composition was grown. For *Sample #2*, a 46 nm film was grown intentionally with Barium deficiency, whereas for *Sample #3*, a 48 nm film was grown with Tin deficiency. La-concentration was kept fixed by keeping La-cell temperature constant. Table 7.1 summarizes the DC transport measurements for the three samples, which were obtained from Hall measurements. Rapid thermal annealing at 800^{o}C for 2 minutes was performed on the samples prior to the transport measurements. As shown in Table 7.1, stoichiometric La-doped BSO (*Sample #1*) showed the highest electron mobility,

86 cm^2/V.s, the highest conductivity, and the highest carrier concentration. *Samples #2 and #3* with Barium and Tin deficiencies showed mobilities of 71 and 17 cm^2/V.s, respectively, consistent with higher disorder due to nonstoichiometry [16]. In order to gain a better understanding on the effect of crystal defects on our characterization method we also analyze *Samples* #2 and #3, which were intentionally grown nonstoichiometric.

For the purpose of terahertz spectroscopy, samples were grown on LSAT substrates. LSAT(001) is used instead of STO(001) substrate – a typical substrate– due to the strong phonon absorption by STO in the terahertz frequency range. In view of this fact, the LSAT substrate, apart from being transparent at visible wavelength, showed negligible absorption in the terahertz frequency range [12,13]. To this end, samples grown on STO substrate were characterized using visible light spectroscopy in order to determine the transparency of the processed thin films. Figure 7.1 shows the transmission spectrum for (*i*) a La-doped BSO-film grown on STO, and (*ii*) a bare STO substrate. In the sample under study, the thickness of the La-doped BSO film is 132 nm and the conductivity extracted from DC transport measurement is 6.85×10^5 S/m, which is comparable to the conductivity values observed in samples grown on LSAT substrates. Measurements were normalized to transmission through air. *The results indicate that the transmission for the BSO sample on STO is larger than that through the STO substrate. This can be understood as the BSO film acting as an antireflection coating*. The insets in Fig. 7.1 depict an optical image of the analyzed La-doped BSO sample and the extracted refractive indices for BSO and the STO substrate by fitting of the transmission data in the visible spectrum to a proper model [19]. Also, depicted in Fig. 7.1 is the fitting of the measured data to this model (dashed curves), showing an excellent agreement with the experiments as well as explaining the

antireflection coating effect. The above results confirm that the La-doped BSO films are transparent across the entire visible range. The refractive index was found to be ~2 across a broad wavelength range from 400 to 800 nm, in agreement with previous reports [15,16].

7.4 Results and discussion

For the purpose of terahertz characterization, we employed the terahertz time-domain spectroscopy (THz-TDS) technique as our primary characterization tool. Using a conventional THz-TDS setup, see the *Methods* section, the complex-transmission through the BSO/LSAT samples was determined; the measured spectral response was normalized to that of the substrate so to independently resolve for the effect of the conductive La-doped BSO film. The normalized transmission data were used to directly extract the complex refractive index of the conductive film (as described in the *Methods* section).

Figure 7.2 depicts the normalized transmission for *Sample #1* at different temperatures (77K, 120K, 170K, 220K and 295K) in the 0.3 to 1.5 THz frequency range. The inset in Fig. 7.2 shows the time domain pulses measured for the reference LSAT substrate and the attenuated transmitted signal through the BSO/LSAT sample (at room temperature and 77K). Transmission in frequency is extracted from the Fourier transform of the received pulses and normalized to the transmission through the substrate and it is related to the conductivity value of the thin film inversely. As Fig. 7.2 depicts, the transmission levels decrease as temperature is decreased. This observation indicates an increase in the film conductivity as temperature is decreased. Furthermore, it can also be noticed that the transmission is flat in this frequency range. This observation indicates a short carrier momentum relaxation time in this material; even with an increase in mobility

at low temperatures, the momentum relaxation time is still relatively short and does not lead to spectral signatures in the analyzed frequency range.

From the complex transmission data, we extracted the refractive index and absorption coefficient following the procedure discussed in the *Methods* section. Figure 7.3 shows these extracted values. These values were found to be relatively high when compared to those reported from THz spectroscopy of typical ITO samples, e.g., [9]. The behavior of these parameters, together with the flat spectral response obtained in the THz-TDS measurements, see Fig. 7.2, is an indication of metal-like behavior from these degenerate-doped semiconductors. From the complex-transmission spectra, it is possible to also obtain a THz-extracted AC conductivity for the film [22]. Figure 7.4 depicts the THz-extracted AC conductivity for *Sample #1* as a function of temperature. Each transmission measurement was normalized to the measured transmission through the LSAT substrate at corresponding temperatures. The increase in conductivity with the decrease in temperature can be attributed to relaxation of phonon modes in these samples, hence curtailing the effect of electron-phonon scattering. The THz-extracted AC conductivity values at each temperature shown in Fig. 7.4 are statistically consistent with those observed in DC measurements. This differs from our previous observations in complex oxide 2DEGs [23], where much larger conductivity levels were extracted in the THz-measurements than in DC. Furthermore, whereas in our previous work [23], the largest differences between THz-extracted and DC-extracted conductivities were observed in nonstoichiometrically-grown samples, across all the analyzed samples in this work, i.e., *Samples #1* to *#3*, no statistical differences were observed between DC-extracted and THz-extracted conductivity levels.

In our previous work [23], we reported on terahertz characterization of the two-dimensional electron gas (2DEG) formed at the interface between polar/nonpolar complex oxides (e.g., NTO/STO). By contrasting results obtained from terahertz and DC characterization techniques, we showed that the electrical properties of the 2DEG are significantly affected by defects and scattering at the interface. Our measurements demonstrated a 3-6 X enhancement in the terahertz-extracted zero-frequency AC conductivity in these samples w.r.t. their DC conductivity [23]. Such enhancement was attributed to the characteristic length at which transport is probed in terahertz spectroscopy being much smaller than the mean free path between defect-induced scattering events [23]. Based on the extracted mobility levels, we estimated this characteristic length to be on the order of 10's of nm[23]. However, in the BSO thin-films analyzed in the current work, the mobilities extracted from Hall-effect measurements are larger – by more than one order of magnitude– than those observed in 2DEGs in NTO/STO. From this perspective, we expect the terahertz-probe length to be on the order of 100's of nm in the BSO samples under current study. Thus, as a result of (*i*) a longer characteristic length at which terahertz transport is probed in these samples having larger mobility, and (*ii*) a longer mean free-path between scattering events that leads to a larger mobility in these samples, no substantial differences between DC-extracted and THz-extracted conductivity levels are expected in the BSO films. Another important factor to be considered here is that free carriers in the NTO/STO heterostructure were confined to a quasi-two-dimensional interface; however, here carriers are present in a three-dimensional BSO layer. The (*iii*) additional degree of freedom for carrier transport as a result of this increased dimensionality would limit the impact of scattering by structural defects in these samples.

Therefore, the close agreement between DC-extracted and THz-extracted conductivity across all samples can be understood on the basis of a larger mean free-path between scattering events as well as on a higher carrier confinement dimensionality.

In order to further validate our results and observations, we performed continuous-wave (CW) terahertz spectroscopy. In the CW-THz setup, data were obtained in the 0.3 to 0.7 THz frequency range. Depicted in Fig. 7.5 are the measured transmission spectra for Samples #1, #2, #3, as well as for a bare LSAT substrate; each transmission measurement was referenced to those in free-space. In this measurement since the transmission data are normalized to those in free-space, Fabry-Perot resonances resulting from the substrate optical thickness are present. Once the transmission data were taken, the measured response was modelled employing a constant conductivity model to represent the conductive La-doped BSO film. Furthermore, the substrate was modelled with appropriate thickness and refractive index to accurately represent the Fabry-Perot resonances associated with the finite thickness of the samples. By fitting the measured data to this model, see *Methods* section, THz-extracted AC conductivities of 7.9±0.2, 4.0±0.6, and 0.4±0.05 $\times 10^5$ S/m were obtained for Samples #1, #2, and #3, respectively. Overall, across all the analyzed samples a close agreement was observed between extracted conductivity levels from THz-TDS, CW-THz, and DC measurements.

7.5 Applications

High carrier concentration, hence, high-conductivity on the analyzed La-doped BSO films leads to a metal-like response from these degenerate-semiconductors at terahertz frequencies. The fact that these TCOs showed a very large terahertz-conductivity

implies that these films could be employed to design terahertz-functional electromagnetic structures that are transparent to near-IR and visible wavelengths. As a proof-of-concept, we designed a simple grid-polarizer by patterning of the La-doped BSO films. A polarizer is a structure that lets electromagnetic waves of a specific polarization pass and blocks waves with perpendicular polarizations. In the case of a perfect polarizer the co-polarized transmission should be 100% and the cross-polarized transmission should be zero. The design geometry for the polarizer was determined with the help of full wave simulations using ANSYS HFSS. We chose a design having a wire width of 17.2 μm and 20 μm periodicity. For this purpose, *Sample #1*, i.e., the sample with the highest conductivity, was patterned using standard lithography and etching techniques (Ar ion milling). The response of the patterned-film was measured using our THz-TDS system as a function of incident-beam polarization. Depicted in Fig. 7.6 are the results from these measurements. For cross-polarized excitation, the transmission was 14%, while for co-polarized excitation the transmission was 88%. These experimental results were largely consistent with our simulated response, as also shown in Fig. 7.6. In order to give further insight into the scaling of the polarizer performance with BSO-film thickness, we performed simulations for polarizers in 200 nm thick films by using the same terahertz-conductivity levels as experimentally determined in *Sample #1*. Furthermore, in order to provide a qualitative comparison, we also performed simulations for these polarizers using 50 nm thick gold as the conductive material. Although in both cases, the gold-based polarizer shows a better performance, in terms of co- and cross-polarized transmission levels, the BSO structures are transparent at near-IR and visible wavelengths, which might be attractive for many terahertz system level applications. Furthermore, by scaling the film thickness, better

polarizer response can be obtained. It is to be noted here that, being a doped, wide band-gap semiconductor, our films demonstrate one of the highest reported conductivity levels from a TCO to-date, which is on-par of the best reported in ITO [24]. Furthermore, contrary to other highly conductive "effectively transparent" semiconductors, such as graphene, in which the high-conductivity arises from a very large electron mobility, the high conductivity in BSO is the result of an ultralarge charge density, in spite of a moderate mobility. As a result, highly conductive TCOs such as BSO have a metallic-like optical response across a wide range of terahertz wavelengths. In contrast, in high-electron mobility "transparent" semiconductors, such as high-quality graphene, the terahertz optical conductivity drops with frequency as a result of a long momentum relaxation time. From this perspective, terahertz-active and visible-transparent electromagnetic structures in BSO can provide for a broader terahertz frequency window of operation. From all these perspectives, ultraconductive La-doped BSO holds bright prospects as a transparent material for the development of future terahertz devices.

7.6 Conclusions

In conclusion, we have reported on terahertz characterization of BSO thin-films. Our BSO films show one of the largest electrical conductivities in any TCO demonstrated to date, which is on par with the best reports in ITO. Our terahertz measurements evidence a metallic response of these films in a broad frequency range from 0.3 to 1.5 THz. Furthermore, visible spectroscopy shows that BSO is transparent in the 400 to 800 nm wavelength window. As a result of its large broadband terahertz conductivity, and large visible transmission, BSO constitutes an interesting material for the design of

electromagnetic structures, such as polarizers, that are functional at terahertz frequencies but transparent in the near-IR to visible range. From this perspective BSO is a strong candidate for future transparent devices for terahertz applications.

7.7 Methods

7.7.1 Film synthesis. Thin films of doped $BaSnO_3$ were grown on LSAT (001) substrates using a hybrid molecular beam epitaxy approach. The method utilizes a metal-organic precursor (hexamethylditin) for Tin [15], a solid source for barium provided through an effusion cell, and an RF plasma source for oxygen. Oxygen plasma was operated at 250 W at a pressure of 5×10^{-6} Torr. Barium beam equivalent pressure (BEP) was kept constant at 5×10^{-8} Torr. Lanthanum (La) was used as an n-type dopant to make the films conducting. The dopant density was kept nominally fixed by keeping the La effusion cell temperature at 1230 °C. A substrate temperature of 900 °C was used for growing 45-50 nm thick of La-doped $BaSnO_3$ layer on top 45-50 nm of undoped $BaSnO_3$ buffer. Films were grown with three different tin precursor flux of 1.0×10^{-6} Torr (Sn-deficient), 1.4×10^{-6} Torr (stoichiometric) and 1.5×10^{-6} Torr (Ba-deficient). Structural characterization was done using in situ Reflection High Energy Electron Diffraction (RHEED) and X-ray Diffraction. DC transport measurements were performed in a conventional van der Pauw configuration using a Physical Property Measurement System (Dynacool). Indium was used as Ohmic contacts.

7.7.2 Ion milling. BSO films were dry etched using Argon plasma in an Intlvac Ion Mill. Argon plasma was operated at 75 W with a gas flowrate of 25 sccm. Substrate was tilted at 75° with respect to the normal and cooled down to 6°C to avoid overheating

during the process. Etching was performed down to the substrate to form a polarizer structure as shown in the inset of Figure 6.

7.7.3 Terahertz spectroscopy. THz-TDS: the terahertz signal was generated by optical rectification in a ZnTe crystal pumped by an 810 nm amplified Ti-Sapphire laser with pulse width of 75 nm and repetition rate of 1 kHz. The terahertz signal was then focused on the samples, which were placed inside a cryostat chamber for the purpose of cryogenic measurements, using two parabolic mirrors. Then, the response signal is focused and sampled on the optical probe beam by using another ZnTe crystal by electro-optic sampling technique. The obtained time domain terahertz waveform is Fourier transformed to extract the frequency response of the sample.

THz-CW: the samples were also tested in a diode-laser-driven photomixing spectrometer. The spectrometer is a commercial system from Toptica photonics. In this system, two lasers with center wavelength of 1500 nm are photo mixed for generation and detection of the terahertz signal. The sample is placed in the collimated region between parabolic mirrors.

7.7.4 Visible spectroscopy. Visible spectroscopy was performed using a Perkin-Elmer LAMBDA 950 UV-Vis-NIR Spectrophotometer with a 150 mm PbS integrating sphere in the wavelength range from 390 to 800 nm with steps of 1 nm.

7.7.5 Modelling. (a) THz-TDS: direct extraction of the complex refractive index. The transmission through a thin optical film (medium #2) sandwiched between two thick optical materials (mediums #1 and #3) normalized to the transmission from medium #1 to #3, can be modelled by [9, 25]:

$$T_{sample}(\omega) = \frac{E_{sample}(\omega)}{E_{substrate}(\omega)} = \frac{t_{12}t_{23}e^{\frac{i(n_2-1)d\omega}{c}}}{t_{13}} FP(\omega) \quad (7.1)$$

where n_2 is the refractive index of medium #2, d is its thickness, c is the speed of light, ω is angular frequency, t_{ij} is transmission from medium i to medium j and is defined as $t_{ij} = \frac{2n_i}{n_i+n_j}$, and FP(ω) is a Fabry-Perot term set by the multiple reflections inside the optically thin slab and defined as:

$$FP(\omega) = \frac{1}{1-r_{21}r_{23}e^{j2n_2d\omega/c}} \quad (7.2)$$

in which, r_{ij} is the reflection from the interface of medium i and j and defined as $r_{ij} = \frac{r_i-r_j}{r_i+r_j}$. Here, medium #1 is air and medium #3 is the LSAT substrate. By fitting the visible transmission data to this model, the refractive index of the BSO layer can be extracted at each frequency.

(b) THz-TDS: extraction of conductivity from transmission spectra. The optical conductivity of the BSO film was extracted from the transmission data by fitting to [22]:

$$1 - \left|\frac{T}{T_0}\right|^2 = 1 - \frac{1}{\left|1+\frac{\sigma(\omega)Z_0}{n_s+1}\right|^2} \quad (7.3)$$

where, Z_0 is the characteristic impedance of free space, n_s is the refractive index of the substrate, and σ(ω) is an effective 2D conductivity for the La-doped BSO layer, i.e., conductivity [S/m] multiplied by thickness of the film. The above formula is valid for situations where the effective optical thickness of the film is much smaller than the relevant terahertz wavelengths, which is the case in our study. Since the measured transmission did not exhibit significant frequency variations, the measured data were fitted to the above formula assuming a constant conductivity.

(c) CW-THz spectroscopy: extraction of conductivity from transmission spectra. In CW measurements, multiple reflections from the substrate need to be considered; therefore a different theoretical framework needs to be employed so to model the data. For this purpose, the ABCD matrix formalism is employed. By fitting of the experimental data to this analytical model the conductivity of the film is extracted. It is worth mentioning that since the BSO film is very conductive, we are not capable of determining its real part of permittivity employing this approach. The LSAT substrate is modelled by [26]:

$$\begin{pmatrix} A & B \\ C & D \end{pmatrix}_{LSAT} = \begin{pmatrix} \cos(\Phi_{LSAT}) & \mathrm{j}Z_{LSAT}\sin(\Phi_{LSAT}) \\ \mathrm{j}\frac{1}{Z_{LSAT}}\sin(\Phi_{LSAT}) & \cos(\Phi_{LSAT}) \end{pmatrix} \tag{7.4}$$

where: $\Phi_{LSAT} = \frac{n_{LSAT}\omega d_{LSAT}}{c}$, n_{LSAT} is the refractive index of the LSAT substrate, ω in angular frequency, d_{LSAT} is the thickness of the LSAT substrate and c is the speed of light. Furthermore, $Z_{LSAT} = \frac{Z_0}{n_{LSAT}}$, where Z_0 is the vacuum impedance. The transmission through the LSAT substrate can be extracted using the following formula [26]:

$$T = \frac{2}{A+\frac{B}{Z_0}+CZ_0+D} \tag{7.5}$$

The doped BSO film can also be modelled by an ABCD matrix:

$$\begin{pmatrix} A & B \\ C & D \end{pmatrix}_{BSO} = \begin{pmatrix} \cos(\Phi_{BSO}) & \mathrm{j}Z_{BSO}\sin(\Phi_{BSO}) \\ \mathrm{j}\frac{1}{Z_{BSO}}\sin(\Phi_{BSO}) & \cos(\Phi_{BSO}) \end{pmatrix} \tag{7.6}$$

where: $\Phi_{BSO} = \frac{n_{BSO}\omega d_{BSO}}{c}$, n_{BSO} is the complex refractive index of the BSO layer, and d_{BSO} is its thickness. The complex refractive index can be defined as:

$$n_{BSO} = \sqrt{\varepsilon_r - j\frac{\sigma_{BSO}}{\omega\varepsilon_0}} \approx \frac{(1+j)}{\sqrt{2}}\sqrt{\frac{\sigma_{BSO}}{\omega\varepsilon_0}} \tag{7.7}$$

here: ε_0 is the vacuum permittivity, and σ_{BSO} is the conductivity of the BSO film. In this

case, the ABCD matrix representing the total structure can be found from the matrix multiplication of $(ABCD)_{total} = (ABCD)_{LSAT}.(ABCD)_{BSO}$. It is worth mentioning again that in the analyzed frequency ranges, the transmission was found to be constant over frequency. Therefore, the terahertz optical conductivity was modeled as a constant across this frequency range.

7.8 Acknowledgement

The work involving terahertz characterization of the samples was supported primarily by the NSF MRSEC program at the University of Utah under grant DMR #1121252. We also acknowledge support from the NSF awards ECCS #1407959 and #1351389 (CAREER). The work involving thin films growth and DC transport measurements at the University of Minnesota was supported primarily by the AFOSR Young Investigator Program (FA9550-16-1-0205). The work also acknowledges partial support from National Science Foundation through DMR-1741801. We also acknowledge the use of facilities at the UMN Characterization Facility and the Nanofabrication Center, which receives partial support from the NSF through the MRSEC program at the University of Minnesota.

Table 7.1. DC extracted parameters for the analyzed BSO samples

	Thickness (nm)	Carrier concentration (cm^{-3})	Mobility ($cm^2/V.s$)	Resistivity ($\Omega.cm$)
Sample #1	49.3	6.75×10^{20}	86	1.06×10^{-4}
Sample #2	45.8	3.73×10^{20}	71	2.36×10^{-4}
Sample #3	48.0	1.27×10^{20}	17	2.93×10^{-4}

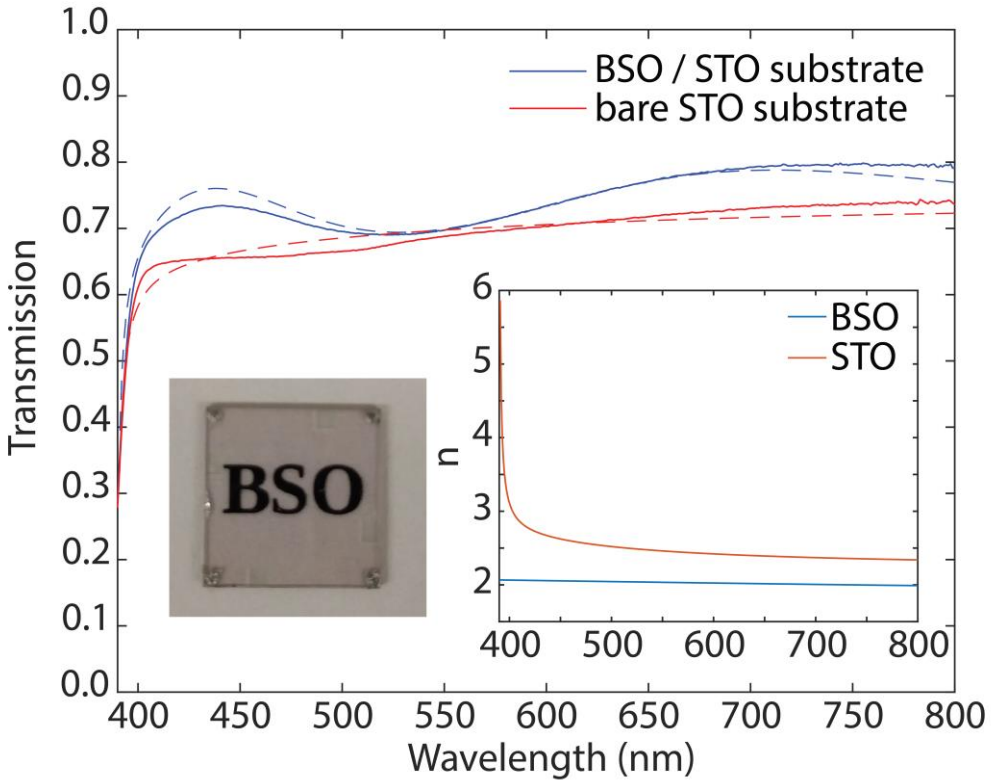

Figure 7.1. Measured optical transmission through a 132-nm film of La-doped BSO grown on an STO substrate (blue trace) as well as optical transmission through an STO bare substrate (red trace) in the visible spectrum. Fitted curves for the measured data to the model described in the *Methods section* are indicated by dashed lines. The right inset shows the extracted refractive indices for BSO and the STO substrate extracted from this fitting. The left inset shows a picture of one of the analyzed samples showing its transparency.

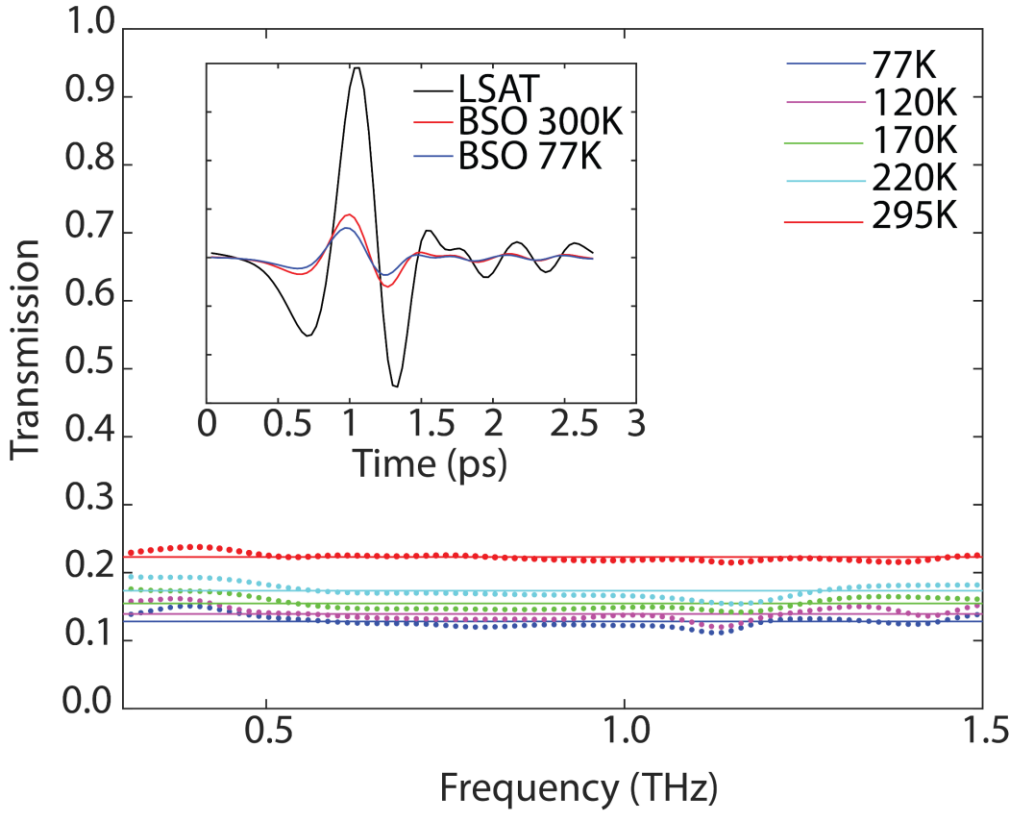

Figure 7.2**.** Measured terahertz transmission through Sample #1. The transmission is normalized to that of a bare substrate at each temperature. The experimental data points are indicated with dots, whereas fits to the model discussed in methods section are depicted with solid lines. The inset shows the measured terahertz pulse through the LSAT substrate at room temperature as well as the pulses through Sample #1 at room temperature and 77K.

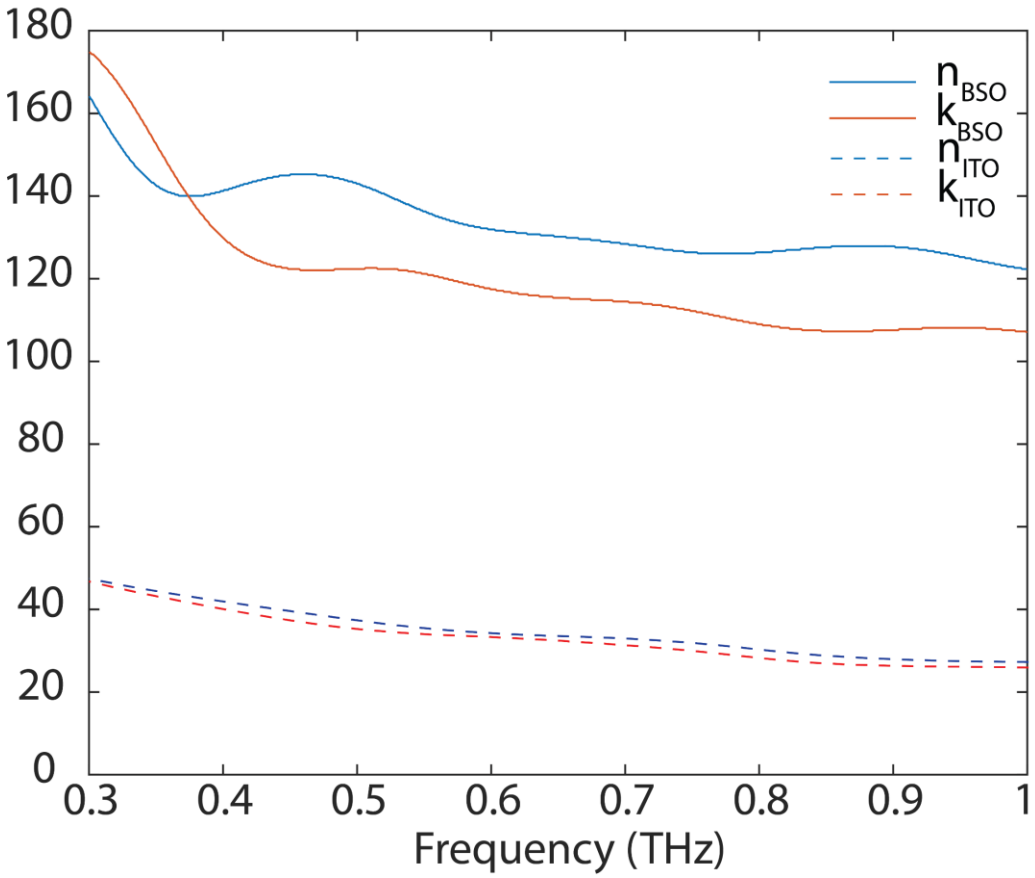

Figure 7.3. Real(*n*) and imaginary(*k*) part of refractive index vs. frequency for Sample #1. These parameters are directly extracted from the complex TDS transmission. In addition to the extracted values for our La-doped BSO sample (49.3nm thick film), data reported in the literature [9] for an ITO film (345 nm thick) are also depicted in the plot. In both cases a metal-like response is observed. The conductivity levels observed in the analyzed BSO samples are on par with the best results reported in the literature for ITO [27], and larger than those for the samples studied by terahertz spectroscopy in Ref. [9].

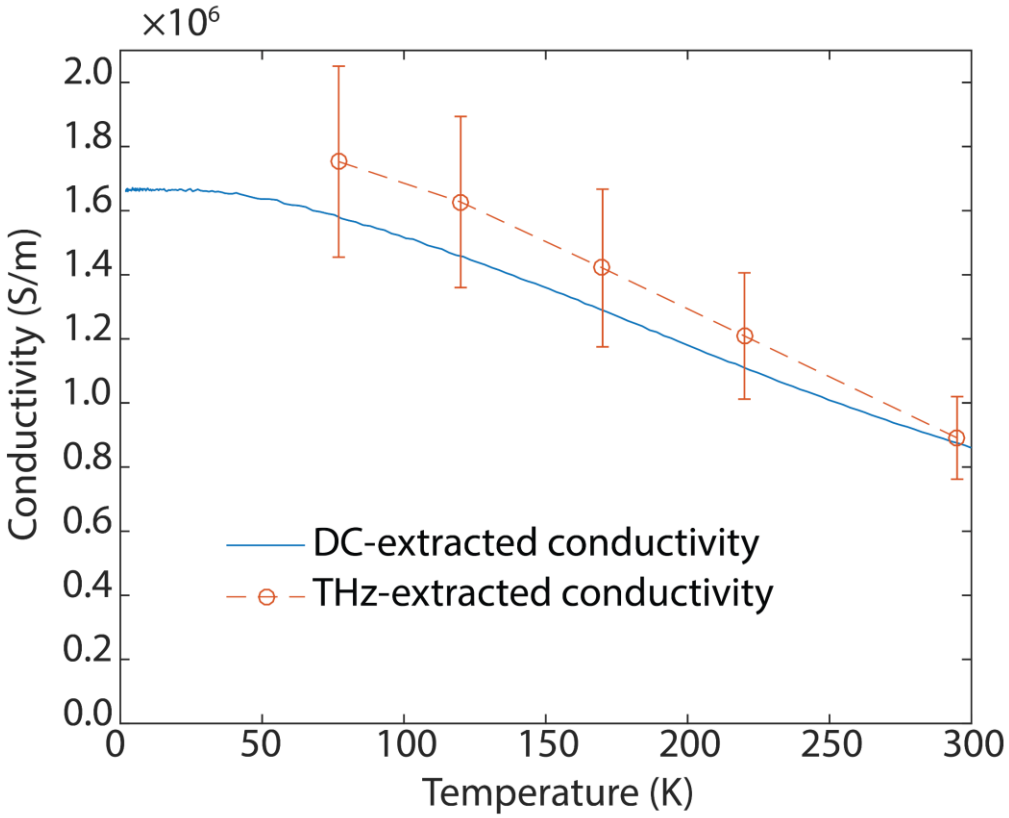

Figure 7.4. THz-extracted and DC-extracted conductivity vs. temperature for *Sample #1*. THz-extracted conductivity levels statistically agree with those observed in DC measurements; this observation is different from our previous observations in complex oxide 2DEGs, where a much larger THz-extracted conductivity was observed.

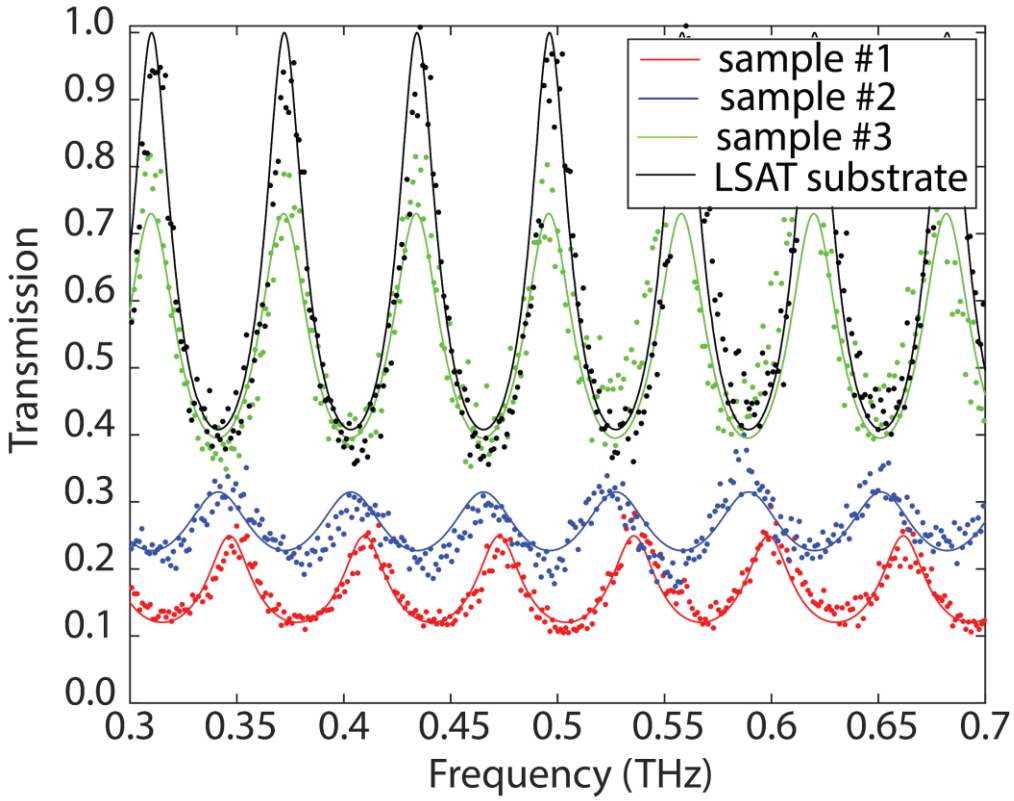

Figure 7.5. Measured CW terahertz transmission through Samples #1, #2, #3, and a bare LSAT substrate. The solid lines, represent the fitting of the measured data to the model described in *Methods* section.

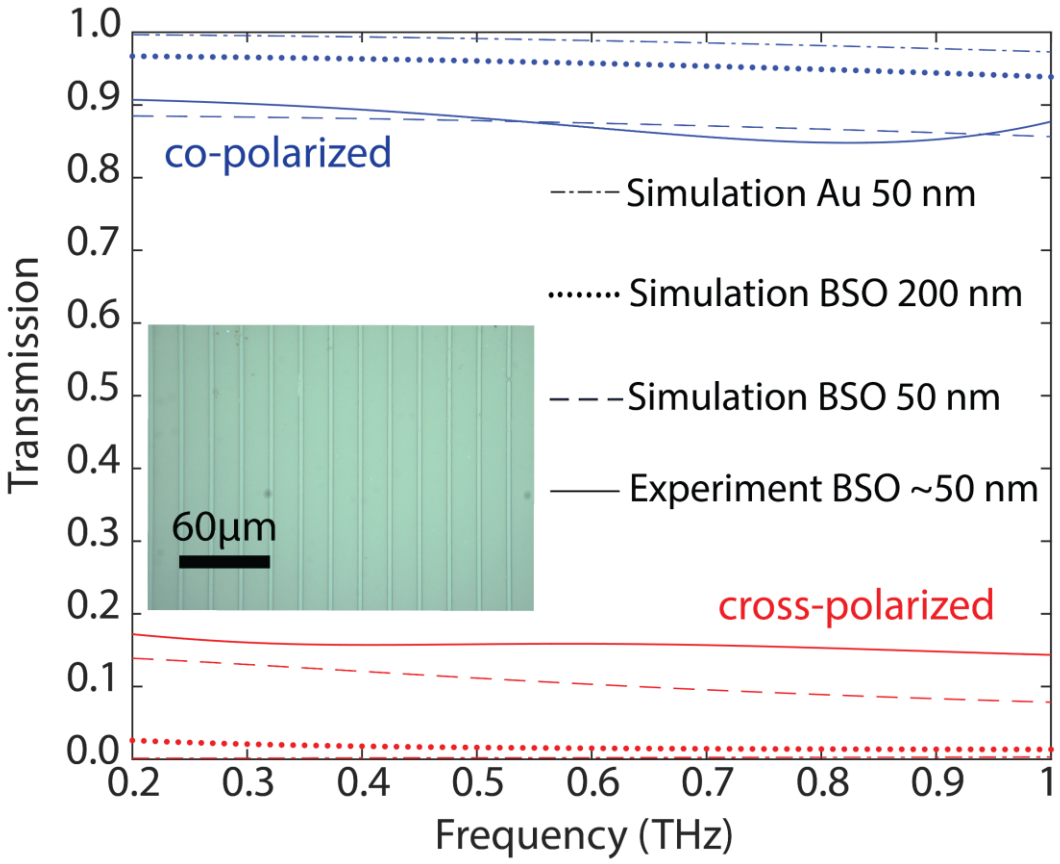

Figure 7.6. Co-polarized and cross-polarized transmission through polarizer structures. The continuous traces indicate our experimental results. Dotted and dashed curves represent modelled data. The inset shows an optical image of the fabricated sample, which is transparent to visible wavelengths.

7.9 References

[1] S. Masuda, K. Kitamura, Y. Okumura, S. Miyatake, H. Tabata, and T. Kawai, "Transparent thin film transistors using ZnO as an active channel layer and their electrical properties," *J. Appl. Phys.*, vol. 93, no. 3, pp. 1624–1630, Feb. 2003.

[2] P. F. Carcia, R. S. McLean, M. H. Reilly, and G. Nunes, "Transparent ZnO thin-film transistor fabricated by rf magnetron sputtering," *Appl. Phys. Lett.*, vol. 82, no. 7, pp. 1117–1119, Feb. 2003.

[3] R. L. Hoffman, B. J. Norris, and J. F. Wager, "ZnO-based transparent thin-film transistors," *Appl. Phys. Lett.*, vol. 82, no. 5, pp. 733–735, Feb. 2003.

[4] B. G. Lewis and D. C. Paine, "Applications and processing of transparent conducting oxides," *Mrs Bull.*, vol. 25, no. 8, pp. 22–27, 2000.

[5] C.-S. Yang *et al.*, "Non-Drude behavior in indium-tin-oxide nanowhiskers and thin films investigated by transmission and reflection THz time-domain spectroscopy," *IEEE J. Quantum Electron.*, vol. 49, no. 8, pp. 677–690, 2013.

[6] T. Bauer, J. S. Kolb, T. Löffler, E. Mohler, H. G. Roskos, and U. C. Pernisz, "Indium–tin–oxide-coated glass as dichroic mirror for far-infrared electromagnetic radiation," *J. Appl. Phys.*, vol. 92, no. 4, pp. 2210–2212, 2002.

[7] V. E. Babicheva, A. Boltasseva, and A. V. Lavrinenko, "Transparent conducting oxides for electro-optical plasmonic modulators," *Nanophotonics*, vol. 4, no. 1, pp. 165–185, 2015.

[8] T. Wang *et al.*, "Ultrabroadband terahertz conductivity of highly doped ZnO and ITO," *Opt. Mater. Express*, vol. 5, no. 3, pp. 566–575, Mar. 2015.

[9] C.-S. Yang, C.-M. Chang, P.-H. Chen, P. Yu, and C.-L. Pan, "Broadband terahertz conductivity and optical transmission of indium-tin-oxide (ITO) nanomaterials," *Opt. Express*, vol. 21, no. 14, pp. 16670–16682, Jul. 2013.

[10] E. R. Brown, W.-D. Zhang, H. Chen, and G. T. Mearini, "THz behavior of indium-tin-oxide films on p-Si substrates," *Appl. Phys. Lett.*, vol. 107, no. 9, p. 091102, Aug. 2015.

[11] R. Bel Hadj Tahar, T. Ban, Y. Ohya, and Y. Takahashi, "Tin doped indium oxide thin films: Electrical properties," *J. Appl. Phys.*, vol. 83, no. 5, pp. 2631–2645, 1998.

[12] H. Kim *et al.*, "Electrical, optical, and structural properties of indium–tin–oxide thin films for organic light-emitting devices," *J. Appl. Phys.*, vol. 86, no. 11, pp. 6451–6461, 1999.

[13] Y. Igasaki and H. Saito, “The effects of deposition rate on the structural and electrical properties of ZnO: Al films deposited on (1120) oriented sapphire substrates,” *J. Appl. Phys.*, vol. 70, no. 7, pp. 3613–3619, 1991.

[14] A. Prakash *et al.*, “Wide bandgap BaSnO3 films with room temperature conductivity exceeding 104 S cm- 1,” *Nat. Commun.*, vol. 8, 2017.

[15] A. Prakash, J. Dewey, H. Yun, J. S. Jeong, K. A. Mkhoyan, and B. Jalan, “Hybrid molecular beam epitaxy for the growth of stoichiometric BaSnO3,” *J. Vac. Sci. Technol. A*, vol. 33, no. 6, p. 060608, Nov. 2015.

[16] A. Prakash, P. Xu, X. Wu, G. Haugstad, X. Wang, and B. Jalan, “Adsorption-controlled growth and the influence of stoichiometry on electronic transport in hybrid molecular beam epitaxy-grown BaSnO 3 films,” *J. Mater. Chem. C*, 2017.

[17] B. Q. Hu, X. M. Wang, T. Zhou, Z. Y. Zhao, X. Wu, and X. L. Chen, “Transmittance and refractive index of the lanthanum strontium aluminium tantalum oxide crystal,” *Chin. Phys. Lett.*, vol. 18, no. 2, pp. 278–279, Feb. 2001.

[18] T. Kiwa and M. Tonouchi, “Time-domain terahertz spectroscopy of (100) (LaAlO3)(0.3)-(Sr2AlTaO6)(0.7) substrate,” *Jpn. J. Appl. Phys. Part 2-Lett.*, vol. 40, no. 1AB, pp. L38–L40, Jan. 2001.

[19] Y. Hishikawa, N. Nakamura, S. Tsuda, S. Nakano, Y. Kishi, and Y. Kuwano, “Interference-free determination of the optical absorption coefficient and the optical gap of amorphous silicon thin films,” *Jpn. J. Appl. Phys.*, vol. 30, no. 5R, p. 1008, 1991.

[20] D. J. Singh, Q. Xu, and K. P. Ong, “Strain effects on the band gap and optical properties of perovskite SrSnO3 and BaSnO3,” *Appl. Phys. Lett.*, vol. 104, no. 1, p. 011910, 2014.

[21] S. Soleimanpour and F. Kanjouri, “First principle study of electronic and optical properties of the cubic perovskite BaSnO 3,” *Phys. B Condens. Matter*, vol. 432, pp. 16–20, 2014.

[22] H. Yan *et al.*, “Tunable infrared plasmonic devices using graphene/insulator stacks,” *Nat. Nanotechnol.*, vol. 7, no. 5, pp. 330–334, May 2012.

[23] S. Arezoomandan *et al.*, “Large nanoscale electronic conductivity in complex oxide heterostructures with ultra high electron density,” *Apl Mater.*, vol. 4, no. 7, p. 076107, Jul. 2016.

[24] H. Ohta, M. Orita, M. Hirano, H. Tanji, H. Kawazoe, and H. Hosono, “Highly electrically conductive indium–tin–oxide thin films epitaxially grown on yttria-

stabilized zirconia (100) by pulsed-laser deposition," *Appl. Phys. Lett.*, vol. 76, no. 19, pp. 2740–2742, 2000.

[25] L. Duvillaret, F. Garet, and J.-L. Coutaz, "A reliable method for extraction of material parameters in terahertz time-domain spectroscopy," *IEEE J. Sel. Top. Quantum Electron.*, vol. 2, no. 3, pp. 739–746, 1996.

[26] D. M. Pozar, *Microwave Engineering*. Wiley, New York, NY, 2004.

[27] H. Ohta, M. Orita, M. Hirano, H. Tanji, H. Kawazoe, and H. Hosono, "Highly electrically conductive indium-tin-oxide thin films epitaxially grown on yttria-stabilized zirconia (100) by pulsed-laser deposition," *Appl. Phys. Lett.*, vol. 76, no. 19, pp. 2740–2742, May 2000.

CHAPTER 8

CONCLUSIONS AND FUTURE WORK

8.1 Graphene for THz applications

In the first three chapters of this dissertation, we discussed graphene as an active material to realize devices for THz applications. In this regard, we proposed a deep subwavelength metamaterial based on graphene for THz phase modulation. Our design can improve the efficiency of beam steerers based on phase modulators when compared to other metamaterial phase modulators proposed in the literature. Due to the small area covered by the active region of the device, the speed of these devices can also improve with respect to that in previously proposed metamaterials integrated with graphene. In order to provide further insight into the performance levels of such devices, we analyzed their geometrical tradeoffs. For this purpose, we performed a simulation study for two families of deep subwavelength metamaterial, namely multi spiral resonators and multi split ring resonators. As a result of this study we found that there is a specific metal coverage ratio in both families of devices that leads to the best performance. In these cases, the unit cell to wavelength ratio is around $\lambda/20$.

A long-standing question in the literature is: what should be the role of graphene when developing THz devices? Graphene-based devices for THz applications can be divided in two major groups: (i) graphene plasmonic devices, in which graphene is both

acting as the plasmonic medium as well as the reconfigurable medium, and (ii) graphene-metal hybrid devices, in which the electromagnetic properties of the device are mainly set by the metallic structure, whereas the reconfigurability is enabled by graphene, which is integrated within the metallic structure. By comparing these two families of devices we found out that due to the poor quality of current large area CVD graphene, which is essential for THz applications, graphene-metal hybrid approaches can achieve much better quality factors and stronger electromagnetic responses. The carrier momentum relaxation time in CVD grown samples is usually in the range of 100 fs and that leads to Q smaller than 1. However, since the electromagnetic properties of graphene-metal hybrid metamaterials are set by the metal pattern, by using this strategy and using graphene only as a reconfigure medium within the metamaterial, we can achieve much larger quality factors. However, by using this strategy the tunability range on the device is reduced. We demonstrated that there is a trade-off between response strength and tunability.

8.2 Other 2D materials beyond graphene

We analyzed 2D materials beyond graphene for THz metamaterial applications. In graphene, due to its Dirac band structure, there is a finite minimum conductivity. Therefore, there is always loss in these devices. By using other 2D materials, having a band gap, we can achieve zero conductivity in the off state. Thus, we can decrease the insertion loss by realizing devices with such a zero off state conductivity. Also, due to the minimum finite absorption in graphene, the active layer cannot be put in close proximity of the metallic pattern. From this perspective, we are losing the possibility of placing the active material on the regions of the device where maximum field enhancement takes place.

However, due to the smaller maximum conductivity achievable in MoS_2, with respect to that in graphene, the modulation depth observed in our metamaterial devices was smaller than that in graphene-based structures even by using multilayer MoS_2 and by putting the active layer right next to the metamaterial surface.

8.3 The power of THz spectroscopy as a technique for studying materials

We also discussed THz spectroscopy as a tool for characterizing 2D materials and TCOs. One of the structures that we studied is the heterostructure between NTO and STO, two complex oxide materials. In this heterostructure, a 2DEG is formed at the interface. We performed a systematic study across samples grown under different conditions, and compared the mobility extracted using DC electrical characterization tools with that extracted from THz measurements. We found that the transport properties of these 2DEGs, as extracted from electrical measurement, are affected by extended effects such as those arising from point defects and dislocations, which lead to a decrease in conductivity of the 2DEG with respect to what is extracted from THz measurements. Therefore, THz spectroscopy is a better estimate for the nanoscale transport properties of these materials. Furthermore, we employed THz spectroscopy to characterize a transparent oxide film (BSO) with record high conductivity (at room temperature and among this family of materials). We extracted the refractive indices, and from the extracted properties we designed and fabricated a THz polarizer that is transparent at visible wavelengths. Our results show that BSO is an attractive material for the design of THz devices that are transparent in the visible and near-IR range.

8.4 Future works

To follow up our theoretical studies on graphene-based modulators, we demonstrated an alternative geometry to the two discussed in this dissertation, which can also improve the phase modulation while keeping a small unit cell to wavelength ratio. Our simulations predict that the proposed device can achieve 2X larger phase modulation than other semiconductor-based THz phase modulators reported in the literature. Moreover, this device can achieve the same transmission amplitude thus the same loss level as our previous proposed MSRR and MSR structures. In Fig. 8.1.a, a detail of the unit cell is shown; graphene is placed in the center of the unit cell where the metal arms meet. Furthermore, an optical microscopy image of a fabricated sample is shown in Fig 8.1.b, although the device is not complete. Finally, in Fig. 8.1.c the simulated amplitude and phase of transmission for different graphene conductivity levels is shown, which indicates a resonance at 0.6THz and ~90° phase modulation [1].

Moreover, we also performed modeling of a beam steerer, by assuming an array of antennae creating a phase gradient in accordance with what is possible in these devices, and the same unit cell size. This enabled us to analyze the effect of the unit cell to wavelength ratio on beam steering performance, thus to demonstrate why it is good to utilize deeply-scaled metamaterials. Fig. 8.2 depicts the directivity for an infinite antenna array, for different unit cell to wavelength ratios, the phase gradient in each case is designed to achieve a 45° angle in transmission, and the incident wave is a normally incident plane wave. As demonstrated, with decrease in the unit cell to wavelength ratio, the array becomes more directive for the designed angle. To improve the model, we can consider the radiation pattern for each element, here the unit cell of the phase modulator. In this

preliminary study, we assumed an omnidirectional radiation pattern for each antenna.

The next step is to fabricate and test the devices. In addition, there is also room to come up with better metamaterial structure geometries that could achieve larger phase modulation as well as higher amplitude of transmission. Either geometric optimization or an exploration of the entire design space by means of random geometry simulations, as performed in Ref. [2] could be employed for this purpose.

In terms of transparent devices, the next step is to design and fabricate a metamaterial based on BSO and to integrate it with active 2D materials such as graphene or TMDCs so to achieve a reconfigurable THz device that is fully transparent to visible and near-IR wavelengths. These devices could find multiple applications in THz systems. For example, as indicated in Fig. 8.3, if we fabricate the same split ring resonator structure as discussed in Ref. [3] but substitute the gold (metallic part) with 200nm of BSO, then we will obtain a very similar electromagnetic response but in a device being fully transparent. By transferring directly growing MoS_2 or $MoTe_2$ (which was found by other of our group members, Prashanth Gopalan, to enable a THz conductivity swing similar to that in graphene by means of optically pumping), we can demonstrate a THz active filter that is fully transparent. This idea can be also used for amplitude modulation, phase modulation, active focusing, and beam steering. We can develop a complete set of devices, with a full array of functionalities by integrating highly-conductive TCOs (as transparent replacements of traditional metals) with 2D materials (as effectively transparent replacements of traditional semiconductors).

Furthermore, we are also interested in employing dielectric metamaterials and to combine these with active 2D materials. As first experimental demonstrations of all-

dielectric metamaterials at THz frequencies were reported, e.g., [4], the interest in developing these devices for different application has risen. By using dielectric metamaterials, we can overcome the losses arising from using metallic structures. Furthermore, these devices could be transparent to other target wavelengths. In this regard, our first goal is to integrate a dielectric metamaterial structure with a reconfigurable medium, e.g., graphene, to make a reconfigurable device. In order to show the feasibility of this approach, we performed a simulation study to find the best dimensions of the dielectric geometrical features to achieve maximum absorption modulation. We studied the same cylinder geometry as reported in [4], but employing undoped Si and just looked at the field distribution. In this study, we tried to maximize the electric field at resonance on the top facet of the cylinder. Figure 8.4 shows a simulation for these silicon cylinder metamaterials integrated with graphene, which is placed on top of the cylinder and whose conductivity is varied. Simulations were performed for two different conductivity levels in graphene. The values employed in this simulation are consistent with those we can typically achieve in CVD graphene. Our results show that by using this approach we can modulate the absorption in the device, from ~20 to ~90% by means of altering the conductivity of graphene. Whereas previous studies showed that dielectric metamaterials can be efficient wavelength selective absorbers, here we are showing that by integrating these with active semiconductors, we can also construct efficient reconfigurable absorbers. In the inset of Fig. 8.4 we depict an optical image of a fabricated device (without graphene); these devices are still under fabrication thus yet not complete. However, transmission measurements show resonance features in agreement with our simulations. The next steps in this projects are: (a) to transfer graphene on top of the Si cylinder array, (b) to construct

a series of samples of different graphene conductivity by means of chemical doping, (c) to measure these and find the THz transmission as a function of graphene conductivity, (d) to check whether the results agree with our simulations, (e) to explore other 2D materials beyond graphene and experimentally demonstrate active tuning of absorption. Finally, it is worth mentioning that many papers have reported on graphene-metal hybrid metamaterials and graphene-only plasmonic metamaterials at THz wavelengths. However, to the best of our knowledge, in the literature there is a complete lack of experimental studies on graphene with all-dielectric metamaterials. Our studies will constitute some of the first demonstrations of these devices and will show that this is also an efficient approach leading to enhancing light-matter interaction in graphene.

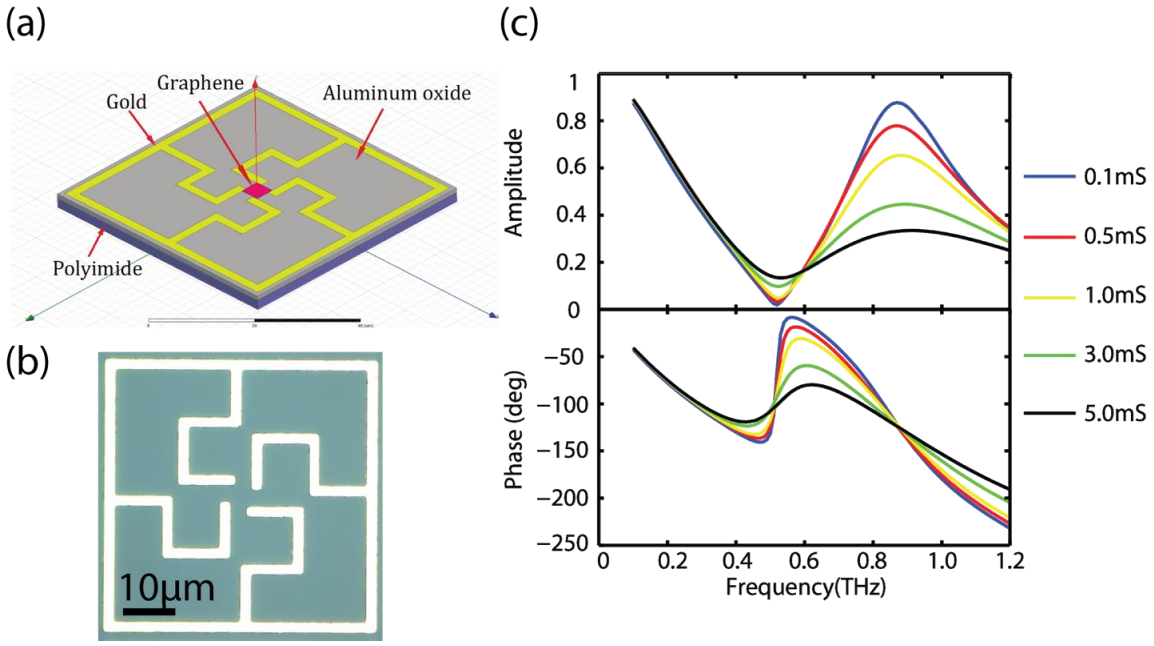

Fig 8.1. THz phase modulator (a) Unit cell structure of the proposed phase modulator, (b) Preliminary work, fabricated unit cell structure, (c) the amplitude and phase of transmission vs. frequency for different conductivity of the graphene sheet.

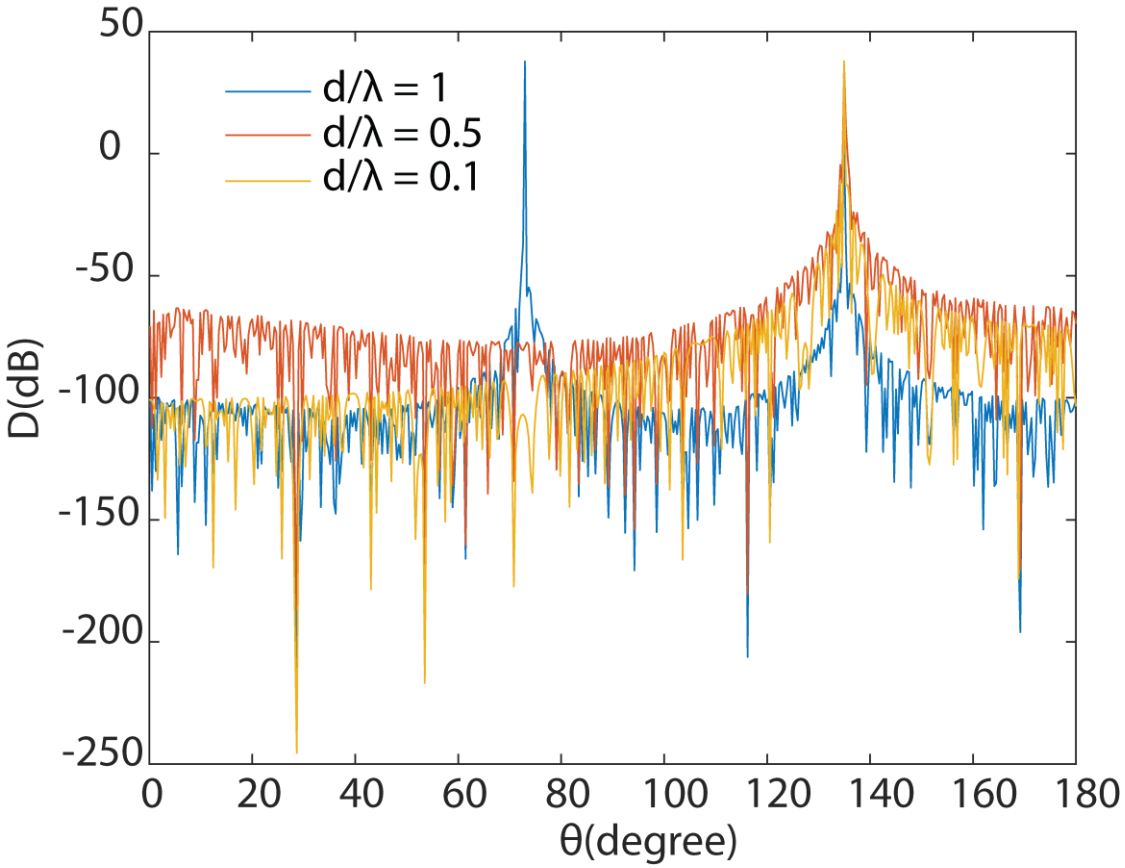

Fig 8.2. The directivity of an array of omnidirectional antenna with different unit cell to wavelength ratio. The array is designed so to have the transmission direction at 45°. As indicated, as the ratio becomes smaller the array become more directive.

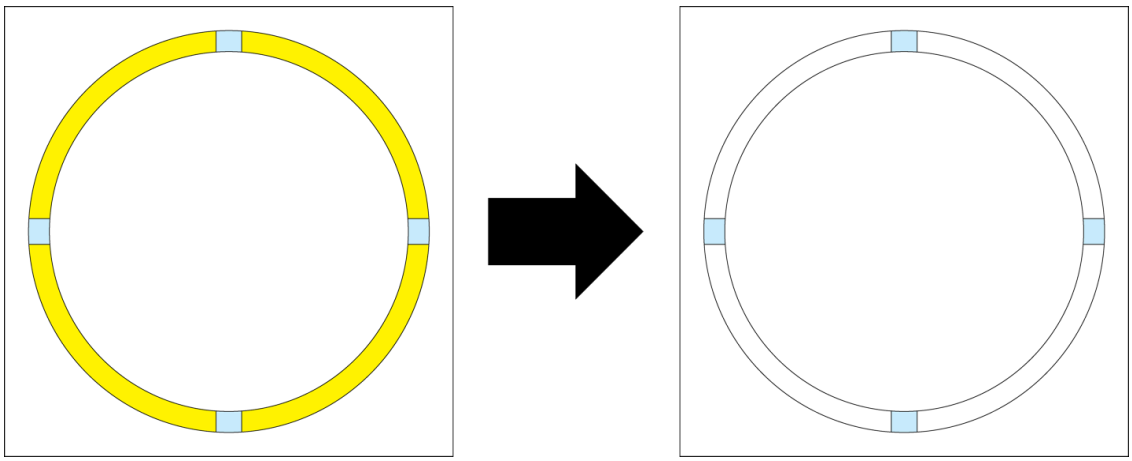

Fig 8.3. A metal-graphene hybrid metamaterial that operates as a THz filter, from Ref. [3], is shown on the left: gold is used as metal shown in yellow and graphene in the gaps is shown in light blue. Graphene due to its single layer nature is effectively transparent. In the left we show our proposed structure in which the gold is substituted with transparent BSO. Thus the final device will be transparent in the visible but operate as reconfigurable filter at THz wavelengths.

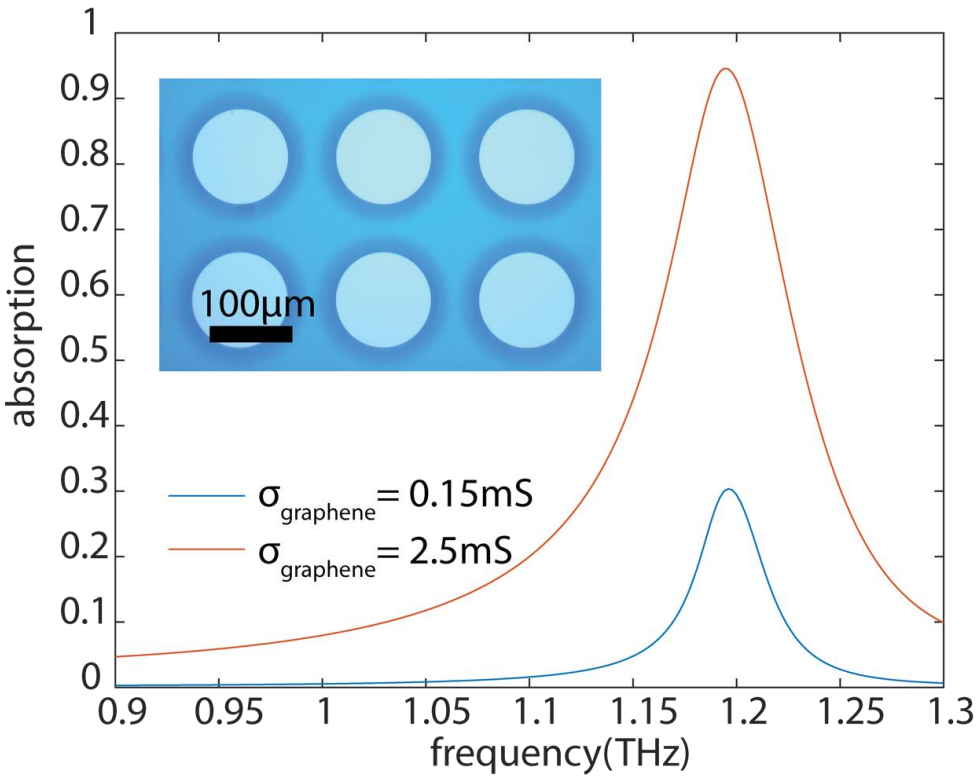

Fig. 8.4. The simulated absorption for a dielectric metamaterial structure which is integrated with a single layer of graphene placed on top of Si-cylinders. Simulations were carried out for two different graphene conductivities. The inset shows an optical image of the fabricated structure.

8.5 References

[1] S. Arezoomandan and B. Sensale-Rodriguez, "A deep-subwavelength metamaterial terahertz phase modulator," in *Infrared, Millimeter, and Terahertz Waves (IRMMW-THz), 2014 39th International Conference on*, 2014, pp. 1–1.

[2] M. Tamagnone, A. Fallahi, J. R. Mosig, and J. Perruisseau-Carrier, "Fundamental limits and near-optimal design of graphene modulators and non-reciprocal devices," *Nat. Photonics*, vol. 8, no. 7, pp. 556–563, 2014.

[3] K. Yang, S. Liu, S. Arezoomandan, A. Nahata, and B. Sensale-Rodriguez, "Graphene-based tunable metamaterial terahertz filters," *Appl. Phys. Lett.*, vol. 105, no. 9, p. 093105, 2014.

[4] X. Liu, K. Fan, I. V. Shadrivov, and W. J. Padilla, "Experimental realization of a terahertz all-dielectric metasurface absorber," *Opt. Express*, vol. 25, no. 1, pp. 191–201, 2017.

APPENDIX A

SUPPLEMENTARY INFORMATION: GRAPHENE-BASED RECONFIGURABLE TERAHERTZ PLASMONICS AND METAMATERIALS

Contents:

The material provided in this chapter is available at: Carbon 112, pp.177-184 (2017). Reprinted and adapted with permission from Elsevier.

A.1 Derivation of the analytical expressions for ω_p, E, and Q.

By substituting Eqn. (4.1) into Eqn. (4.3) —from the main manuscript— the following equation is obtained:

$$\frac{T}{T_0} = \frac{1}{\left|1+\frac{Z_0}{1+\sqrt{\varepsilon_S}}F\frac{\sigma_{graphene}(\omega)}{1+\frac{\pi}{2d\varepsilon_0(1+\varepsilon_S)i\omega}\sigma_{graphene}(\omega)}\right|^2}. \tag{R1}$$

Let us introduce the following two parameters (α and β) so to simplify the notation:

$$\alpha = \frac{Z_0 F}{1+\sqrt{\varepsilon_S}}, \tag{R2}$$

$$\beta = \frac{\pi}{2d\varepsilon_0(1+\varepsilon_S)}. \tag{R3}$$

Equation (R1) can thus be rewritten as:

$$\frac{T}{T_0} = \frac{1}{\left|1+\alpha\frac{\sigma_{graphene}(\omega)}{1+\frac{\beta}{i\omega}\sigma_{graphene}(\omega)}\right|^2}. \tag{R4}$$

Let us define: $f(\omega) = T/T_0(\omega)$, and $g(\omega) = 1/f(\omega)$.

At the plasmonic resonance frequency $f(\omega)$ exhibits a minimum, buy alternatively, when looking at $g(\omega)$, $g(\omega)$ should exhibit a maximum.

From Eqn. (R4), $g(\omega)$ can be expressed as:

$$g(\omega) = \left|1 + \alpha\frac{\sigma_{graphene}(\omega)}{1+\frac{\beta}{i\omega}\sigma_{graphene}(\omega)}\right|^2. \tag{R5}$$

At this stage let us employ Eqn. (2) from the main manuscript and substitute accordingly in Eqn. (R5). By doing this we obtain:

$$g(\omega) = \left|1 + \alpha\frac{\frac{\sigma_{DC}}{1+i\omega\tau}}{1+\beta\frac{\sigma_{DC}}{i\omega(1+i\omega\tau)}}\right|^2, \tag{R6}$$

which can be rewritten as:

$$g(\omega) = 1 + \alpha\sigma_{DC}(\alpha\sigma_{DC} + 2)\frac{\omega^2}{(\beta\sigma_{DC}-\omega^2\tau)^2+\omega^2}. \quad \text{(R7)}$$

Let us define $x = \omega^2$, and take the derivative of $g(x)$ with respect to *x*:

$$\frac{\partial g(x)}{\partial x} = \alpha\sigma_{DC}(\alpha\sigma_{DC} + 2)\left(\frac{1}{[(\beta\sigma_{DC}-x\tau)^2+x]} - \frac{x[1-2\tau(\beta\sigma_{DC}-x\tau)]}{[(\beta\sigma_{DC}-x\tau)^2+x]^2}\right). \quad \text{(R8)}$$

By looking at the zeros of Eqn. (R8), one can find the value of *x*, x_0, at which *g* (*x*) exhibits its minimum. It is observed that:

$$(\beta\sigma_{DC} - x_0\tau)^2 + x_0 - x_0(1 - 2\tau(\beta\sigma_{DC} - x_0\tau) = 0, \quad \text{(R9)}$$

so:

$$x_0 = \frac{\beta\sigma_{DC}}{\tau}. \quad \text{(R10)}$$

Since $x = \omega^2$, and because of the definition of β (Eqn. (R3)), the plasmonic resonance frequency is thus given by:

$$\omega_p = \sqrt{\frac{\pi\sigma_{DC}}{2d\varepsilon_0(1+\varepsilon_s)\tau}}. \quad \text{(4.4)}$$

This demonstrates Eqn. (4.4) from the manuscript main text.

At this point let us calculate for *E*:

$$E = 1 - \frac{T}{T_0}\Big|_{@\omega_p} = 1 - \frac{1}{g(\omega_p)} \quad \text{(R11)}$$

Because of Eqn. (R10), we know that at $\omega = \omega_p$: $\beta\sigma_{DC} - \omega_p^2\tau = 0$

Therefore, by inspecting Eqn. (R7):

$$g(\omega_p) = 1 + \alpha\sigma_{DC}(\alpha\sigma_{DC} + 2)\frac{\omega_p^2}{(\beta\sigma_{DC}-\omega_p^2\tau)^2+\omega_p^2} = 1 + \alpha\sigma_{DC}(\alpha\sigma_{DC} + 2) = (\alpha\sigma_{DC} + 1)^2 \quad \text{(R12)}$$

E can be now calculated as:

$$E = 1 - \frac{1}{g(\omega_p)} = 1 - \frac{1}{(\alpha\sigma_{DC}+1)^2}. \quad \text{(R13)}$$

By using the definition of α (Eqn. (R2)), it results:

$$E = 1 - \frac{1}{\left|1+\frac{Z_0 F \sigma_{DC}}{1+\sqrt{\varepsilon_S}}\right|^2}. \tag{4.5}$$

This demonstrates Eqn. (4.5) from the manuscript main text.

So to determine Q it is necessary to find the frequencies that satisfy the condition below:

$$1 - \frac{T}{T_0}\Big|_{@\omega_1,\omega_2} = \frac{E}{2}. \tag{R14}$$

Since:

$$1 - \frac{T}{T_0}\Big|_{@\omega_1,\omega_2} = 1 - \frac{1}{g(\omega)|_{@\omega_1,\omega_2}} = \frac{E}{2} \quad \Rightarrow \quad g(\omega)|_{@\omega_1,\omega_2} = \frac{2}{2-E}. \tag{R15}$$

Since $\beta\sigma_{DC} = \omega_p^2\tau$, we can rewrite $g(\omega)$ as:

$$g(\omega) = \frac{\left(\omega_p^2-\omega^2\right)^2\tau^2+(\alpha\sigma_{DC}+1)^2\omega^2}{\left(\omega_p^2-\omega^2\right)^2\tau^2+\omega^2}. \tag{R16}$$

Using Eqn. (4.5) from the manuscript main text, which we demonstrated a few steps back, we can write: $(\alpha\sigma_{DC}+1)^2 = 1/(1-E)$ and thus by substituting in Eqn. (R16) we obtain:

$$g(\omega) = \frac{\left(\omega_p^2-\omega^2\right)^2\tau^2+\frac{\omega^2}{1-E}}{\left(\omega_p^2-\omega^2\right)^2\tau^2+\omega^2}. \tag{R17}$$

Therefore when evaluating at ω_1 and ω_2, the following condition should hold (Eqns. (R15) and R(17)):

$$\frac{\left(\omega_p^2-\omega^2\right)^2\tau^2+\frac{\omega^2}{1-E}}{\left(\omega_p^2-\omega^2\right)^2\tau^2+\omega^2} = \frac{2}{2-E}. \tag{R18}$$

By rearranging terms, Eqn. (R18) can be rewritten as:

$$(\omega^2)^2 - \left(2\omega_p^2 + \frac{1}{\tau^2}\frac{1}{1-E}\right)\omega^2 + \omega_p^4 = 0. \tag{R19}$$

This equation is of the form: $Ax^2 + Bx + C = 0$, where: $x = \omega^2$.

The sum of the roots is given by:

$$x_1 + x_2 = \omega_1^2 + \omega_2^2 = -\frac{B}{A} = 2\omega p^2 + \frac{1}{\tau^2}\frac{1}{1-E}. \quad \text{(R20)}$$

And the product of roots is given by:

$$x_1 x_2 = \omega_1^2 \omega_2^2 = \frac{C}{A} = \omega_p^4. \quad \text{(R21)}$$

So from Eqns. (R20) and (R21), one can observe that:

$$(\omega_1 - \omega_2)^2 = \omega_1^2 + \omega_2^2 - 2\omega_1\omega_2 = \frac{1}{\tau^2}\frac{1}{1-E}. \quad \text{(R22)}$$

And, therefore:

$$\Delta\omega = |\omega_1 - \omega_2| = \frac{1}{\tau}\frac{1}{\sqrt{1-E}}. \quad \text{(R23)}$$

Hence, the quality factor (Q) is given by:

$$Q = \frac{\omega_p}{\Delta\omega} = \omega_p \tau \sqrt{1-E}. \quad \text{(4.6)}$$

This demonstrates Eqn. (4.6) from the manuscript main text.

It is worth mentioning that Eqns. (4.5) and (4.6) are general and hold for any graphene pattern of convex geometry, i.e., squares, rectangles, triangles, etc.

A.2 General contour plots for ω_p, E, and Q.

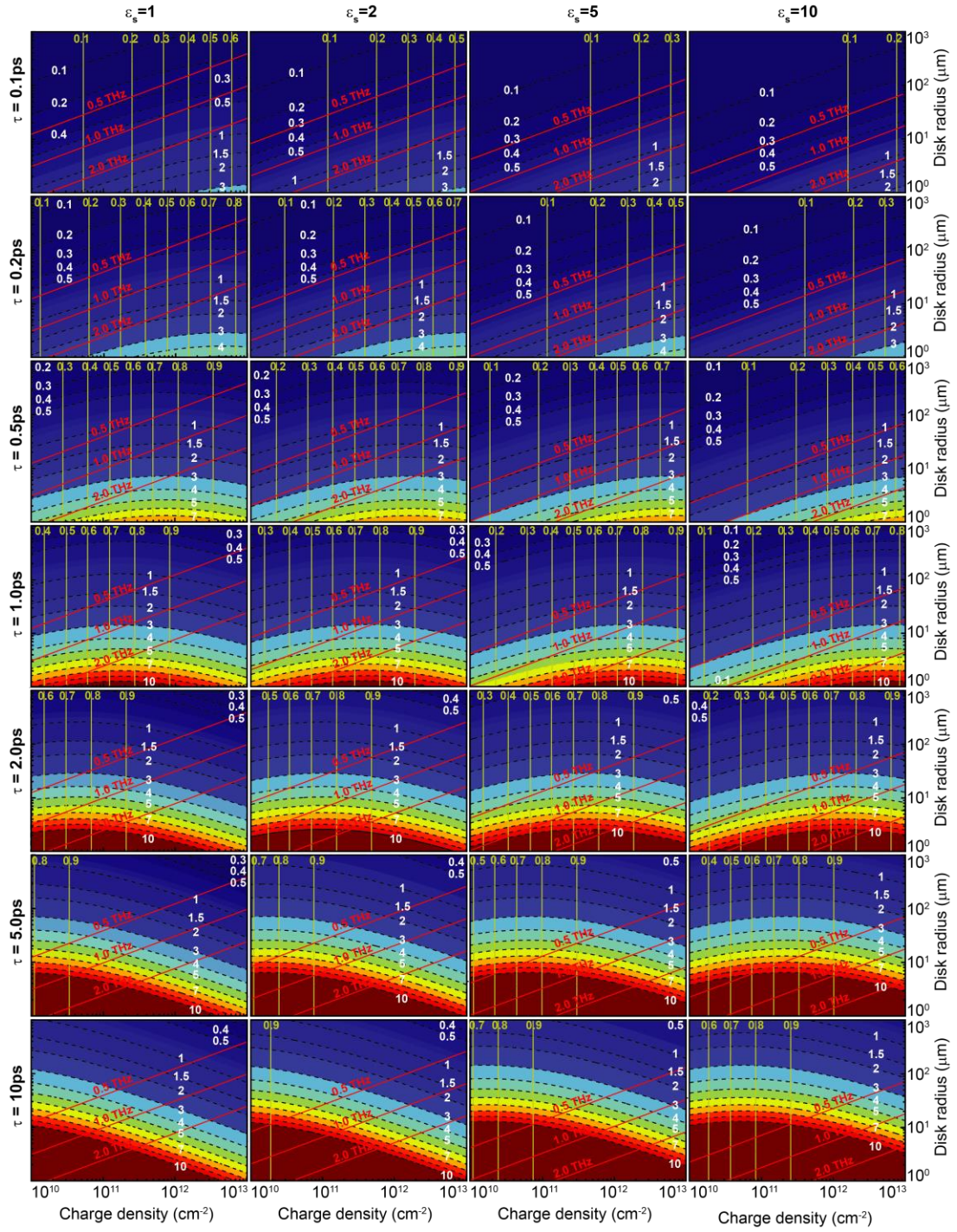

Figure A.1. Contour plots of Q (filled), E (yellow-traces), and ω_p (red-traces) as a function of charge density and disk radius for different values of τ and ε_s.

A.3 Equivalent Transmission Line Model for the SRR-based graphene/metal hybrid structure

The analyzed SRR-based geometry (*Sample Set #2*), can be modelled using the equivalent circuit model described by Fig. 4.2(b) in the main text. Following the discussion in Ref. [18], graphene is modeled as an impedance of value $Z_g = R_g + i\omega L_g$, where R_g and L_g represent its associated resistance and inductance, respectively, as shown in Fig. A.2. The transmission can be calculated using the following formula:

$$T = \left|\frac{2Z_{in}}{Z_{in}+Z_0}\right|^2. \quad \text{(R.24)}$$

where Z_{in} represents the input impedance, i.e., $Z_{in} = \{R+i\omega L+1/i\omega C\}//Z_0$. Moreover, as discussed in the main manuscript, L represents the self-inductance of the metal loop, R the metal losses, and the capacitor C results from the separation between adjacent unit cells. Therefore, for the equivalent circuit depicted in the middle panel of Fig. 4.2(b) of the main text, which consists of a closed metallic loop, the transmission is given by:

$$T = \left|\frac{2}{2+\frac{Z_0}{R+i\omega L+\frac{1}{i\omega C}}}\right|^2. \quad \text{(R.25)}$$

So by fitting the simulated data to this model we find $R = 0\ \Omega$, $C = 1.34$ fF, and $L = 122$ pH. Since this simulation was performed assuming lossless materials (PEC), we expect the resistance to be zero. Moreover, the capacitance and inductance set the resonance-frequency to be at $f = 1/2\pi\sqrt{LC} \sim 0.4$ THz.

When gaps are added, the capacitance of the structure is increased; the gaps insert a series capacitance C_{gap}. We can find the transmission using the following equation, which is based on the model depicted in the right panel of Fig. 4.2(b) on the main text:

$$T = \left| \frac{2}{2 + \frac{Z_0}{R + i\omega L + \frac{1}{i\omega C} + \frac{1}{i\omega C_{gap}}}} \right|^2 . \quad \text{(R.26)}$$

By fitting our simulation results to this model, and by using the R, L, C parameters previously found, we find that C_{gap} = 0.83 fF. In this case, the resonance corresponds to at $f = 1/2\pi\sqrt{L(C.C_{gap})/(C + C_{gap})}$ ~ 0.65 THz.

When we add graphene into the gaps, the structure can be modeled using the equivalent circuit depicted in the left panel of Fig. 4.2(b) on the main text. The transmittance through the structure is given by:

$$T = \left| \frac{2}{2 + \frac{Z_0}{R + i\omega L + \frac{1}{i\omega C} + \frac{R_g + i\omega L_g}{i\omega C_{gap}(R_g + i\omega L_g) + 1}}} \right|^2 , \quad \text{(R.27)}$$

thus:

$$T = \left| \frac{2}{2 + \frac{Z_0}{R + i\omega L + \frac{1}{i\omega C} + \frac{1/\alpha\sigma_{graphene}}{i\omega C_{gap}/\alpha\sigma_{graphene} + 1}}} \right|^2 . \quad \text{(R.28)}$$

In the latter formula, α is a parameter which is used to consider the field enhancement effect in graphene as discussed in Ref. [18]. We employ this model to fit the simulated data for different graphene conductivity values to the equivalent circuit model. To simplify the analysis, an electron momentum relation time (τ) equal to zero is assumed in our simulations as well as in the model. The results of the fitting are depicted in Fig. A.3(a). It is observed that the equivalent circuit model is capable of accurately representing the dynamic behavior observed in *Sample Set #2*. Moreover, depicted in Fig. A.3(b) is a plot of the extracted α versus graphene conductivity. As observed in previous studies, for

different metamaterial structures, e.g., Ref. [18], α is found to be independent on the graphene conductivity. In our case we found $\alpha \sim 3.4$.

In conclusion, the structure analyzed in Sample Set #2, can be well described by the equivalent circuit model depicted in Fig. A.2 by employing the following parameters: $R = 0\ \Omega$, $C = 1.34$ fF, $L = 122$ pH, $C_{gap} = 0.83$ fF, and $\alpha \sim 3.4$.

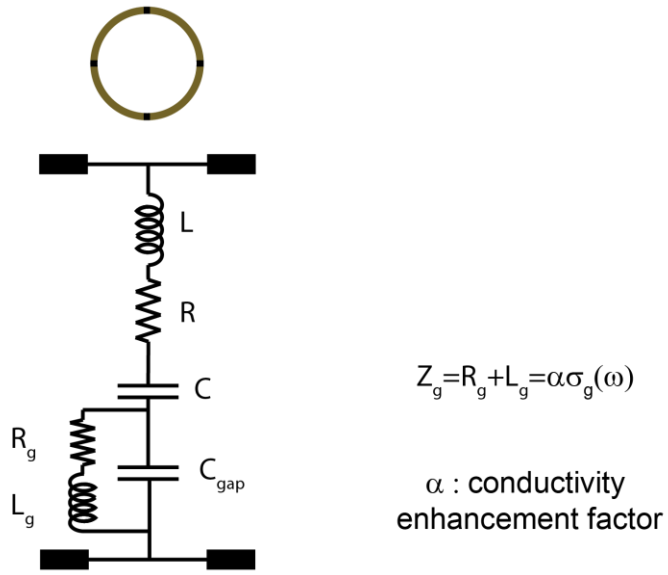

Figure A.2. Equivalent circuit model for the structure analyzed in *Sample Set #2*.

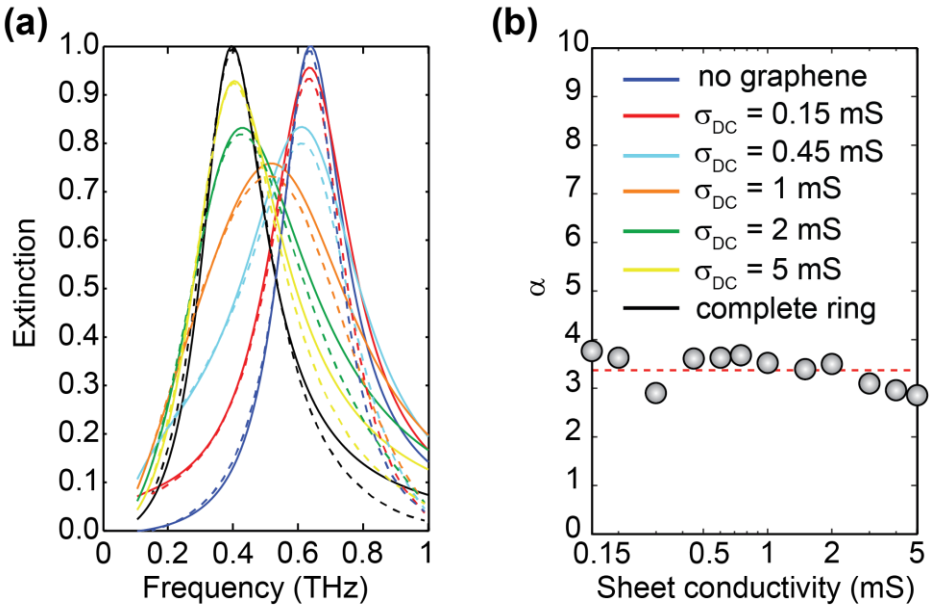

Figure A.3. (a) Simulated (dashed lines) extinction and calculated extinction from the fit to the equivalent circuit model (continuous lines). (b) Extracted α for different DC (sheet) conductivity levels in graphene; α ~ 3.4 is found to be independent on the graphene conductivity.

A.4 Effect of the electron momentum relaxation time on the response of the SRR-based graphene/metal hybrid structures

We performed simulations for the SRR-based graphene/metal hybrid structures (*Sample Set #2*) employing different values for the electron momentum relaxation time (τ). The results of those simulations are depicted in Fig. A.4. It is observed that for either low graphene conductivity, or high graphene conductivity, the response is (almost) independent of τ. However, at moderate conductivities, e.g., 1 mS, deviations start to take place when $\tau > 100$ fs.

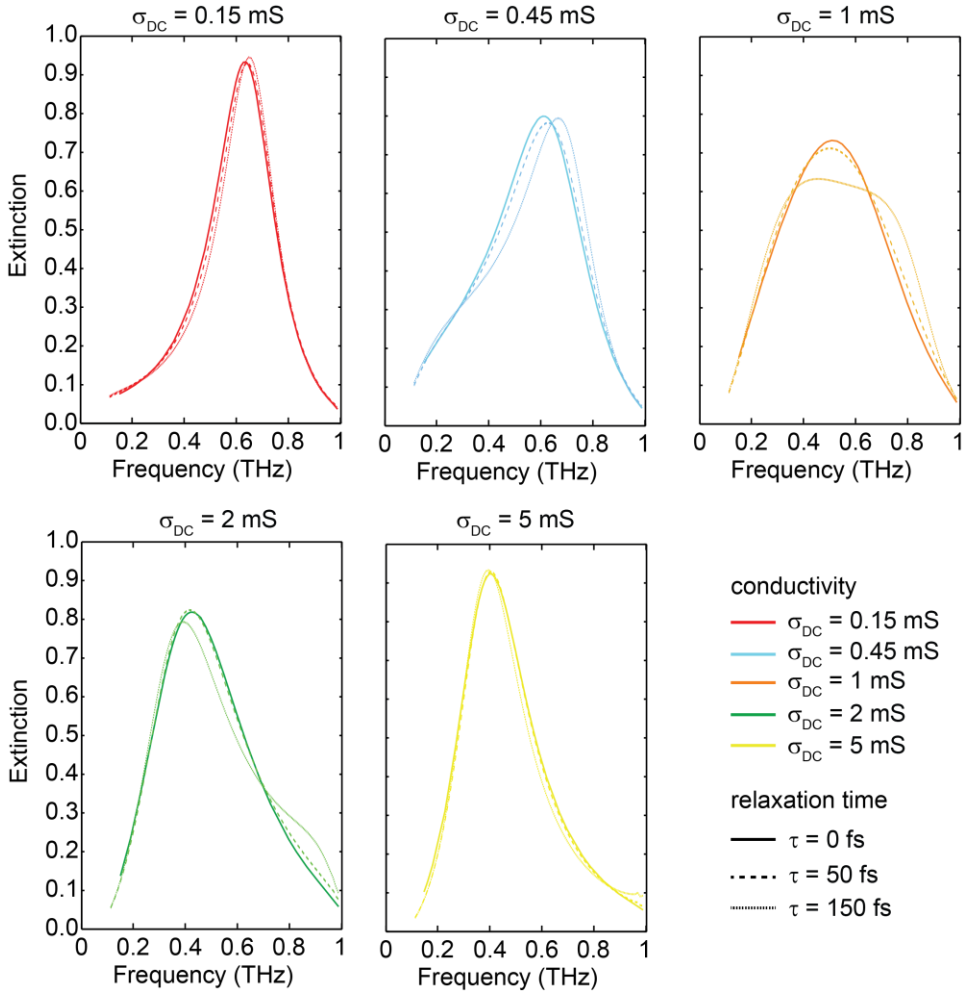

Figure A.4. Simulated extinction for different conductivity of graphene and different electron momentum relaxation times. The solid lines represent $\tau = 0$ fs, the dashed lines $\tau = 50$ fs, and the dotted lines $\tau = 150$ fs, respectively.

A.5 Raman spectroscopy of graphene

Raman measurements were conducted employing a WITec (Alpha300S) scanning near field optical microscope (SNOM). These measurements were carried out using a 488 nm linearly polarized excitation source operated in the back scattering configuration. A 20X objective was employed for this measurement, with 1sec integration time and 5mW power on the sample.

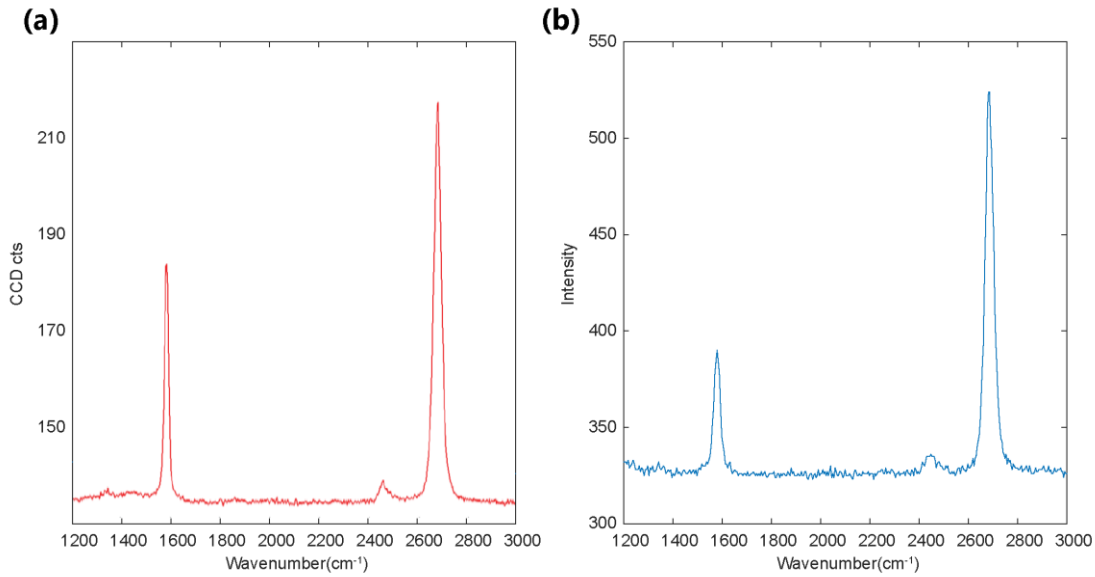

Figure A.5. Graphene Raman spectra before and after transfer a) Raman spectroscopy of the commercial graphene transferred on 285 nm SiO_2/Si substrate reported by the vendor (Bluestone). b) Raman spectroscopy of the one layer transferred film (on PI).

A.6 Graphene Drude model parameter extraction

As mentioned in the manuscript body, each sample consists of two adjacent (1cm × 1cm) square regions, containing the structure under test, and an unpatterned graphene control region, respectively. In order to characterize the graphene properties through the control region, two measurements are performed: (*i*) terahertz spectroscopy on the 0.1 to 2 THz spectral range; and (*ii*) FTIR on the 3 to 12 THz spectral range. By using Eqns. (4.2-4.3) from the manuscript main text, Eqn. (R24) is obtained. Therefore, the DC conductivity and momentum relaxation time can be extracted from the transmission measurements by fitting to:

$$\frac{T}{T_0} = \frac{1}{\left|1+\frac{Z_0 \sigma_{DC}}{1+\sqrt{\varepsilon_S}1+i\omega\tau}\right|^2}. \tag{R29}$$

In Eqn. (R24): $Z_0 = 377\ \Omega$ is the vacuum impedance, and $\varepsilon_s = 3.24$ is the relative permittivity of polyimide [39-40]. Depicted in Fig. A.6 is an example of the fitting, corresponding to *Sample Set #1*, case (*i*).

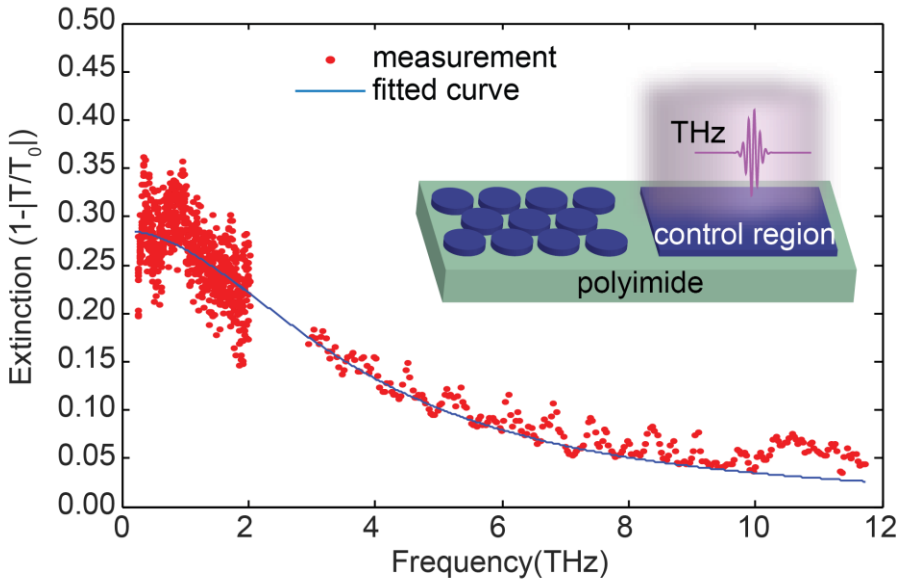

Figure A.6. Measured extinction for a graphene control region as obtained from THz and FTIR measurements, and fit to the analytical expression from where the Drude model parameters are extracted (Eqn. (R24)).

A.7 Details of the simulated geometries as set in HFSS

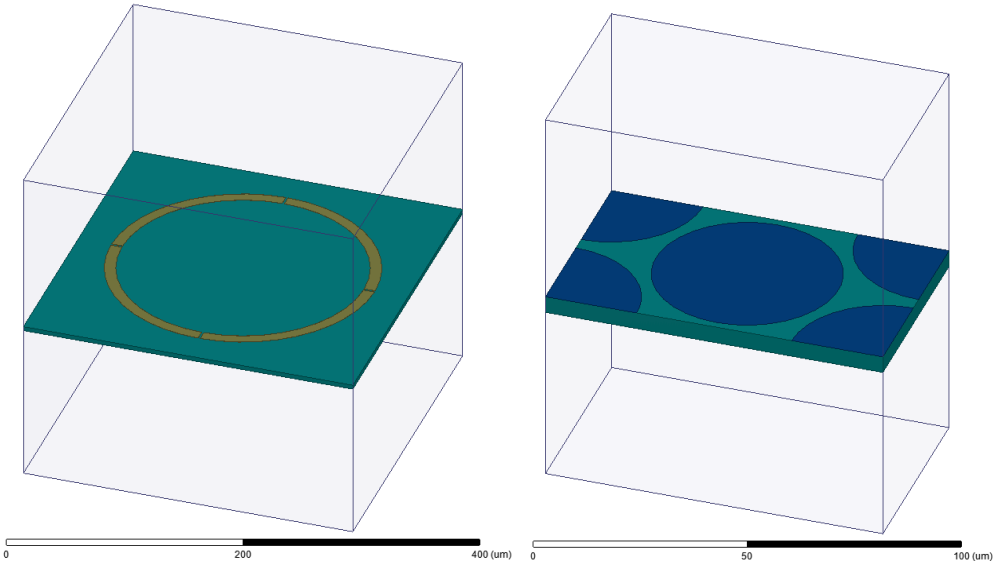

Figure A.7. Detail of the simulation geometries as set in HFSS for (left) the SRR graphene/metal hybrid structure and (right) the graphene-disk plasmonic structure. Periodic boundary conditions were set around the unit cells.

A.8 Continuous-Wave (CW) terahertz spectroscopy system

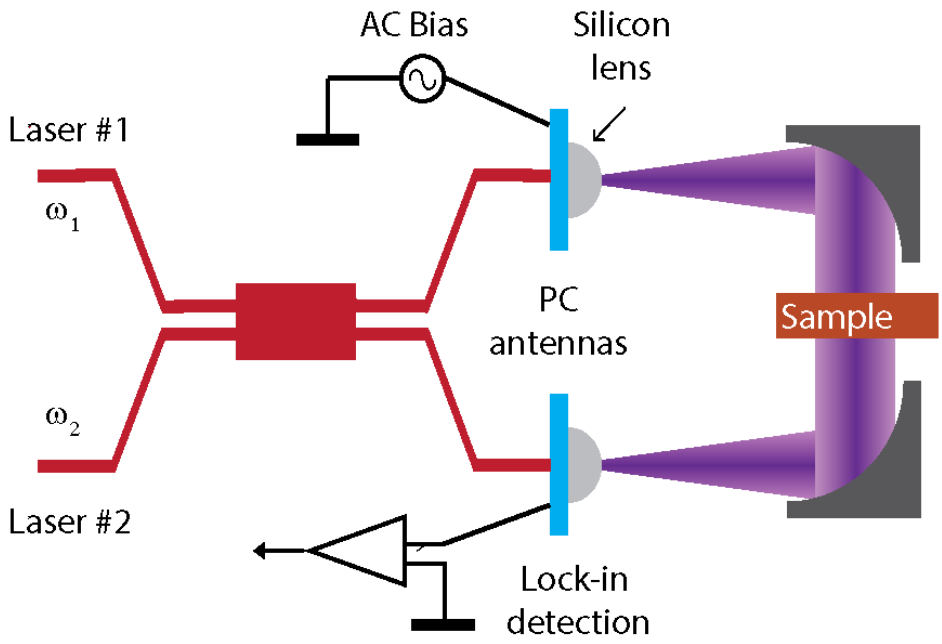

Figure A.8. Schematic diagram of the employed CW THz spectroscopy system.

APPENDIX B

FABRICATION TECHNIQUES

B.1 Wafer cleaning

For wafer cleaning two different processes were employed. For cleaning a sample that goes into the furnace for oxide or nitrite growth or deposition RCA cleaning procedure is performed. For lithography or polymer deposition nanostrip cleaning process is used.

B.1.1. RCA cleaning recipe. The RCA cleaning procedure started by RCA2 and then was followed by RCA1 cleaning procedure. For RCA 2 procedure the sample is placed in the RCA 2 solution, at 70±5˚C for 10 minutes. Then followed by 5 minutes DI water rinse. For preparing the RCA 2 solution, hydrogen chloride(HCl) is diluted with water, 6 part water, 1 part HCl and heated up on a chemical hot plate. As the temperature gets to 70˚C 1part hydrogen peroxide(H2O2) is added, and after 1 or 2 minutes the solution starts making bubbles and it is ready to use. At this temperature the solution is only good to use for half an hour. After the procedure is done, the solation should be diluted with water and cools down to near room temperature, then poured down into the drain and all lab wares should be rinsed three times with DI water.

For RCA 1 procedure, the sample should be placed in the solution for 10 minutes and rinsed with DI water for 5 minutes afterward and in the end blown dry. For preparing the RCA 1 solution, ammonium hydroxide (NH4OH) 1 part with 5 part water is diluted

and heated up to 70±5˚C. When the solution reaches the desired temperature, 1 part hydrogen peroxide (H2O2) is added and the RCA1 solution is ready to use. The similar procedure is done for cleaning RCA 1.

B.1.2 Nanostrip cleaning. There is a dedicated tank for nanotstrip cleaning. For cleaning, the sample is placed in the nanostrip solution at 80˚C for 10 minutes, and then rinsed with DI water for 5 minutes and blown dry with N2.

B.2 Polyimide substrate

The polyimide substrate was spin coated and cured, and before measurement is peeled off. Here we used PI2611 that is customized for polyimide layer with thickness of 2-11µm. The recipe below is used for usual polyimide layer

- After cleaning substrate (usually glass or silicon) dehydrate at 150˚C for 10 minutes
- Spin coat with PI 2611(note: it is very viscous)
    - Dispense at 500rpm with ramp 1000r/s for 5sec
    - Spin at 5000rpm with ramp 1000r/s for 35sec
- Soft bake first at 90˚C for 90sec the at 150˚C for 90sec
- Curing at 300˚C for 30minutes, the temperature is increased gradually from room temperature with ramp of 4˚C/min and cooled down to room temperature with 6˚C/min ramp

The film thickness will be between 3.5-4.5µm. The solution become more viscous and the thickness increases during the time, as the bottle opens. The film thickness is increases in the edges of the sample.

B.3 Photolithography

The lithography is done using two different types of photoresist, and for each type the recipes are mentioned. The positive photoresist was the most popular one since it needs less preparation steps, but for certain application negative photoresist was needed.

B.3.1 Positive photoresist. Two types of positive photoresist were used in the cleanroom, S1813 and 9260. S1813 is used for thinner resist application and 9260 for thick applications.

B.3.1.1. Shiply 1813. I used this resist with two different thickness goal, very thin films and thin films. Very thin photoresist film is needed when the rabbit ear problem is bold in the target application.

The recipe below was used for very thin photoresist film (less than 1.2µm)

- After clean up the wafer, dehydration at 150 ˚C for 10 minutes
- Spin coating with S1813
    - Dispense at 500rpm with ramp 250r/s for 2 sec
    - Spin at 6000rpm with ramp 1000r/s, for 60sec
- Soft-bake at 110˚C for 90sec
- Exposure at SUSS for 4.5sec (lamp intensity 6.2mW/cm^2)
- Develop in AZ 300MIF for 30sec

The recipe below was used for thin photoresist (around 2µm)

- After clean up the wafer, dehydration at 150 ˚C for 10 minutes
- Spin coating with S1813
    - Dispense at 500rpm with ramp 250r/s for 2 sec
    - Spin at 3000rpm with ramp 1000r/s, for 60sec

- Soft-bake at 110˚C for 90sec
- Exposure at SUSS for 7.5sec (lamp intensity 5.3mW/cm^2)
- Develop in AZ 300MIF for 30sec

B.3.1.2. AZ 9260. This photoresist is used for achieving thick photoresist film from 5-20µm. The recipe below is used for patterning.

- After clean up the wafer, dehydration at 150 ˚C for 10 minutes
- Spin HMDS
    - Dispense at 500rpm with ramp 250r/s for 2 sec
    - Spin at 2400rpm with ramp 1000r/s for 60 sec
- Spin coating with AZ 9260
    - Dispense at 500rpm with ramp 250r/s for 2 sec
    - Spin at 2400rpm with ramp 1000r/s for 60sec
- Soft-bake at 110˚C for 165sec
- Exposure at SUSS for 12sec, 6 times (6.2 mW/cm^2)
- Develop in AZ 400 MIF (dilute with DI water 1:4) for 120sec

B.3.2. Negative photoresist. The negative photoresist that is used in the clean room is AZ 5214 E. This product can be used both as positive and negative resist. By performing the post exposure bake and the flood exposure this photoresist become image reversal. The recipe below is used for patterning

- after clean up the wafer, dehydration at 150˚C for 10 minutes
- Spin coating with 5214E
    - Dispense at 500rpm with ramp 250r/s for 2 sec
    - Spin at 5000rpm with ramp 1000r/s for 35sec

- Softbake at 110˚C for 90sec
- Exposure at SUSS for 4.5sec (lamp intensity was 6.2 mW/cm^2)
- Postexposure bake 120˚C for 120sec
- Flood exposure 4.5sec (lamp intensity was 6.2 mW/cm^2)
- Develop in AZ 400 MIF (dilute with DI water 1:4) for 120sec

B.4 Lift-off

For lift-off after evaporation of 100nm gold, immerse the sample in vessel with acetone, leave for 1-2 minute, the 30sec of sonication is enough for the lift-off process. For Different types films and thickness maybe more sonication is needed. Also samples sputtered may need more sonication time for lift-off process.

B.5 Graphene transfer

For graphene transfer there is one-day preparation before the actual transfer process. For this purpose, first graphene sample grown on copper foil should be cut into the size that is needed for the transfer, with scissors (cleaned with wipe). Copper foils are very fragile so the whole process should be done with extreme caution. After cutting graphene pieces should be cleaned, with soaking the pieces in to the acetone for 15 minutes, and after that just dried by putting them in the ambient and let the acetone evaporate. The graphene sample should become as flat as possible, it can be achieved by putting the sample between two clean glass slides and push them together. Afterward sample is pasted to a clean glass slide using kapton tapes (Note: keep the side of the copper foil with the graphene that needs to be used on top). The area that is covered with kapton tape need to

be very small since the graphene on those area is wasted, also all the sides should be cover to prevent the spin coat material to reach the other side of the copper foil.

Then graphene sample is spin coated with PMMA (950 PMMA C2) with speed of 500rpm, ramp 500rpm for 60 sec. Next the sample is left under fume hood for one night at least to get dry, we do not want to solidify the PMMA with heating since the flexibility of the PMMA film is essential for the transfer process. Next step is to remove the kapton tape and flip over the sample on to another clean glass slide and use kapton tape again to paste it to the glass slide. In CVD graphene process on copper, graphene is formed on both side of the copper foil. So the graphene film on the unwanted side should be etched by using O2 plasma. The graphene etch recipe in the oxford 80(RIE) tool use the following steps:

- Pump down to 0.9×10^{-4}Torr
- Purge N2 with 80sccm for 5 minutes
- Purge O2 with 90sccm and pressure 25 mTorr and RF power 150W for 15sec
- Purge and vent

After the graphene etching, the sample is ready for transfer. First the copper film should be etched by removing the kapton tape and flip the sample and place the uncovered side of the copper in the copper etchant solution at 40˚C. After all the copper etched, it can be recognized when copper color cannot be seen with eye and the sample is fully transparent. The etching process can take from 15minutes to 1hour, depend on the thickness of the foil and the etchant etch rate. The etch rate of the solution decrease during the time after the bottle is opened. Then using the clean silicon wafer graphene sample is moved from the copper etchant vessel to another vessel filled with DI water, and after 5 minutes most of the copper etchant in the sample get dissolve in DI water. For removing the copper etchant

fully, the sample can be moved to another DI water vessel and, but usually the first vessel is enough. Then by merging the desired substrate and putting the graphene sample on the desired spot the transfer process is done. (Note: due to the hydrophobic nature of some sample this step can be tricky). After taking out the sample from DI water and it should be kept at room temperature for at least 1hour, so the water leaves the area between the graphene and sample (to avoid cracks in the graphene sample due to bubbles). Then the sample is heat up to 120˚C for 10 minutes. After that the PMMA layer can washed with merging the sample in the acetone or using a pipette and pouring acetone on the sample.

B.6 Mask fabrication

For mask fabrication the Heidelberg MicroPG 101, is used with 12mW power and 50% intensity. After the exposure, the mask is developed in developer 352, developer 351(diluted in water 1:5), or AZ 1:1 for 30sec. Then the chrome film is etched in the chrome etchant for 90sec to 2 minutes, the etching should be stopped when the mask become completely transparent. After that the photoresist is washed by merging the mask into the acetone and followed by an oxygen plasma for 5 minutes.